BIDIRECTIONAL REFLECTANCE CORRECTION MODEL FOR COASTAL WATERS AND ITS APPLICATION TO MINIMIZATION OF UNCERTAINTIES IN SATELLITE AND IN-SITU WATER LEAVING RADIANCES AT LONG ISLAND SOUND COASTAL OBSERVATORY SITE

by

SOE MIN HLAING

A dissertation submitted to the Graduate Faculty in Engineering in partial fulfillment of the requirements for the degree of Doctor of Philosophy, The City University of New York

2012

This manuscript has been read and accepted for the
Graduate Faculty in Engineering in satisfaction of the
dissertation requirement for the degree of Doctor of Philosophy.

Dr. Alexander Gilerson

Date | Chair of Examining Committee

Dr. Mumtaz K. Kassir

Date | Executive Officer

Dr. Samir Ahmed

Dr. Barry Gross

Dr. Fred Moshary

Dr. Menghua Wang

Supervisory Committee

THE CITY UNIVERSITY OF NEW YORK

Abstract

BIDIRECTIONAL REFLECTANCE CORRECTION MODEL FOR COASTAL WATERS AND ITS APPLICATION TO MINIMIZATION OF UNCERTAINTIES IN SATELLITE AND IN-SITU WATER LEAVING RADIANCES AT LONG ISLAND SOUND COASTAL OBSERVATORY SITE

by

Soe Min Hlaing

Adviser: Professor Alexander Gilerson

Co – adviser: Professor Samir Ahmed

Ocean Color data validation is the absolute requirement to provide the steady and reliable Ocean Color data stream. In the validation of Ocean Color data, water-leaving radiances, retrieved from in situ or satellite measurements, need to be compared in very accurate manner. Both in-situ and satellite data to be used in the comparisons are required to be the representative of the typical water and environmental condition at the site without being affected by the unexpected natural and environmental perturbation. As the result, assessments of the uncertainties in the water leaving radiance data must be carried out in the measurement and the every step of data processing procedure. With the hyper- and multi-spectral water leaving radiance data retrieved for the different viewing geometries of the instruments at the Long Island Sound Coastal Observatory (LISCO), uncertainties in the water leaving radiance data and processing procedures have been assessed and quantified. Recommendations and algorithm improvements have been also made to reduce the uncertainties in the processing and validation of Ocean Color data. Particularly, remote sensing reflectance model to correct the bidirectional angular dependencies

in both in-situ and satellite data have been proposed. The proposed model is first validated with a one year time series of in situ above-water measurements acquired by collocated multi- and hyper-spectral radiometers which have different viewing geometries installed at LISCO. Match-ups and inter-comparisons performed on these concurrent measurements show that the proposed algorithm outperforms the algorithm currently in use at all wavelengths, with spectral average improvement of 2.4%. LISCO's time series data has also been used to evaluate improvements in the match-up comparisons of MODIS satellite data when the proposed Bidirectional Reflectance Distribution Function (BRDF) correction is used in lieu of the current algorithm. It has been shown that the discrepancies between coincident in-situ sea-based and satellite data were decreased by 3.15% with the use of the proposed algorithm. Possibility of the application of the developed BRDF algorithm for the open ocean conditions is also considered.

Acknowledgements

In the summer of 2006, right after receiving my Bachelor degree in Electrical Engineering at the City College of New York, I was given a remarkable opportunity of being on a research field trip to Sapelo Island, Georgia. As our team led by Dr. Alex Gilerson was an integral part of the multi organizational research effort, I met and worked alongside with several research scientists who inspired me with their convictions in their field of studies. That seven days long trip strengthened my desire to become a scientist and, looking back, it was one of the most important factor in achieving this far. For letting me being a part of the team and accepting me as the PhD student in the Ocean Color remote sensing group of Optical Remote Sensing Lab, I am grateful to Prof. Samir Ahmed.

It has been a great opportunity for me to have worked under supervision of Prof. Alex Gilerson who has a very broad experience in this field. My academic achievement as a first author of a scientific journal article would not have been realized without his support and guidance. Therefore, I would like to thank him for his support, guidance and, more importantly, patience at the times when I was not in right direction. I also would like to thank Prof. Samir Ahmed who gave me the opportunity to fulfill my dream of becoming a scholar for his support and guidance throughout my PhD study. Also working as part of a team, this thesis has contributions from many of colleagues including students, research associates and professors in the Optical Remote Sensing Lab at City College. From my interaction with them, during the past 6 years, I attained knowledge, beyond science that will very much benefit me in the years to come. Last but not least I would also like to thank Prof. Fred Moshary and Prof. Barry Gross for letting me teach at the City College as it will definitely benefit my career in the future.

This manuscript is dedicated to my parents who gave me the opportunity they never had in their life and their consistent and unconditional love and support. I also would like to devote this thesis to my fiancée who stood by me past nine years for better or worse. Her ultimate desire to see me succeed gave me the strength to continue on even when obstacles seem impassable. I share this accomplishment with everyone mentioned in this acknowledgement as I achieved because of their love, trust, guidance and support.

Table of Contents

List of Figures

List of Tables

1 Introduction

In the industrialized world, more than 50% of the population lives within 100 km of the coast. As this population expands, continued anthropogenic pressures are placed on coastal regions [1]. Consequently, coastal resource management is becoming increasingly important and the ability to provide large-scale synoptic monitoring of the coastal water quality is vital for the assessments of the anthropogenic impacts on the natural environments of coastal areas. As the result, Ocean Color (OC) satellite sensors such as the Sea-viewing Wide Field-of-view (SeaWiFS) [2] (operational till December 2010), Medium-spectral Resolution Imaging Spectrometer (MERIS) [3] and the Moderate-resolution Imaging Spectrometer (MODIS) [4] (both are currently operational) as well as Visible and Infra-red Imaging Radiometer Suites (VIIRS)[5, 6] (on orbit since October 2011), are becoming the crucial assets for the OC research community in its ability to provide large-scale, synoptic observations of phytoplankton biomass, marine productivity, suspended sediment load, and other valuable parameters of the open and coastal areas of the ocean.

Because of the opportunities afforded by the data obtained through these OC satellite sensors, a wide variety of ocean color models which relate the optical signature of the ocean to in-water constituents have been developed during the past decades[7-10]. As these models continue to evolve, their success in retrieving the in-water constituents from the OC satellite data entirely depends on the accurate determinations of the optical signatures (i.e. water leaving radiance and remote sensing reflectance) which carry the information regarding the optical properties of that water. However, determination of the water leaving radiance (consequently remote sensing reflectance) from the measurements made from OC satellite sensors is not straight forward

requiring the multiple rigorous processing steps such as the procedures to remove the contribution of atmospheric and ocean surface radiances to the total radiance measured by the satellite sensor and the bidirectional correction of the water leaving radiances to eliminate their dependency on angular variations.

It is well recognized that more than 90% of the signal measured by an ocean color satellite sensor is due to the confounding influence of the atmosphere [11]. The atmospheric and ocean surface effects must be removed before ocean radiance signals can be analyzed for the purposes of understanding the ocean biosphere. These so called atmospheric correction procedures for satellite OC data of the ocean waters have been developed [12, 13] and proved to be providing the corrections with the reasonable accuracies for the open ocean areas and moderate coastal waters with low turbidity index [14].

Similarly, resulting water-leaving radiances after the atmospheric correction procedures must be further processed to remove the bidirectional angular variations in them in order to standardize the data and make them comparable with each other [15]. This bidirectional correction step is the most important step in the processing of satellite retrieved water-leaving radiance after the atmospheric correction step because the water-leaving radiance can typically vary 10 - 20% depending on the solar and viewing (observation) angles [16]. The angular variability in the emerging water leaving radiance field is mainly resulted from the non-isotropic character of the volume scattering function (VSF) of the water body, and thus it is also the function of the in-water constituents [17-19]. Therefore, removing the bidirectional effect from the retrieved water-leaving radiance requires the extensive knowledge of the optical properties of the water body itself beforehand. Due to the importance of the subject, variations in the bidirectional properties

of the upward radiance field have already been extensively studied. Notably, Morel and Gentili [15] reported the variations in the bidirectional properties of the upward radiative field for case 1 (open ocean) waters, and their studies related the bidirectional variations of water leaving radiance field to phytoplankton particulate (i.e. chlorophyll) concentration. Their finding were tentatively extended to typical case 2 (coastal) waters, and are currently being used in the NASA ocean color data processing procedures as the operational correction algorithm for the retrieval of water leaving radiance from both case 1 and case 2 water types [15]. The efficacy of the current operational bidirectional correctional algorithm has already been confirmed [19, 20] and considered to be reasonably effective for the case 1 water conditions. However, unlike open ocean waters in which variability in the optical properties are mainly driven by the phytoplankton particulate, in-water constituents of the coastal areas are usually dominated by sediment or by colored dissolved organic matter (CDOM)[9, 21]. Therefore, the validity of using this correction algorithm, which was developed based on single particulate type (phytoplankton) assumption, in case 2 water conditions is questionable [16, 22-24]. Accordingly, the need for an improved version of a bidirectional reflectance correction algorithm particularly tuned for typical case 2 water conditions is the general consensus among the ocean color radiometry community [16, 22-24].

In the coastal waters, variability of optical properties and biogeochemical constituents tends to be particularly high [25, 26]. Moreover, optically complex aerosols are blown away from the mainland and might lie up to a couple of days over the coastal area. This overall optical complexity of the atmospheric-water system makes observation from space highly challenging because geophysical processing of the satellite data is highly sensitive to the atmospheric and water composition. Consequently, the retrieved water-leaving signal, which carries information

on water optical properties and water composition, is not error free and its reliability needs to be assessed and validated against actual high quality in-situ field measurements. The assessments and validations are usually done by performing the matchup and comparisons between the field measurements usually carried out from the boats or offshore platforms and coincident satellite data of the location [27-30]. These matchup comparisons between the satellite and in-situ data can provide the valuable information regarding the effectiveness and validity of the overall satellite OC data processing and correction procedures [27, 31]. However, these comparisons themselves require the bidirectional correction because the observation and illumination angles of the in-situ instrument and those of satellite sensor are usually different from one another. Unless correction algorithm appropriate for the water types being investigated is used, validity of the OC sensor data may not be properly assessed and even lead to erroneous interpretation of the validation results.

Aiming at supporting the requirement of satellite data validation, network of observational platforms equipped with spectral radiometers that measure the radiance emerging from the sea (i.e., water-leaving radiance) as well as sky and solar irradiance were established throughout the coastal areas around the world to provide the satellite ocean color validation activities through standardized measurements performed at different sites [29, 32-34]. The Aerosol Robotic Network (AERONET) [35], developed primarily to sustain atmospheric studies at various scales with measurements from worldwide distributed autonomous sun-photometers has been extended with the additional capability of measuring the radiance emerging from the sea to support ocean color remote sensing applications [30, 36]. This new network component with additional capability of measuring water-leaving radiance are called AERONET – Ocean Color (AERONET-OC). As part of the AERONET-OC, City College of New York (CCNY) has

established a new scientifically comprehensive off-shore platform, the Long Island Sound Coastal Observatory (LISCO) to support present and future multi- and hyper-spectral calibration/validation activities, as well as the development of new measurement and retrieval techniques and algorithms for coastal waters [33, 37, 38]. LISCO's instrument suite includes the two independent above water radiometers which have different viewing geometries from one another. As the result, match-ups and inter-comparisons performed on the concurrent measurements of these co-located instruments permit us to carry out the detailed analysis on the angular variations of the water-leaving radiance field of the LISCO site [23]. In addition, these coincident measurements also allow us to perform the assessments of the intrinsic uncertainties in the in-situ data associated with the in-situ above water measurements and data processing procedures. These concurrent measurements also permit the self-quality checking of data and thus, consistent and reliable time series in-situ data record to be used for the validation of the OC satellite data can be created.

Background analysis of LISCO area water characteristics based on the time-series OC satellite data has been carried out and it was found that water parameters are typical for coastal waters with the moderate variability [34]. The combination of LISCO's typical coastal water characteristics and ability of its instruments to make concurrent water-leaving radiance measurements from the different viewing geometries enable us to (i) quantify the uncertainties in the in-situ above water measurements and create self - quality checked and reliable time series in-situ OC data records; (ii) analyze the bidirectional properties of the water-leaving radiance field typical to coastal water conditions; (iii) develop the bidirectional correction algorithm optimized for the coastal water conditions and test the validity of the algorithm by using it in data processing in lieu of the current operational one (iv) facilitate the validation of the OC

satellite data and processing procedures with the use of quality assured LISCO data processed with the appropriate bidirectional correction algorithm for the coastal water conditions.

In the second chapter, background of the satellite OC sensors and fundamental processing and correction procedures for the OC radiometry data currently in use will be discussed. Next, in chapter 3, fundamental inherent optical properties will be explained. In chapter 4, we will present the characteristics of the LISCO and its measurement systems along with the above water data processing procedure being used in the OC data validation. Assessments of the uncertainties in the above water measurements and data processing procedures will be carried out in chapter 5. In chapter 6, representativeness of LISCO as the validation site will be verified and uncertainties in the satellite OC data will be assessed with the use of quality assured above water data of LISCO. Chapter 7 details the radiative transfer simulations performed for the development of bidirectional correction algorithm. Moreover, analysis on the angular dependencies of the water leaving radiance field will be also carried out based on the water characteristics. In chapter 8, assessments of the proposed algorithm are made based on the simulated dataset, in-situ and satellite data. Summary and conclusions are presented in chapter 9.

2 Background of the Ocean Color Remote Sensing

2.1 Ocean color satellite sensors

The use of satellite remote sensing data to investigate oceanic processes has become essential for oceanographic research and monitoring [39]. Remote sensing of ocean color from space began in 1978 with the successful launch of NASA's Coastal Zone Color Scanner (CZCS) [40, 41]. CZCS mission demonstrated the possibility of mapping the phytoplankton pigment concentration in the upper ocean layers with an optical remote sensor and provided a worldwide picture of oceanic biomass[40-42]. Despite the fact that CZCS was an experimental mission intended to last only one year, the sensor continued to generate a valuable time-series of data over selected test sites until early 1986[30]. This achievement led to the development of numbers of increasingly advanced ocean color sensors capable of producing global images for worldwide oceanographic studies. Among these are the Moderate Optoelectrical Scanner (MOS)[43], Ocean Color Temperature Scanner (OCTS)[44] and POLarization and Directionality of the Earth's Reflectances (POLDER)[45], and Sea-viewing Wide Field-of-view Sensor (SeaWiFS)[2]. Ocean color remote sensing was brought to next level with the launch of Moderate-resolution Imaging Spectroradiometer (MODIS) instrument launched into Earth orbit by NASA in 1999 on board the Terra Satellite, and in 2002 on board the Aqua satellite [46, 47]. The instruments capture data in 36 spectral bands ranging in wavelength from 0.4 µm to 14.4 µm and at varying spatial resolutions (2 bands at 250 m, 5 bands at 500 m and 29 bands at 1 km). Together the MODIS instruments image the entire Earth every 1 to 2 days. Also in 2002, Medium Resolution Imaging Spectrometer (MERIS) was launched on board the European Space Agency (ESA)'s Envisat satellite[48]. The MERIS instrument provides 15 spectral bands ranging from 412 to 1050nm,

which are programmable in position, width and gain. The highest spatial resolution provided by the detector is 300 m near nadir at the Earth's surface and it is known as the 'Full Resolution (FR)' product. The more common 'Reduced Resolution (RR)' products are generated by aggregating the FR data to a nominal resolution of 1200 m. The total field of view of MERIS is 68.5 degrees around nadir (yielding a swath width of 1150 km), which is sufficient to collect data for the entire planet every 3 days (in equatorial regions).

Several new ocean-color sensors have recently been launched and still more are planned for the near future by various space agencies. Recent success in the launching of the Visible and Infra-Red Imaging Radiometer Suite (VIIRS)[5] [49, 50](which has the similar spectral bands in visible region as MODIS but with the higher resolution) makes possible the continuity of the reliable OC data stream as the new sensor can be validated against the currently operational sensors which are already in space[6]. Therefore, OC research community has been recently paying much attention to the validation activities of the both new and current operational OC sensors and, as the result, reliable data processing and correction algorithms are urgently needed.

2.2 Ocean color data

Microscopic plant lives called phytoplankton are at the base of the marine food chain and are the primary food and energy source for the ocean ecosystem. Phytoplankton convert nutrients into plant material through the process called photosynthesis by using sunlight with the help of the optically active green pigment called chlorophyll. In the process, they convert carbon dioxide from sea water into organic carbon and oxygen as a by-product and thus form an important part of the global carbon cycle [26]. Therefore, the global assessment of phytoplankton biomass and

its variations in time and space is essential for the long-term evaluation of ocean ecosystem health and for understanding changes in the ocean carbon cycle [26, 51, 52].

In the case 1 water phytoplankton is the main water constituent [8]. The color of ocean shifts from blue to green with the increasing presence of phytoplankton as they absorb light strongly in the blue regions of the spectrum and scatter light in the green regions. These spectrally dependent absorption and scattering properties of phytoplankton are resulted from the optically active pigment called chlorophyll. As the result, chlorophyll concentration [Chl], mg/m^3, has been used as the proxy data to quantify the phytoplankton biomass in the ocean waters. The sheer size of the ocean and the costs associated with its in situ sampling has led to the deployment of satellite ocean color missions [42, 53, 54]. These global determinations of the upper ocean chlorophyll distribution have produced the first consistent views of the space/time dynamics of the ocean biosphere [42, 55]. Figure 2.1 shows the [Chl] maps of the Long Island Sound and the vicinity areas for the different seasons of the year exhibiting the seasonal variability in phytoplankton biomass of the area.

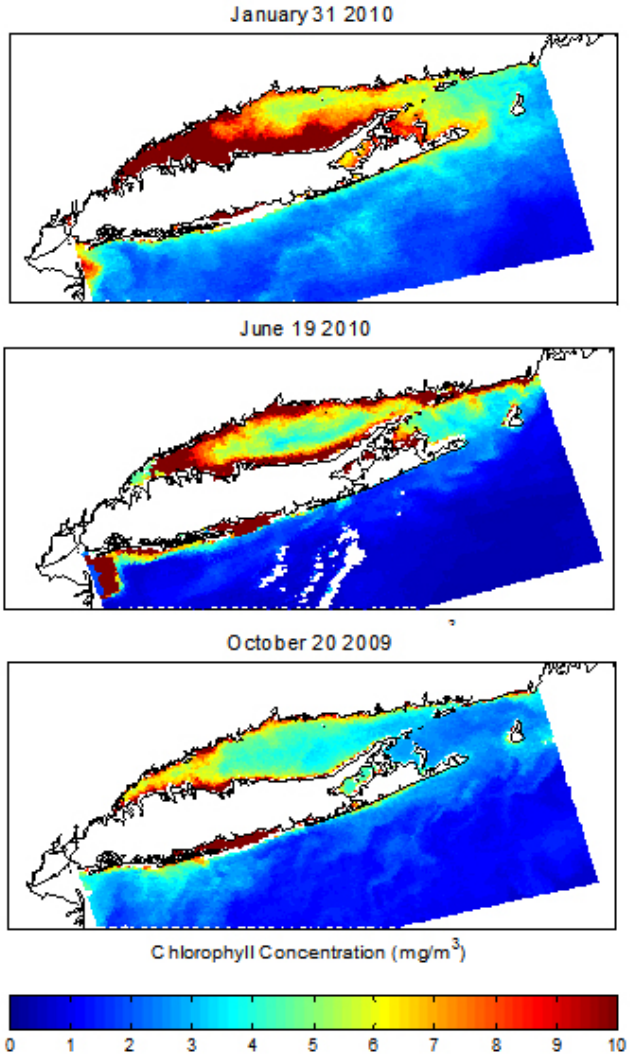

Figure 2-1. Chlorophyll concentration [Chl], mg/m^3, of the Long Island Sound and vicinity areas for different times of the year. [Chl] images are retrieved from the Level 2 MODIS data of AQUA satellite.

Other indicators of the biogeochemical process of the sea waters such as the color dissolved organic matter (CDOM) and sediment concentration can be also effectively assessed from the OC data [10, 56, 57]. In addition to the geophysical products like these, OC data images can also be directly derived into the basic optical properties, such as absorption and backscattering of the water body with the use of the inversion algorithms [58, 59]. These optical properties can then be

related to the events occurred naturally or resulted from the anthropogenic impacts for the further understanding of the phenomenon. For example, particulate backscattering coefficients and the mineral concentration are known to be strongly correlated [60]. As the result, backscattering coefficients of the water body can be used as the proxy for the discharge of the sediment flow which is usually abundant with the mineral rich particles.

Figure 2.2 exhibits particulate back-scattering coefficient maps of the Long Island Sound and its vicinity areas for three particular days (March 9, 16 and 20 of the year 2010). The particulate back-scattering coefficient of these satellite images are obtained by using the Quasi Analytical Algorithm (QAA) [59]. In fact, these three images were recorded before and after the severe storm event occurred in New York region on March 14 of 2010. The images clearly show the flows of the sediment discharged from the rivers of the area demonstrating the potentials to make the assessments to the extent and impact of the storm.

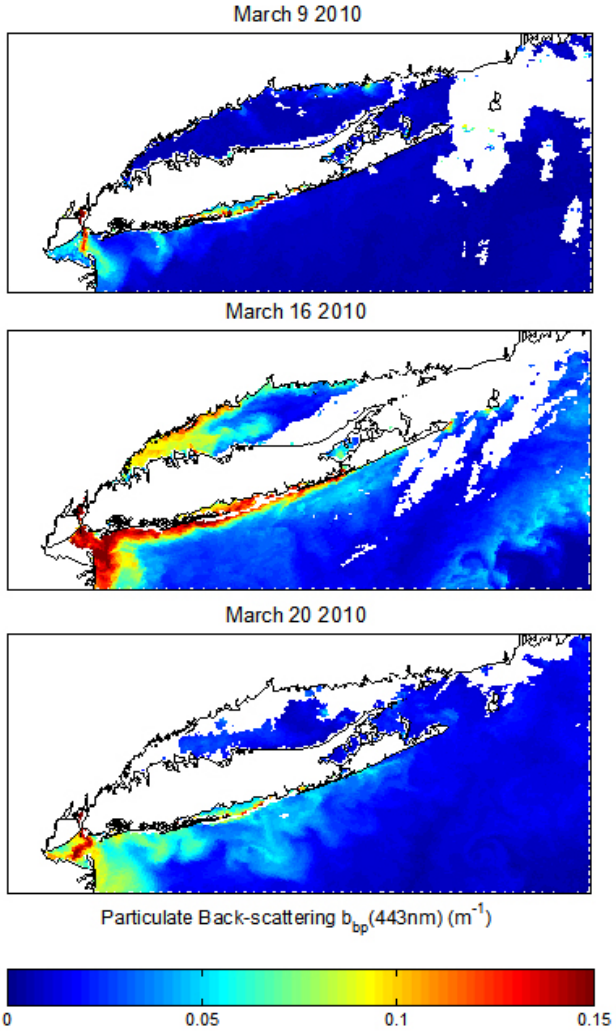

Figure 2-2. Maps of the particulate back-scattering coefficient at 443nm for Long Island Sound and its vicinity areas. b_{bp} images shown above are retrieved from the Level 2 MODIS data of AQUA satellite.

2.3 Processing of the Satellite Ocean Color Radiometric Data

It is well recognized that about 90% of the signal measured by an ocean color satellite sensor is resulted from the confounding influence of the atmosphere [11]. Reflected light from ocean surface also contributes noticeably to the total radiance measurement made from top of the

atmosphere [61]. The atmospheric and ocean surface effects must be removed before ocean radiance signals can be analyzed for the purposes of understanding the ocean biosphere and doing so requires the multiple rigorous processing steps [61]. This section of the chapter mainly addresses the fundamental radiometric quantities that are used in the ocean color remote sensing and derivation of those quantities from the top of the atmosphere measurements, detailing the processing procedures at each derivation step.

2.3.1 Top of atmosphere (TOA) radiance

Retrieving of the water leaving radiance data which carries the information of the optically active constituents of the seawater accurately from the total radiance data measured by the satellite sensor is the one of the main objectives in the Ocean Color data processing [11, 61, 62]. The water leaving radiance, L_w (mW/cm^2/μm/sr), which propagates in upward direction through the atmosphere, is modified by the atmosphere through absorption and scattering and exits the top of the atmosphere, where it is measured by the space borne ocean color sensor. In general, the radiance exiting the top of the atmosphere (TOA) in an arbitrary direction, denoted as Ω, in a spectral band centered at λ, $L_{Total}(\Omega, \lambda)$ can be written as follows:

$$L_{Total}(\Omega,\lambda) = L_r(\Omega,\lambda) + L_a(\Omega,\lambda) + L_{ra}(\Omega,\lambda) + L_s^{TOA}(\Omega,\lambda) + L_w^{TOA}(\Omega,\lambda) \quad (2.1)$$

where L_r represents the radiance resulting from the scattering by air molecules (Rayleigh scattering), L_a similarly is the radiance resulting from scattering by aerosols in the absence of air, L_{ra} is the resulting radiance due to interaction between molecular and aerosol scattering, L_s^{TOA} and L_w^{TOA} are the radiance specularly reflected from the direct solar beam at the ruffled ocean surface, and the water-leaving radiance that were transmitted to the top of the atmosphere. In equation 2.1, L_r, L_a , and L_{ra} are the contribution of the solar photons which are scattered to the

sensor direction along the path through atmosphere, and the summation of them are called usually atmospheric path radiance, L_{path}. These atmospheric path radiance (L_{path}) and air sea surface reflected radiance (L_s^{TOA}) typically constitute 80-90% of the total radiance seen by a satellite when looking at the ocean, only 10-20% of the signal comes from the water [11, 62].

2.3.2 Atmospheric correction procedures

Atmospheric correction procedures estimate L_{path} as well as L_s^{TOA}, and remove it from the total radiance, L_{Total}, measured by sensor obtaining an estimate of the water-leaving radiance that was transmitted to the top of the atmosphere, L_w^{TOA}. However, algorithms for estimating the IOPs of the water are based on the water-leaving radiance at the water surface, L_w, not at the TOA. On the other hand, L_w can be related to the L_w^{TOA} through the diffuse transmittance of the atmosphere in the sea surface to sensor direction, t_d, as described in the following equation.

$$L_w(\Omega,\lambda) = \frac{L_w^{TOA}(\Omega,\lambda)}{t_d(\Omega,\lambda)} \tag{2.2}$$

The equation (2.1) and (2.2) imply that retrieving L_w from the total radiance measured by the space borne sensor, L_{Total}, is not straightforward requiring the precise estimations of the L_{path}, L_s^{TOA} and t_d which in turn also need the extensive information of the atmospheric optical properties.

To achieve the task of estimating atmospheric and sea surface reflected radiances contribution in the total radiance measurements and atmospheric diffuse transmittance parameter (t_d) in order to produce estimates of the water-leaving spectrum, different atmospheric correction algorithms have been implemented since the early eighties for open ocean waters [11, 12, 62-64]. Most of these algorithms assume that the water-leaving radiance is negligible in the near-infrared (NIR)

part of the spectrum to determine the atmospheric optical properties and subsequently estimate the water-leaving radiance. However, this assumption may break down for the coastal waters with highly turbid conditions whose optically active constituents might produce significant scattering in the NIR region. New modalities of the atmospheric correction algorithms have been accordingly developed to adjust the NIR water-leaving contribution in the overall data processing. The atmospheric correction step is the one of the most important steps in OC data processing. Although detail analysis of the atmospheric correction procedures in the OC data processing is beyond the scope of this research, some of atmospheric correction issues associated with the in-situ measurements and OC satellite data validation activities will be addressed briefly in the following sections.

2.3.3 Normalization step to remove the environmental effects

In the processing of the ocean color radiometric data, the spatial and temporal consistency of spectral radiance data is of crucial importance. In other words, obtaining the standardized L_w data which ideally varies only with the IOP of the seawater is the prerequisite when data observed within a satellite sensor swath, along the orbit, or viewed during successive days, or by various sensors in flight, are to be compared [65, 66]. In fact, one of the main goals of the International Ocean Color Coordinating Group (IOCCG) is to achieve the data processing procedures that will enable the merging of the ocean color data (such as concentrations of chlorophyll and sediment) captured by several instruments operating simultaneously and, from that, to generate the reliable global time series ocean color satellite imageries [53]. Therefore, resulting L_w data of the equation (2.2) must be further processed into standardized form (i.e. the water leaving radiance data which is not influenced by the factors such as varying illumination conditions due to the seasonal as well as natural environmental changes and observational conditions which depend on

the illumination and viewing geometries). This standardization is the requirement especially when in situ field data are to be compared with the data captured from the space borne sensor. Consequently, the concept of spectral "normalized water-leaving radiance," denoted as $nLw(\lambda)$ was introduced by Gordon and Clark in an attempt to fulfill this requirement [67, 68]. The rationale is to produce the standardized hypothetical water leaving radiances that are independent from the environmental conditions and observation geometries at the instant of measurement. In the processing, the environmental influences are firstly removed by forming the following intermediate quantity:

$$L_{wN}(\theta_s, \theta_v, \phi, \lambda) = \frac{L_w(\theta_s, \theta_v, \phi, \lambda)}{E_d(\theta_s, \lambda)} \times F_0(\lambda) \tag{2.3}$$

In the above equation, the water-leaving radiance, L_w, has been written in the more precise form in which its arguments being wavelength, λ, the direction of the exiting water leaving radiance (the same as the viewing zenith angle), θ_v, sensor's relative azimuth angle from the Sun's direction φ, and the solar zenith angle, θ_s. The convention used for φ throughout this thesis is φ = 0° when the sensor is in opposition with the Sun and φ = 180° when the Sun is behind the sensor. It should be recalled here that L_w has been described only as the function of its direction, denoted as Ω and λ up until now. In fact, for any instantaneous observation, measured radiance data at a given wavelength λ can be completely described by its own direction and quantity. Nevertheless, this may no longer be sufficient if those measurements were to be comparable with other measurements taken under varying environmental, illumination and observation conditions. Therefore, the standardization (normalization) process requires the information regarding the environmental conditions as well as observation geometries of the instant at which the radiance measurement is made.

In the equation (2.3) $F_0(\lambda)$ is the extraterrestrial solar irradiance (i.e. solar flux at the top of the atmosphere) measured in mW/cm^2/μm. In contrast, E_d is the down-welling irradiance just above the sea surface also measured in mW/cm^2/μm and it is a function of the solar zenith angle, θ_s, and the wavelength λ. As E_d by definition is the measurement that were to be made just above the sea surface, its quantity cannot be directly determined from the measurements made from space borne ocean color sensors. As the result, it must rather be indirectly derived from the atmospheric parameters as it is governed by the diffuse atmospheric transmittance in the sun to sea surface direction, t_d^*. Derivation of E_d can be described in the following equation:

$$E_d(\theta_s, \lambda) = D^2 t_d^*(\theta_s, \lambda) \cos\theta_s F_0(\lambda) \tag{2.4}$$

The term D^2 in (2.4) accounts for the variation of the Sun-Earth distance with the day of the year in order to compute E_d for the mean Sun-Earth distance there by eliminating the underlying seasonal variation in solar radiation that reaches to earth.

The same L_{wN} quantity can be interpreted in another way: this intermediate normalized water leaving radiance is the hypothetical radiance that would be measured if the Sun were at zenith, in the absence of atmosphere, and when the Earth is at its mean distance from the Sun. In spite of this interpretation L_{wN} is still a quantity depending on observation and illumination geometry [15].

2.3.4 Bidirectional correction to remove angular dependency

Indeed, the water-leaving radiance field emerging from sea water is not generally isotropic because of the nonisotropic character of the volume scattering function (VSF) of the water body, coupled with nonisotropic illumination conditions that generally prevail above the sea surface.

Furthermore, the wavy nature of the water surface also has noticeable influence over the angular distribution of the water leaving radiance field [15-19, 24]. However, the initial quantity L_w has been obtained under specific angular viewing and illumination conditions θ_v, φ, and θ_s. So this angular dependence must be removed and this process is called the bidirectional correction. A way to remove this remaining dependence on the actual geometrical conditions consists of assumption that the observation was ideally made as though the pixel was seen vertically (nadir viewing) and the Sun was at zenith. Practically, it corresponds to carrying out the following operations: (i) deriving the approximate of the *IOP* of water body under observation through the L_{wN}; (ii) estimating the Volume Scattering Function (VSF) of the water body based on the approximated *IOP*; (iii) calculating the angular distribution of the water leaving radiance based on the estimated VSF; (iv) calculating the correction factor (i.e. adjustment to the L_{wN} in order to obtain the radiance field that propagate through the water-air surface to the nadir direction at the hypothetical illumination condition of the Sun at the Zenith) according to the assumed VSF.

The normalized water leaving radiance, *nLw*, is then obtained from L_{wN} by multiplying it with the correction factor as below:

$$nLw(\lambda) = C_{BRDF}(\theta_s, \theta_v, \phi, W, IOP, \lambda) \times \frac{L_w(\theta_s, \theta_v, \phi, \lambda)}{E_d(\theta_s, \lambda)} \times F_0(\lambda) \tag{2.5}$$

In the equation (2.5) C_{BRDF} is the correction factor for the bidirectional effect. It is the function of *IOP* in addition to the geometries (θ_v, φ, and θ_s), sea state defined by the win speed (W) and wavelength (λ).

The anisotropy in the water leaving radiance field has implications, particularly, in the processing of data from ocean-color satellite sensors as well as in calibration-validation activities

for ocean-color sensors in which water-leaving radiances obtained under various geometrical configurations have to be quantitatively and accurately compared [28, 30, 32]. Morel and Gentili developed an approach which relates the bidirectional properties of the water-leaving radiance field to the chlorophyll concentration of the water, and the approach is currently employed in the OC data processing as an operational algorithm [15].

2.3.5 Remote sensing reflectance

Another quantity routinely used in the ocean color remote sensing is remote sensing reflectance, *Rrs*, which is measured in the sr^{-1} unit. *Rrs* is the standard input to many of the derived product algorithms [59, 69]. It is calculated by dividing the normalized water leaving radiance by the $F_0(\lambda)$. Thus, $Rrs(\lambda)$ after the bidirectional angular dependencies are removed can be described as:

$$Rrs(\lambda) = C_{BRDF}(\theta_s, \theta_v, \phi, IOP, \lambda) \times \frac{L_w(\theta_s, \theta_v, \phi, \lambda)}{E_d(\theta_s, \lambda)} \tag{2.6}$$

3 Fundanmental Inherent Optical Properties

3.1 Inherent and apparent optical properties

The optical properties of water can be separated into two categories: inherent and apparent. Inherent optical properties (IOPs) such as absorption and scattering coefficients depend only upon the medium while the apparent optical properties (AOPs) such as reflectance are determined by the medium and the geometric structure of the surrounding light field. The overall optical properties of natural waters are determined, in part, by the optically active constituents in water. The AOPs can be computed through the radiative transfer equation (RTE) or approximations of the RTE from empirical models, using the combined IOPs as inputs. For the analysis purpose, the AOPs are also routely obtained through raidative transfer simulations fed with input IOPs independently modeled for each constituent of the water body [60]. This chapter is devoted to the derivation and phyical meaning of the basic optical properties, namely absorption, scattering, attenuation and the scattering phase function of the water body that will be used in the paper from this point forward.

3.2 Basic inherent optical properties

Two of the fundamental IOP's are the absorption coefficient and the volume scattering function. Consider a small volume ΔV of water with thickness Δr, illuminated by a narrow collimated beam of monochromatic light with spectral radiant power $P_i(\lambda)$, Wnm^{-1}, as schematically illustrated in Figure 3.1. Some part of incident power is absorbed within the volume of water $P_a(\lambda)$; some part is scattered out of the beam at an angle ψ, $P_s(\psi, \lambda)$; and the remaining light, $P_t(\lambda)$, propagates in the same direction as the insistent light and transmitted through the volume.

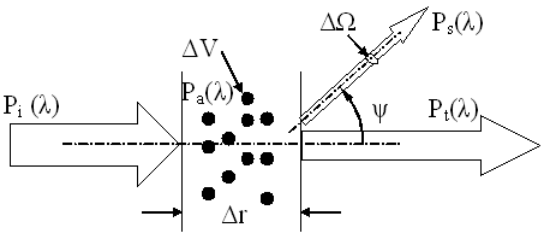

Figure 3-1. Illustration of the IOP parameters

3.2.1 Absorption coefficient

The spectral absorption coefficient is defined as the fraction of incident power that has been absorbed per unit length and defined as follows:

$$a(\lambda) = \lim_{\Delta r \to 0} \frac{P_a(\lambda)}{P_i(\lambda)\Delta r} \qquad m^{-1} \tag{3.1}$$

3.2.2 Volume scattering function

The angular scattered power per unit length and unit solid angle when normalized to the incident power is defined as volume scattering function (VSF), customarily written as $\beta(\psi,\lambda)$ ($m^{-1}sr^{-1}$), which is a function of the angle between the directions of incident and scattered light, ψ (ψ varies from 0 to π):

$$\beta(\psi,\lambda) = \lim_{\Delta r, \Delta\Omega \to 0} \frac{P_s(\psi,\lambda)}{P_i(\lambda)\Delta r \Delta\Omega} \qquad m^{-1}sr^{-1} \tag{3.2}$$

3.2.3 Scattering coefficient

Integration of $\beta(\psi,\lambda)$ over the 4π space is the total fraction of incident power per unit distance that has been scattered, and is defined as the scattering coefficient $b(\lambda)$:

$$b(\lambda) = \lim_{\Delta r \to 0} \frac{P_s(\psi, \lambda)}{P_i(\lambda)\Delta r} = \int_{4\pi} \beta(\psi; \lambda) d\Omega = 2\pi \int_0^{\pi} \beta(\psi; \lambda) \sin\psi d\psi \quad m^{-1} \tag{3.3}$$

3.2.4 Attenuation coefficient

The attenuation coefficient $c(\lambda)$ is defined as:

$$c(\lambda) = a(\lambda) + b(\lambda) \qquad m^{-1} \tag{3.4}$$

which describes the fraction of incident power loss per unit distance, either absorbed or scattered.

If a water body contains several different substances which have scattering or absorption coefficient a_i, b_i for the i^{th} substances, then a or b of the whole water body is simply the addition of all of a_i or b_i:

$$a = \sum_i a_i \text{ and } b = \sum_i b_i \tag{3.5}$$

Similar approaches can be also applied to the attenuation coefficient c.

3.3 Spectral scattering phase function

The spectral scattering phase function (SPF), denoted as $\overline{\beta}(\psi, \lambda)$, is defined by:

$$\overline{\beta}(\psi, \lambda) = \frac{\beta(\psi, \lambda)}{b(\lambda)} \qquad (\text{sr}^{-1}) \tag{3.6}$$

Writing the volume scattering function $\beta(\psi, \lambda)$ as the product of the scattering coefficient $b(\lambda)$ and the phase function $\overline{\beta}(\psi, \lambda)$ partitions $\beta(\psi, \lambda)$ into a factor giving the strength of the scattering, $b(\lambda)$ with units of m^{-1}, and a factor giving the angular distribution of the scattered

photons, $\bar{\beta}(\psi,\lambda)$ with units of sr^{-1}. Combining equation (3) and (6) gives the normalization condition for the phase function:

$$2\pi \int_0^{\pi} \bar{\beta}(\psi,\lambda)\sin\psi d\psi \quad = 1 \tag{3.7}$$

The IOPs as just defined give us a full description of the optical properties of a water body as needed for the interpretation and prediction of underwater light fields within the framework of radiative transfer theory.

4 Long Island Sound Coastal Observatory for Ocean Color Data Validation

4.1 Background of Ocean Color Data Validation

The accurate determination of satellite retrieved $L_w(\lambda)$ values requires the absolute calibration of the space sensor, precise removal of the atmospheric and sea surface perturbing effects, and proper correction for the angular dependencies resulted from bidirectional properties of water. The accuracy of the absolute calibration and the effectiveness of the atmospheric and bidirectional correction can be determined by comparing contemporaneous satellite derived and in situ $L_w(\lambda)$ data or, alternatively, derived quantities like the normalized water leaving radiance $nLw(\lambda)$ and remote sensing reflectance $Rrs(\lambda)$. The generalized process of ground truth comparison under a wide range of environmental conditions is usually called validation. The validation and merging of remote sensing products from different satellite OC sensors require accurate, frequent, globally-distributed and highly consistent in-situ measurements of $nLw(\lambda)$. This requirement led to idea of developing a network of consolidated above-water autonomous radiometers operated at sites encompassing distinct water types suitable for satellite ocean color validation activities in coastal regions [29]. In particular, the objective is to generate in-situ datasets which are representative of various marine trophic regimes by relying on standardized measurements obtained with identical instruments, protocols, calibration facility and processing code. This approach is expected to lessen potential inconsistencies inherent to global data sets of in situ measurements so far obtained by grouping data from several independent sources intrinsically affected by uncertainties due to different field instruments, diverse sampling methods, a variety of calibration sources and protocols, and assorted processing schemes [70].

In fact, a network of sites for Earth Observation (EO) satellite sensor validation have already been established since early 1990 in the form of globally-distributed autonomous robotic sun-photometers to support atmospheric studies at various scales through standardized measurements of the direct sun irradiance and sky-radiance [35]. The so called Aerosol Robotic Network (AERONET) which is made up of the identical robotic sun-photometers, offers the regional to global scale aerosol monitoring and characterization and has been instrumental to the investigation of aerosol optical properties, the creation of global aerosol climatology, and the validation of atmospheric remote sensing products. Since 2006, the network has been expanded through a new component called AERONET – Ocean Color (AERONET-OC) which provides the additional capability of determining the radiance emerging from the sea from which the normalized water-leaving radiance, $nLw(\lambda)$, is derived with modified sun-photometers installed on offshore fixed platforms. The ultimate purpose of AERONET – OC is the production of standardized measurements performed at different sites with identical measuring systems and protocols, calibrated using a single reference source and method, and processed with the same code to provide the reliable data stream of $nLw(\lambda)$ for OC data validation [28].

4.2 Long Island Sound Coastal Observatory (LISCO)

In order to support present and future multi- and hyper-spectral calibration/validation activities for the Ocean Color Radiometry satellites, as well as the development of new measurements and retrieval techniques for coastal waters, City College of New York along with Naval Research Laboratory has established a scientifically comprehensive observational platform, Long Island Sound Coastal Observatory (LISCO). LISCO is an integral part of the NASA AERONET – OC Network which has been designed to support long-term satellite ocean color investigations

through cross-site consistent and accurate measurements collected by autonomous radiometer systems deployed on offshore fixed platforms and achieving measurements from above water [37]. In addition to the standard AERONET-OC multispectral SeaPRISM instrument, LISCO expands observational capabilities for the continuous monitoring and assessment of the hyperspectral and polarized properties of coastal waters through HyperSAS sensor suite.

In this section, characteristics of the LISCO and its measurement systems will be detailed along with the above-water data acquisition systems and processing procedures employed in the OC satellite data validation activities.

4.2.1 LISCO location

The Long Island Sound Coastal Observatory (LISCO) platform is located at around 3 km from the shore of Long Island near Northport, NY, USA. The coordinates of the site are N 40º57'16", W 73º20'30" [Figure 4.1.(a)]. The bathymetry in the immediate vicinity of the platform exhibits a plateau at around 13 meters depth [Figure 4.1.(b)]. LISCO is located in the area of western Long Island Sound which is usually moderately turbid, very productive and principally driven by phytoplankton biomass and associated detrital materials, rather than suspended sediments. Steady surface currents in the LISCO area are around 0.3 m s^{-1} in average according to NOAA HF Radar dataset.

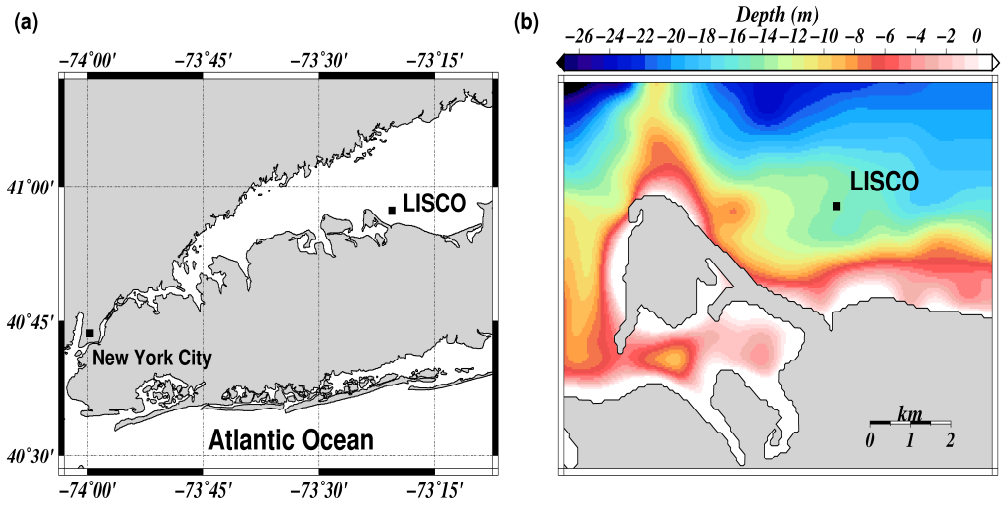

Figure 4-1. (a) Long Island Sound Coastal Observatory (LISCO) map (LISCO coordinates N40.955°; W73.342°). (b) LISCO site bathymetry derived from the General Bathymetric Chart of the Oceans (GEBCO) dataset.

4.2.2 LISCO Instrumentation

The platform combines a multispectral SeaPRISM system (CIMEL ELECTRONIQUE, France) as a part of AERONET – OC Network [29-31], with a co-located hyperspectral HyperSAS system (Satlantic Inc, Canada). The instruments are positioned on a retractable tower on the platform with an elevation of 12m. Both instruments were installed on the LISCO platform in October 2009 and have been providing data since then. Figure 4.2 illustrates LISCO's retractable instrument tower with its instrument panel at the top, and the solar panel which generates the electricity for the operation of the instruments.

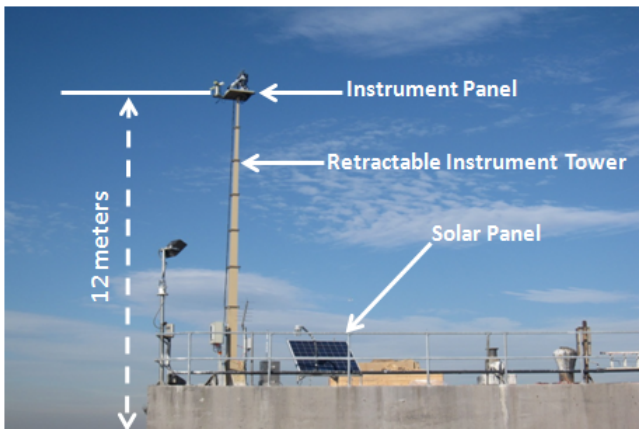

Figure 4-2. Illustration of LISCO tower.

4.2.2.1 SeaPRISM system

SeaPRISM system is made up of CE-318 sun photometers (see Figure 4.3) modified to meet requirements for above-water radiometry [32]. The photometers perform radiance measurements with a full-angle field of view of 1.2° to determine the total radiance from the sea, $L_T(\theta_s, \theta_v, \varphi, \lambda)$, and the sky, $L_i(\theta_s, \theta'_v, \varphi, \lambda)$, for the relative azimuth angle with respect to the sun φ and the respective viewing angles θ_v and θ'_v with $\theta'_v = \pi - \theta_v$. With the use of the programmable robotic arm of SeaPRISM, the azimuth φ is always set to 90° regardless the sun position; the downwards viewing angle θ_v is set to 40° from the nadir position. These values were determined in order to minimize the perturbations resulting from the sun glint of the sea surface [71] and the deployment superstructure itself or its shadow [30, 72].

Figure 4-3. SeaPRISM instrument.

The instrument acquires the measurements at seven wavelengths performing one channel at a time by sequentially moving a filter wheel. Each measurement sequence consists of 3 sky and 11 sea measurements and the execution of a complete measurement sequence takes approximately 6 minutes.

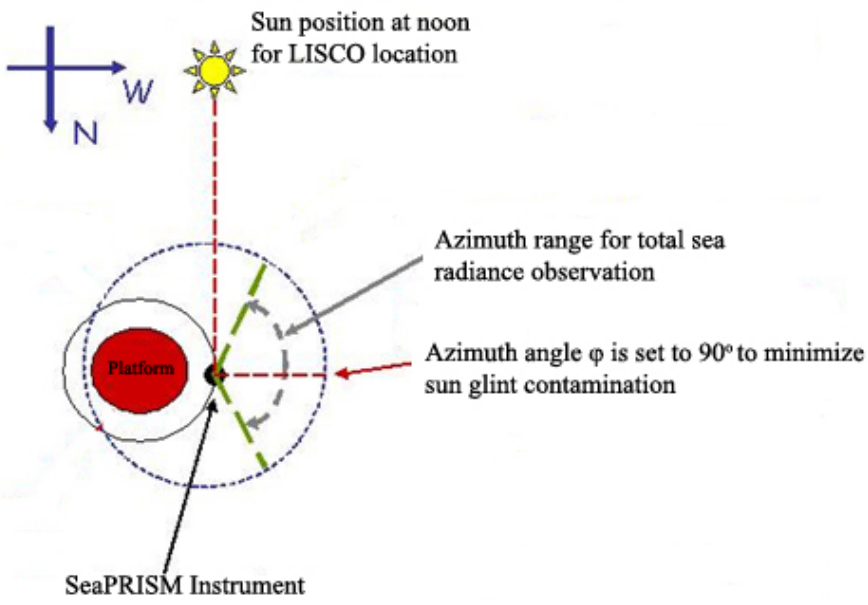

Figure 4-4. Top view of the deployment strategy of the SeaPRISM system.

The SeaPRISM system configuration of LISCO performs ocean color measurements at the 412, 443, 491, 551, 668, 870 and 1018 nm center wavelengths. These center wavelengths were selected to be as close as possible to the bands of current ocean color EO systems [2, 39, 48] in order to support essential validation activities. In addition to these ocean color measurements, the regular data acquisition of AERONET are achieved which enables retrievals of the aerosol optical thickness and the fine-coarse aerosol mode fraction [73].

4.2.2.2 HyperSAS system

Figure 4-5. Hyperspectral radiance sensors of HyperSAS system.

The hyperspectral measurements are achieved by a HyperSAS system providing high precision hyperspectral measurements of total spectral radiance from the sea and the sky. The radiance and irradiance measurements of HyperSAS system are achieved for 180 channels regularly spaced between 305 and 905 nm. Two radiance sensors (see figure 4.5) are mounted on the same location as SeaPRISM system and have a full-angle field of view of 3°. Consequently, the sea target sensed by HyperSAS is slightly larger than the SeaPRISM one. These radiance sensors provide the total sea measurement, $L_T(\theta_s, \theta_v, \varphi, \lambda)$, and the sky, $L_i(\theta_s, \theta'_v, \varphi, \lambda)$, for a fixed geometrical configuration with $\theta = 40°$ from the nadir view and pointing exactly westwards. As a result, the relative azimuth φ is changing with respect to the sun position. Thus, SeaPRISM and

HyperSAS point at the same area when the Sun is southward in other words around 12:00 PM local time (LT). In addition to the radiance sensors, HyperSAS system also include a hyper-spectral irradiance sensor to make down-welling irradiance, $E_d(\theta_s,\lambda)$, measurements. Furthermore, three customized hyperspectral HyperSAS systems (HyperSAS-POL) were added to LISCO platform in June 2010 enabling polarization measurements.

4.2.2.3 Calibration and data acquisition

Each HyperSAS and SeaPRISM sea-viewing measurement sequence is executed every 30 min within plus or minus 4 hours of 12:00 PM LT. SeaPRISM data are transferred by the satellite link to NASA, processed by the NASA AERONET group and posted on the NASA AERONET website [74]. The near-real-time transmission of HyperSAS data is achieved by broadband cellular service to the CCNY server. The calibration of the SeaPRISM sun-photometer is carried out by NASA in the standard way of AERONET-OC. The HyperSAS system calibration is carried out by Satlantic, Inc. The recalibration of the HyperSAS sensors has shown a radiometric stability over a time period of approximately 9 month better than 0.5%.

4.3 Above Water Data Processing

4.3.1 Decomposition of the above water radiometric data

The most common above-water methods for producing $L_w(\lambda)$ make use of measurements of the total radiance $L_T(\theta_s, \theta_v, \varphi, \lambda)$ taken while pointing a radiance sensor at the sea [71]. However, the radiance sensor pointing toward the sea surface in θ_v and φ direction measures the sum of the water-leaving radiance, L_w, and any incident sky radiance that has been reflected by the sea surface into θ_v and φ direction. Therefore precise retrieval of L_w entirely depends on the accurate estimation of the contribution of the surface reflected radiance, denoted as L_{ref}, in the L_T

measurement. L_{ref} can be related to the incident sky radiance, L_i, measured in the direction of $\theta'_v = \pi - \theta_v$ and φ, by deploying a radiance sensor pointing toward the sky, through the surface reflection coefficient ρ. Therefore, L_w, in principle, can be derived from two simultaneous measurements (i.e. $L_T(\theta_s, \theta_v, \varphi, \lambda)$ and $L_i(\theta_s, \theta'_v, \varphi, \lambda)$) taken by deploying the two radiance sensors concurrently with the geometrical configuration mentioned above and can be described with the following equation [71]:

$$L_w(\theta_s, \theta_v, \phi, \lambda) = L_T(\theta_s, \theta_v, \phi, \lambda) - \rho(\theta_v) \cdot L_i(\theta_s, \theta'_v, \phi, \lambda) \quad (4.1)$$

In the above equation surface reflection coefficient, ρ, can be easily calculated via the Fresnel equation for the given θ_v with the use of the known refractive index of water if the flat water surface is assumed. However, in reality, sea surface is not flat; it is roughened by the wind-blown surface wave and gravity wave. Therefore, calculation of ρ is not straightforward, it requires taking into account the varying slope of the facets of the wavy sea surface which effectively change the sensor viewing angle within the sensor field of view (FOV). Because of the wavy sea surface, sky radiance in any downward direction can in principle be reflected into the detector and this may result in erroneous retrieval of L_w especially when the sky radiance distribution is not uniform throughout the hemisphere.

Consequently, ρ depends not only on direction, wavelength (λ), and wind speed (W), but also on the detector FOV and on the sky radiance distribution. Although ρ is sometimes called the Fresnel reflectance, this is incorrect terminology: ρ depends on, but in general does not equal, the Fresnel reflectance of the surface at viewing angle θ_v. Consequently, ρ should be viewed simply as non-dimensional quantity whose functional dependence can be expressed as ρ (θ_s, θ_v, φ, W, λ) [71].

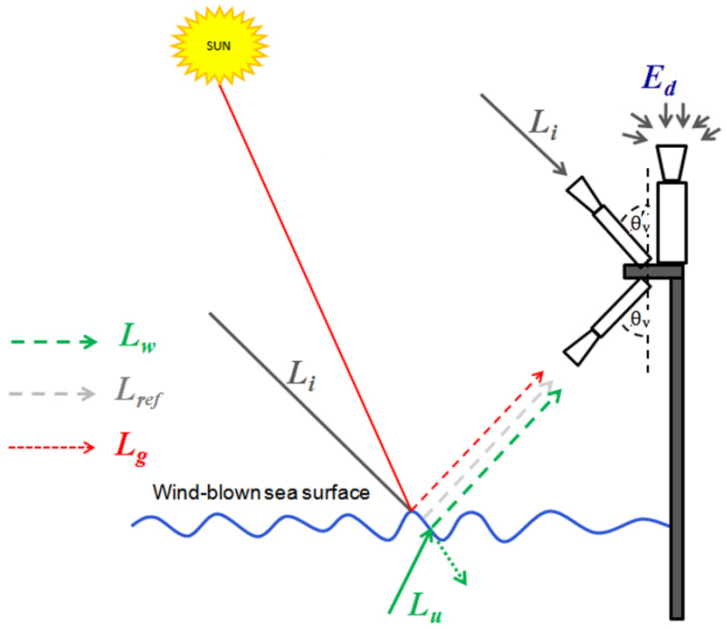

Figure 4-6. Illustration of the above water radiometric system installed on an offshore tower which includes two radiance sensors, one pointing upward toward sky to measure L_i and another downward toward sea to measure L_T, together with an irradiance sensor for down-welling irradiance, E_d, measurement. Three components of total radiance, L_w (green), L_{ref} (gray) and L_g (red), are shown in dotted lines together with the underwater upwelling radiance L_u (solid green line).

In addition, glint radiances which are mostly produced by the perturbations of the surface wave (i.e. solar and sky radiance, which are not from the pointing direction of the sky radiance sensor, directly reflected in the direction of the water viewing sensor FOV) and whose spectral shape significantly differs from that of L_i may also have compounding effects on the retrieval of L_w [75]. If present, these so called glint radiance, L_g, adds the offset spectra to the measured total radiance. Determination of L_g contribution to L_t spectral is also complicated because it depends

on the atmospheric conditions, solar position and statistics of the wave slopes which in turn require the exact knowledge of the wind direction and speed [36].

With the considerations mentioned above, equation (4.1) in general should be rewritten in the realistic form as below:

$$L_w(\theta_s,\theta_v,\phi,\lambda) = L_T(\theta_s,\theta_v,\phi,\lambda) - \rho(\theta_s,\theta_v,\phi,W,\lambda)\cdot L_i(\theta_s,\theta_v',\phi,\lambda) - L_g(\theta_s,\theta_v,\phi,W,\lambda) \qquad (4.2)$$

4.3.2 Surface reflectance factor ρ

Various attempts have been made in order to estimate ρ in the equation above [71]. Notably, Austin presents tables of ρ computed for various wind speeds, solar angles, and viewing angles using the Cox–Munk capillary wave-slope statistics [76]. Mobley also generated the look up tables of ρ for the whole range of illumination and viewing geometries for different wind speeds using Hydrolight radiative transfer simulation software assuming uniform sky radiance distribution [71, 77]. These look up tables are adopted as the standard protocol for the estimation of ρ by ocean color community and currently being employed in the retrieval algorithms for above water ocean color data processing. Figure 4.7 presents the simulated ρ values at the fixed viewing angle (θ_v = 40^o) as the function of solar angles (θ_s) for two relative azimuth angles (φ = 90^o and 135^o) and three wind speeds (W = 0, 5 and 10 ms^{-1}). In the figure, it can be observed that ρ values for the different wind speeds at every sun positions significantly differ from each other underscoring the importance of the precise determination of sea state in the retrieval process of L_w.

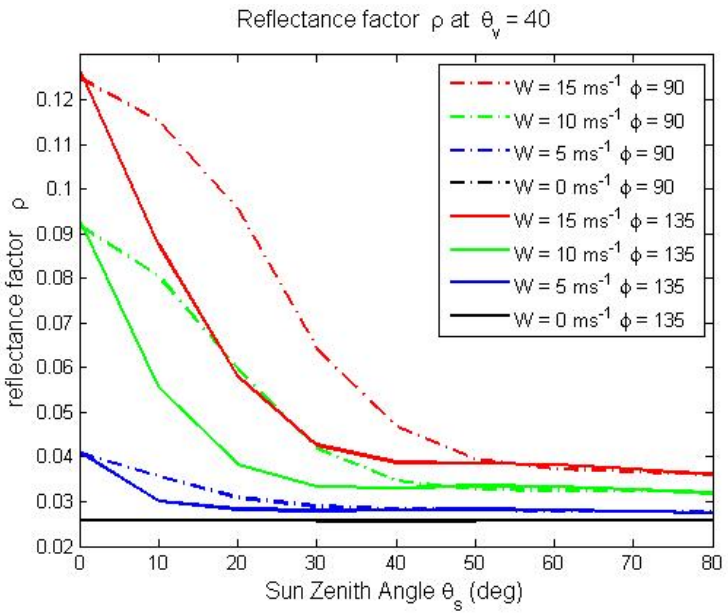

Figure 4-7. Hydrolight simulated ρ values at the fixed viewing angle (θ_v = 40^o) as the function of solar angles (θ_s) for two relative azimuth angles (φ = 90^o and 135^o) and three wind speeds (W = 0, 5 and 10 ms^{-1}).

4.3.3 Removal of the surface wave perturbation effect

As shown in equation (4.2), glint radiance spectrum, L_g (λ), resulted from the surface wave perturbation depends not only on the viewing and illumination geometries but also on the wind speed which is used to approximate the statistics of the randomly fluctuating wave slopes. However, in the current operational above water processing for the validation of OC satellite sensors, L_g is estimated by employing a simple approach which makes use of the multiple successive total radiance measurements [28, 30, 32, 78]. In the approach successive L_T spectral measurements are taken within a short (two to three minutes) period, then, only few lowest (5 to 20 % of the total number of measurements) are considered to be qualified for further processing discarding the high total sea radiance measurements assuming they are affected by the glints due

to wave perturbation. After that, average of the qualified total sea radiance measurement, denoted as, L^*_T, is considered free of glint contamination and further processed for the sky glint removal step. Thus, L_w can be described in the following form:

$$L_w(\theta_s,\theta_v,\phi,\lambda) = L_T^*(\theta_s,\theta_v,\phi,\lambda) - \rho(\theta_s,\theta_v,\phi,W,\lambda)\cdot L_i(\theta_s,\theta_v',\phi,\lambda) \tag{4.3}$$

Although this glint filtering procedure, which makes use of the lowest total sea radiance measurements only in the removal of the glint radiance resulted from the surface wave perturbation, provides the simple and straight forward way of retrieving L_w, the effectiveness of the approach may also vary with the sensor FOV and integration time. Consequently, detailed analysis of this approach has been performed with the use of the coincident above water measurements obtained from the co-located instruments at LISCO. This analysis will be further discussed in chapter 5.

4.3.4 Normalized water leaving radiance and remote sensing reflectance

As discussed in chapter 2, the normalized water leaving radiance, *nLw*, and remote sensing reflectance *Rrs* are calculated as follows:

$$nLw(\lambda) = C_{BRDF}(\theta_s,\theta_v,\phi,IOP,\lambda)\times\frac{L_w(\theta_s,\theta_v,\phi,\lambda)}{E_d(\theta_s,\lambda)}\times F_0(\lambda) \tag{4.4}$$

$$Rrs(\lambda) = C_{BRDF}(\theta_s,\theta_v,\phi,IOP,\lambda)\times\frac{L_w(\theta_s,\theta_v,\phi,\lambda)}{E_d(\theta_s,\lambda)} \tag{4.5}$$

where C_{BRDF} is the correction factor for the bidirectional effect.

In the above equations, down-welling irradiance E_d carries the information of the environmental conditions which prevail above the water surface. Therefore, accurate determination of

standardized *nLw* and *Rrs* data which are free of environmental effects and vary only as the function of water constituents entirely depends on the precise E_d measurements. HyperSAS instrument makes the direct measurements of E_d in hyper-spectral scales via vertically installed irradiance sensor. However, in the case of SeaPRISM, E_d has to be derived from the diffuse atmospheric transmittance, $t_d(\lambda)$, and it is calculated as follows in agreement with [29]:

$$t_d(\lambda) = \exp\left(-\frac{(1-\eta_R(\lambda))\tau_R(\lambda) + (1-\omega_A(\lambda)\eta_A(\lambda))\tau_A(\lambda) + \tau_O(\lambda)}{\cos\theta_s}\right) \tag{4.6}$$

where τ_R, τ_A, and τ_O are the Rayleigh, aerosol, and ozone optical thicknesses, respectively; ω_A is the aerosol single scattering albedo; and, η_R and η_A are the Rayleigh and aerosol forward scattering probabilities. $\tau_R(\lambda)$ quantity can be related to the atmospheric pressure and calculated, as in [79, 80] by the following equation:

$$\tau_R(\lambda) = \frac{p(\alpha + \beta \cdot H)}{p_0} \cdot \lambda^{-(3.916+0.074\lambda+0.05/\lambda)} \tag{4.7}$$

where p is the station pressure in mb, p_0 = 1013.26 mb and H is the elevation in kilometers. α and β are atmosphere model- dependent constants tabulated as a function of latitude and season. α and β values for LISCO site are 8.3781 and 0.0036 for winter and 8.3827 and 0.0069 for summer weather. Rayleigh forward scattering probability, η_R, is taken as a constant and equal to 0.52 [29]. The quantity $\omega_A\eta_A(\lambda)$ is also assumed to be spectrally constant and the value is set to be 0.16.

$\tau_A(\lambda)$ is computed applying the Ångström equation using the coefficients produced from series of sky radiance and direct solar irradiance SeaPRISM measurements. The ozone optical thickness,

$\tau_O(\lambda)$, data is obtained from the Total Ozone Mapping Spectrometer (TOMS). Then $t_d(\lambda)$ is related to the down welling irradiance, $E_d(\lambda)$, as follows:

$$E_d(\lambda) = D^2 F_0(\lambda) \cdot t_d(\lambda) \cdot \cos(\theta_s) \tag{4.8}$$

where D^2 term takes into account for earth-sun distance adjustment and F_0 is mean solar irradiance at the top of the atmosphere. Therefore, for the SeaPRISM instrument, equation (4.4) and (4.5) can be rewritten into following form:

$$nLw(\lambda) = C_{BRDF}(\theta_s, \theta_v, \phi, IOP, \lambda) \times \frac{L_w(\theta_s, \theta_v, \phi, \lambda)}{D^2 t_d(\lambda) \cdot \cos(\theta_s)} \tag{4.9}$$

$$Rrs(\lambda) = C_{BRDF}(\theta_s, \theta_v, \phi, IOP, \lambda) \times \frac{L_w(\theta_s, \theta_v, \phi, \lambda)}{D^2 F_0(\lambda) \cdot t_d(\lambda) \cdot \cos(\theta_s)} \tag{4.10}$$

In the current operational OC data processing procedure, bidirectional correction factor $C_{BRDF}(\theta_s,\theta_v,\varphi,IOP,\lambda)$ is calculated with the use of the coefficients obtained from the series of lookup tables based on the estimated chlorophyll concentration [15]. This current operational algorithm is developed based on the single phytoplankton particulate type assumption and, as the result, optimized for open ocean waters. Validity of the use of this algorithm in coastal water conditions has never been verified. Analysis and assessments of the implications resulting from the use of case 1 water optimized correction algorithm in case 2 conditions like LISCO's location which typically exhibits coastal water characteristics will be detailed in chapter 7.

5 Assessment of Above Surface Water Leaving Radiance Measurement Uncertainties Using Collocated Multi and Hyper-spectral Sensors of LISCO

5.1 Above water measurement uncertainties

As discussed in chapter 4, one of the major difficulties of above-water measurements is to correct the observations from the reflected sunlight and skylight components [78], which are randomly fluctuating with the effect of surface waves. These fluctuations induce different geophysical noise that needs to be removed from SeaPRISM and HyperSAS data, respectively. Based on the retrieval scheme of SeaPRISM [29, 30, 32], a hyperspectral-based procedure has been developed to derive the $nLw(\lambda)$ and $Rrs(\lambda)$ from the HyperSAS measurements. The coincident datasets of the $nLw(\lambda)$ and $Rrs(\lambda)$ derived from the measurements of the two collocated instruments are obtained for a period of more than one year (from October 2009 up to January 2011) encompassing the full natural variability of atmospheric and water conditions. Then, with the use of these datasets, the consistency and the efficiency of the above-water data processing have been assessed.

The detail analysis of these two collocated and coincident datasets not only allows us to obtain quality assured field data set but also permits us to make assessments of the intrinsic uncertainties, which are resulted from the perturbation of wavy sea surface and the estimations made in the above water data processing procedures, in the field data itself. In fact, quantification of the intrinsic uncertainties of the field data is the prerequisite if one needs to make assessments of uncertainties in the OC satellite data and identify sources of those uncertainties [36, 81]. In

this chapter, we will firstly present the data filtering and quality assurance procedures for the HyperSAS measurement. After that, uncertainties in the above water data will be identified by carrying out matchup comparisons between HyperSAS and SeaPRISM data at each step of measurement and processing procedure.

5.2 Data filtering procedure

Data filtering procedure for SeaPRISM system has already been developed in the framework of AERONET-OC distribution [29]. All the SeaPRISM data used in this study are cloud screened level 1.5 data. On the other hand, a specific HyperSAS data filtering has been developed independently of SeaPRISM and can be summarized as follows: first, the negative data are filtered and their values are replaced with zero, in the case that the measurement is very close to the dark value. Second, for each HyperSAS measurement sequence, the ratio of the down-welling irradiance E_d measured at 443 nm to its theoretical clear-sky value is computed. The theoretical irradiance is computed for the actual Sun elevation with 6SV radiative transfer code [82, 83] for an aerosol optical thickness of 0.1 at 550nm which is commonly the case in LISCO area. If the Sun is covered by cloud, the measured E_d consequently drops down and the irradiance ratio departs from one. On the basis of the distribution of the measured-to-computed E_d ratio (Figure 5.1.a) and following Antoine et al. [84], the whole measurement sequence is eliminated from the data quality process if the ratio is outside the [0.85,1.1] interval. Third, the relative standard deviation of sky radiances L_i is computed for each measurement sequence. If the sky is partially cloudy, for instance, this standard variation is enhanced by the cloud progression through the field of view during the 2 minute time acquisition. In order to filter the

HyperSAS dataset for clear sky conditions only, the relative standard deviation threshold of 4% has been set on the basis of the HyperSAS time series statistics (Figure 5.1.b).

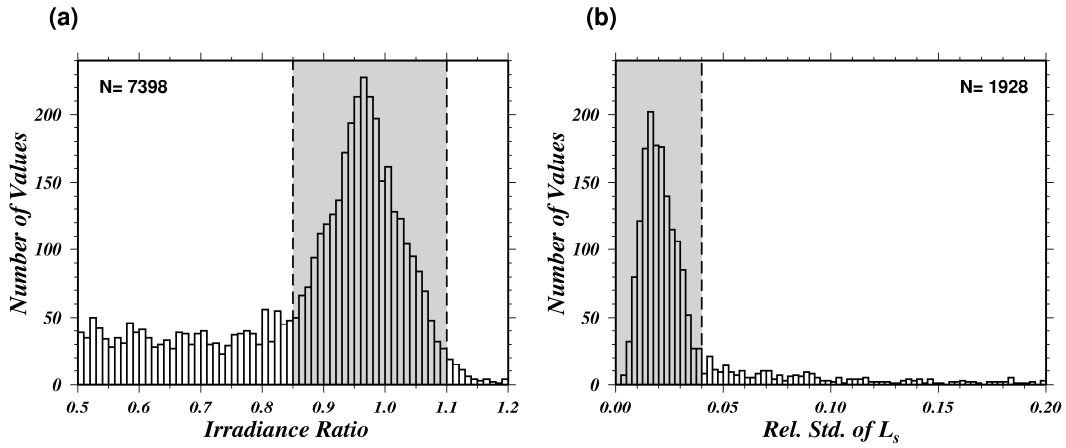

Figure 5-1. (a) Histogram of the ratio of the irradiance E_d measured at 443 nm by HyperSAS to its theoretical clear-sky value computed from 6SV radiative transfer code. The value of this ratio must be between 0.85 and 1.1 (shaded area) so that the corresponding data would be included in the data quality process. (b) Histogram of the relative standard deviation of sky radiances L_i having passed the E_d ratio filter. The values must be lower than 0.04 (shaded area) to pass the data quality process. N is the total number of corresponding data for the period from October 2009 up to January 2011.

5.3 HyperSAS Intrinsic Uncertainty Assessment

A major difficulty with above-water measurements is associated with the corrections to the observations for the effect of surface waves that introduce significant fluctuations into the glint and reflected skylight components. These fluctuations induce different geophysical noise in

respect to the Sun position and viewing geometry [78]. Because HyperSAS and SeaPRISM do not have the same viewing geometry along the day, it is of paramount importance to quantify the HyperSAS data quality independently of SeaPRISM. After this first quality assessment it will be possible to make use of HyperSAS and SeaPRISM time series in order to cross-validate both systems.

The data quality assessment of HyperSAS system along with its specific data processing is addressed here. First, all measurement sequences flagged in the HyperSAS data filtering steps, which were discussed in previous section, have been eliminated from the analysis in order to assure the required clear sky condition over the whole dataset. Second, for each measurement sequence the HyperSAS data processing has been applied to NT^* total sea radiance acquisitions separately, with NT^* equal to 20% of the NT sea-radiance measurements exhibiting the lowest radiance levels. It is reminded that NT varies from 44 to 210 within a measurement sequence of 3 minutes. In addition, it should be noted that this elimination of the highest sea-radiances corresponds to glint effect removal part of the above water data processing. Consequently, NT^* values of the normalized water-leaving radiance spectra, $nLw(\lambda)$, are retrieved for each HyperSAS measurement sequence. From those $nLw(\lambda)$, the estimator of the relative standard deviation is calculated as follows:

$$\sigma_{rel} = \frac{1}{nLw^{est}} \sqrt{\frac{1}{N_T^* - 1} \sum_{i=1}^{N_T^*} (nLw(i) - nLw^{est})^2} \tag{5.1}$$

where nLw^{est} is the normalized water leaving radiance estimated by the operational HyperSAS processing based on the mean value of the sea radiance computed over the NT^* individual measurements of each sequence. Thus, the value of σ_{rel} is an estimator of the uncertainties

induced by the geophysical noise (i.e. environmental effects) and propagated through the whole data processing. This value is used to quantify the geophysical uncertainty of HyperSAS system.

The parameter σ_{rel} has been computed for all the wavelengths in respect to the time of the measurement sequences for the different seasons of the year. The seasonal mean values of σ_{rel} are plotted in Figure 5.2(a - d). The effect of the sun and sky light on the sea surface is primarily driven by the sun position in the sky and the wind ruffled sea [85-88]. Because sun position and wind regimes change over the year, the HyperSAS uncertainties are analyzed for each season independently. It can be noted that the time axis of the plots of Figure 5.2 is given in UTC minus 4 hours as a local time indicator. In addition, a gray scale is used when σ_{rel} is lower than 5%, which is the target accuracy for water-leaving radiance in ocean color remote sensing [89], whereas a color scale is reciprocally used. In spring (Figure 5.2.a), the uncertainty estimator σ_{rel} at 550 nm is below 5% from early in the morning around 8:30am up to 2:30pm. After 3pm, the impact of the sun glint is enhanced owing to the relative position of the sun to the radiance sensor. Consequently, the glint removal part of the data processing become inefficient and σ_{rel} increases above 15% at 550nm.

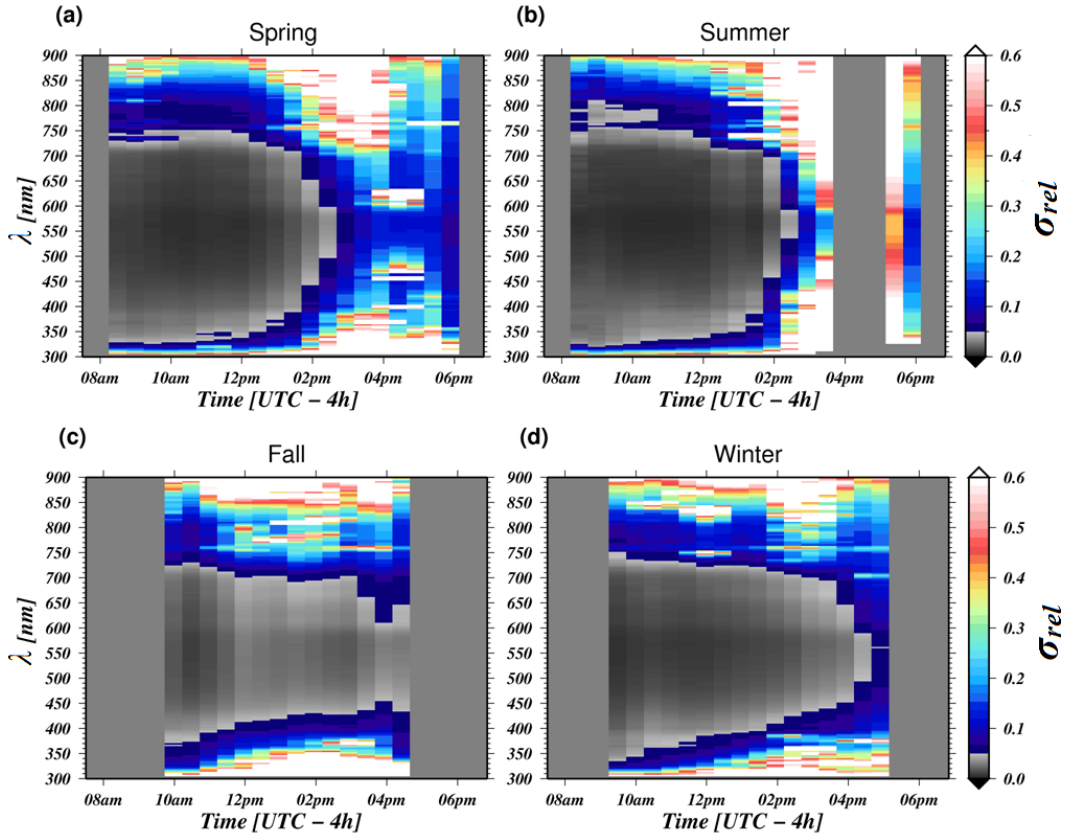

Figure 5-2. Relative standard deviation , σ_{rel}, of *nLw* retrieved by HyperSAS system. Color maps are plotted for (a) Spring, (b) Summer, (c) Fall and (d) Winter seasons. The color values are displayed in respect to the time of acquisition and all the HyperSAS spectral bands.

On the other hand, the relative uncertainties exhibit a spectral dependence. At 12pm, σ_{rel} is lower than 5% over the whole spectral range from 340 to 740nm. Outside from this range and particularly in the near infrared part of the spectrum the uncertainties increase up to 8% at 800nm and 30% at 860nm. In this specific part of the spectrum, L_w is significantly low or negligible in comparison to the sky and sun radiances. As a result, the correction of the sea radiance from the wave induced reflected light cannot be sufficiently accurate any longer. Based on the statistics

done over April to July 2010 (Figure 5.2.a), the HyperSAS data quality can be summarized as follows: (i) uncertainties are below 5% for the spectral range of 330 to 740 nm until local noon, (ii) between 12pm and 2pm acceptable uncertainties are retrieved for a smaller spectral range, (iii) after 2:30pm the contribution of the sun glint is strongly increased and no data stay sufficiently accurate.

Regarding to the summer period, the σ_{rel} values lead to quite similar conclusions. Nevertheless, it should be noted that the lack of data between 3:30pm and 5pm (Figure 5.2.b) is resulted from the application of the HyperSAS filtering step which employs sky radiance relative standard deviation threshold. In fact, the sky radiance sensor is pointing to the vicinity of the sun during this period. The measured sky radiance is subsequently highly variable over the 3 minutes of the sequence inducing a strong standard deviation similarly to the situation of cloud passing through the sensor field of view. During fall and winter (Figure 5.2.c and d), the time range of accurate data is substantially longer from around 9am to 4:30pm. However, the spectral range of the acceptable uncertainties are slightly reduced; especially in fall where this range is limited by 420 and 690 nm in average.

A more synoptic view of the HyperSAS uncertainties can be expressed by plotting the mean σ_{rel} in respect to the viewing and illumination geometrical configuration. This configuration is totally described by the Sun zenith angle, θ_s, and the relative azimuth angle, φ, while the HyperSAS viewing angle, θ_v, is fixed and set to 40° from the nadir direction. The results are displayed in Figure 5.3 for three center wavelengths (443, 550 and 670 nm) that are widely used in ocean color radiometry purposes. For these three bands, results show minimum uncertainties around φ = 130° which is consistent with previous theoretical studies [71]. The contamination by

environmental effects of the retrieved *nLw* becomes sensitive for φ < 60° whatever the Sun elevation with uncertainties higher than 5%. In consequence, it is concluded that quality assured HyperSAS data can be possible only for φ > 60° range. For that relative azimuth range, uncertainty levels stay lower than 5% thereby showing a large range of viewing configuration available for acquiring accurate water-leaving radiance from above water.

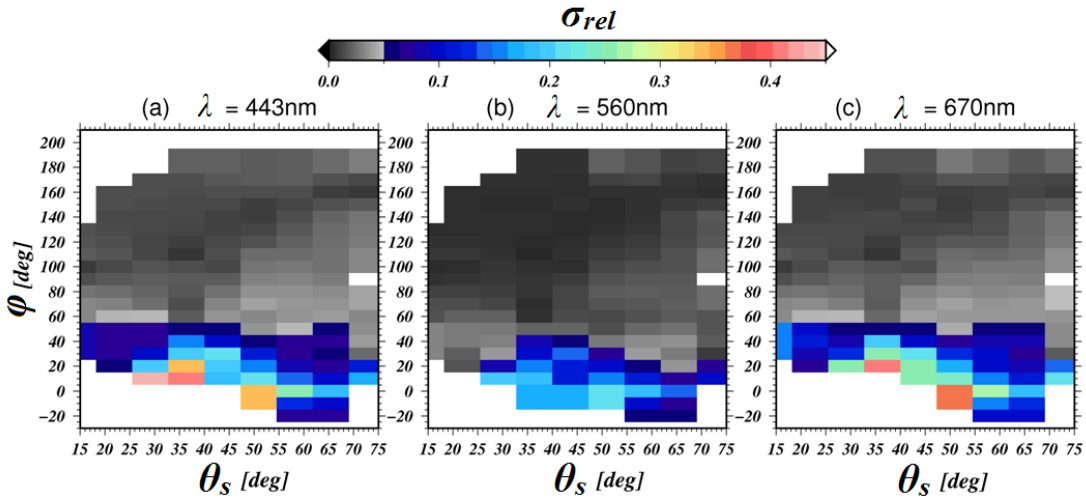

Figure 5-3. Relative standard deviation (uncertainty estimator) of *nLw* as retrieved by HyperSAS system in respect to the solar zenithal angle (θ_s) and the relative azimuth angle (φ) at (a) 443, (b) 560 and (c) 670 nm.

5.3.1 Comparisons between HyperSAS and SeaPRISM data

According to the data processing procedures described in chapter 4, the hyperspectral normalized water-leaving radiance spectra, *nLw*(λ), are retrieved from the HyperSAS measurements over a more than one year period. SeaPRISM and HyperSAS data are compared assuming that both systems on LISCO platform measure the same geophysical target, i.e. the same water composition, in the same time. As an example, *nLw*(λ) retrieved from SeaPRISM and

HYPERSAS measurements are displayed for November 4th 2009 in Figure 5.4. This comparison shows a satisfactory spectral agreement between the two datasets. In addition, it should be noted that the hyperspectral data exhibit supplementary information not contained in the multispectral one supplied by SeaPRISM [90].

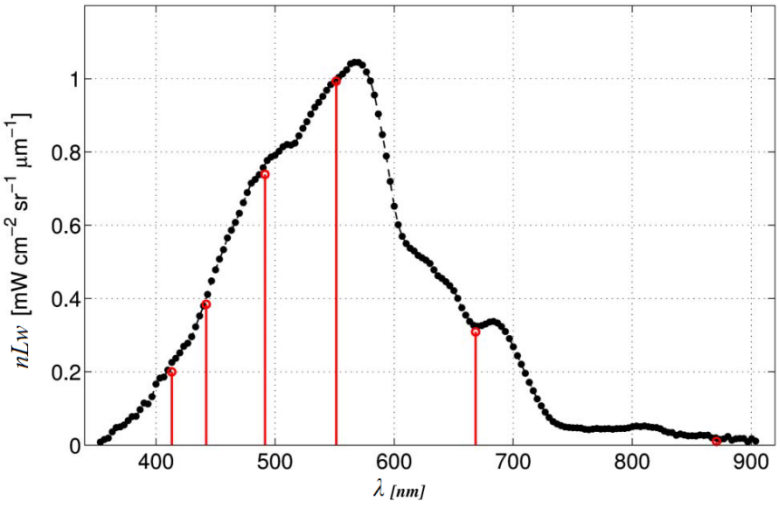

Figure 5-4. Examples of concomitant HYPERSAS (black dots) and SeaPRISM (red circles) data for November 4th 2010.

The time series matchups and comparisons between the normalized water leaving radiance obtained with SeaPRISM and HyperSAS instruments were also carried out at specific SeaPRISM center wavelengths (i.e. 412, 443, 491, 551and 668nm). For the comparison purpose, $L_T(\lambda)$, $L_i(\lambda)$ and $E_d(\lambda)$ measurements of HyperSAS instruments are convolved with the spectral response function of SeaPRISM instrument in order to produce the multispectral data that is comparable to those of SeaPRISM. Calculations are carried out as follows:

$$f(\upsilon) = \int_{\lambda} \zeta(\lambda - \upsilon) \cdot H(\lambda) \cdot d\lambda \tag{5.2}$$

Where $H(\lambda)$ represents the measurement made by HyperSAS instrument, $\zeta(\lambda)$ is the spectral response function of SeaPRISM instrument, and υ is the specific center wavelengths of SeaPRISM. The resulting $f(\upsilon)$ is the measurement quantity which is comparable to the measurements of SeaPRISM at its center wavelengths.

5.3.2 Time series analysis

The 1-year time series of $nLw(\lambda)$ data at two SeaPRISM spectral bands are plotted for the SeaPRISM and HyperSAS instruments in Figure 5.5. These values are derived from the quality-checked measurements taken between 9:00 and 16:00 of local time. In addition, all the HyperSAS measurements with a relative azimuth smaller than 70° have been eliminated based on the uncertainty analysis described in the previous section to avoid the glint contamination. For each day, the mean value and the standard variation are calculated for SeaPRISM and HyperSAS respectively.

In the figure, time series analysis exhibits strong seasonal variations for both datasets. In addition, agreement between two datasets in terms of temporal variability can be also clearly observed. For instance, a specific pattern of high water-leaving radiances is observable on March 17th 2010 resulting from an increase of sediment concentration following a significant storm event due to higher riverine input and water body mixing. As a result, it can be concluded that the seasonal changes are well captured by both above-water measurement systems. This temporal agreement combined with the spectral shape agreement of the LISCO data motivates us to further analyze the inherent uncertainties in the above water measurements and data processing procedures by performing the quantitative matchup comparisons between the two datasets.

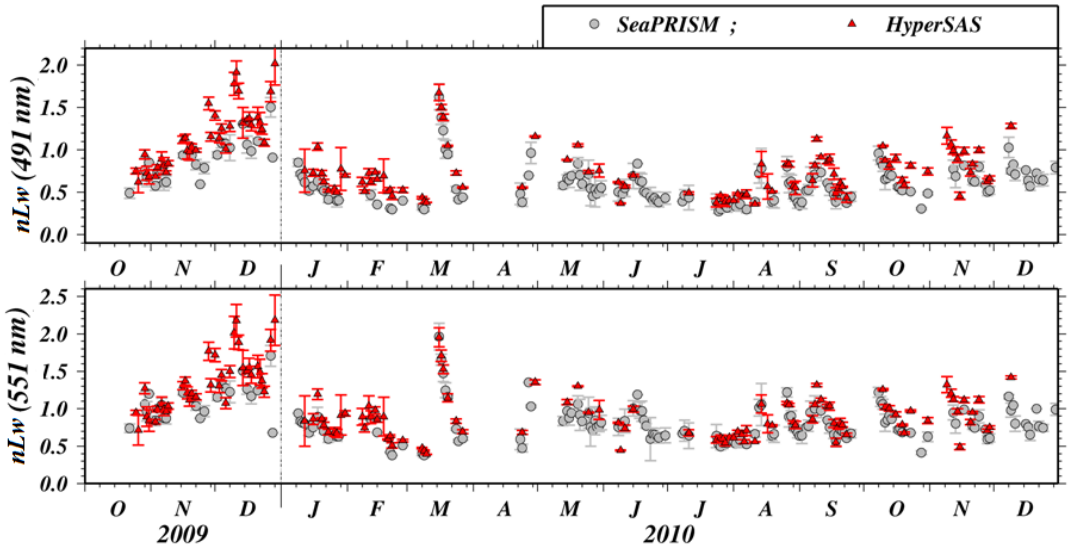

Figure 5-5. Time series of the normalized water-leaving radiance retrieved with HyperSAS (red triangles) and SeaPRISM (grey circles) for two SeaPRISM bands centered on 491 and 551 nm. The vertical bars correspond to the daily standard deviation.

5.3.3 Assessments of uncertainties in above water measurements

To further quantify the uncertainty in the *nLw* data obtained with the above-water instrumentation, matchup inter-comparisons were performed for the whole set of data measured or retrieved by SeaPRISM and HyperSAS systems. The data involved in the following analysis were restricted so that SeaPRISM and HyperSAS measurement sequences are taken within ±10 minutes time window. This time window restriction is applied to minimize the temporal variability between the two observations resulted from the natural changes in environmental and water conditions. In the comparisons, we carried out the statistical analysis of the discrepancies between the measurements or retrieved data of the two systems at each step of above water data

processing procedures. In the statistical approach adopted here, neither SeaPRISM nor HyperSAS data are assigned as reference since both systems are in above-water configurations. Instead, the inter-comparisons were assessed in terms of the percent differences relative to the average of the two data being compared. Two statistical parameters, namely absolute relative percent difference (ARPD) and unbiased relative percent difference (URPD), are used as the uncertainty quantifiers of the comparisons.

The absolute relative percent difference (ARPD) is defined as:

$$ARPD = \frac{200}{N}\sum_{i=1}^{N}\frac{|y_i - x_i|}{x_i + y} \tag{5.3}$$

and the unbiased relative percent different (URPD) is defined as:

$$URPD = \frac{200}{N}\sum_{i=1}^{N}\frac{y_i - x_i}{x_i + y_i} \tag{5.4}$$

where SeaPRISM data are taken as x and HyperSAS data are taken as y.

In the comparisons, the statistical indicator ARPD provides the information regarding the dispersion while URPD can be used to assess the expected bias between the compared datasets. Other statistical indicators such as coefficient of determination, R^2, and regression slopes for each comparison are also obtained in addition to the parameters described above.

5.3.3.1 Comparison of sky radiance measurements

Figure 5.6 (a) shows the comparison between the average direct sky radiance measurements of SeaPRISM, denoted as $L_{i(\mathrm{Spr})}$, and those of HyperSAS, denoted as $L_{i(\mathrm{HS})}$, for the relative azimuth angles for HyperSAS observations restricted in the $70^{o} \leq \phi \leq 180^{o}$ range. The comparison

exhibits strong correlations between HyperSAS and SeaPRISM data with a spectral average coefficient of determination (R^2) greater than 0.91. It can be observed that the dispersion between the two data is high exhibiting ARPD and URPD values 14.9% and -8.9% respectively. In addition, slope of the regression line between the two data deviates significantly from the 1:1 line.

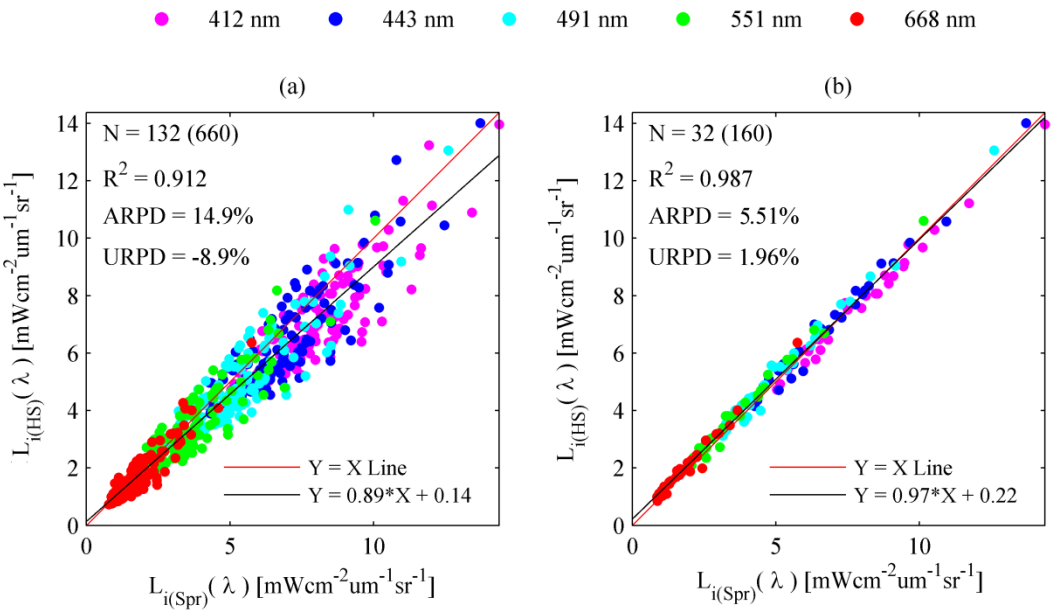

Figure 5-6. Comparisons between HyperSAS and SeaPRISM average sky radiance, L_i ($mWcm^{-2}\ sr^{-1}\ \mu m^{-1}$): (a) relative azimuth angles for HyperSAS observations are restricted in the $70^o \leq \varphi \leq 180^o$ range; (b) relative azimuth angles are restricted to $80^o \leq \varphi \leq 100^o$ range. N is the total number of the comparisons, the bracketed value is the number of different measurement sequences used in the comparison.

Nevertheless, it should be reminded that the dispersion between the two data is almost entirely resulted from the variations in the intensity distribution of the sky radiance field [91] rather than from the measurement uncertainties between two instruments. In fact, all $L_{i(\mathrm{Spr})}$ measurements are taken pointing toward the direction perpendicular to the solar plane because of the configuration of SeaPRISM instrument in which its φ is always set to 90°. Conversely, due to the fixed configuration of HyperSAS instrument, $L_{i(\mathrm{HS})}$ measurements are taken with varying φ values throughout the day resulting in values relatively lower than $L_{i(\mathrm{Spr})}$ for $\varphi > 90^{o}$ range and higher than $L_{i(\mathrm{Spr})}$ for $\varphi < 90^{o}$. The consistency between two measurement systems can be readily observed in the Figure 5.6 (b) in which pointing directions of HyperSAS and SeaPRISM are within $\pm 10^{o}$. It was found that R^2 of L_i comparison increases up to 0.987. URPD and ARPD are reduced down to 1.96% and 5.51% respectively and the regression line between two data becomes very close to the 1:1 line. Thus, statistical differences between the two comparisons clearly identify the directional variations in the sky radiance distribution.

Table 5.1 shows the statistical summary of the comparisons between the $L_{i(\mathrm{Spr})}$ and $L_{i(\mathrm{HS})}$ measurements. The statistical summary for L_i comparison with restricted azimuth range confirms the spectral consistencies between the two measurement systems exhibiting very strong correlation at every wavelength with R^2 values in the 0.949 to 0.985 range. URPD values are in the range of -2.01% in 412nm to 4.04% in 668nm.

Table 5-1. Statistical summary of the comparisons of $L_{i(Spr)}$ and $L_{i(HS)}$ measurements. (1st row) HyperSAS observations are restricted in the $80^o \leq \varphi \leq 100^o$ range. (2nd row) HyperSAS observations restricted in the $70^o \leq \varphi \leq 180^o$ range.

	Wavelength (nm)					*Spectral Average*
	412	***443***	***491***	***551***	***668***	
R^2	0.98	0.98	0.98	0.98	0.95	0.987
***URPD* (%)**	-2.01	1.54	3.03	3.22	4.04	1.964
***ARPD* (%)**	3.97	4.55	5.61	6.62	6.8	5.510
R^2	0.767	0.775	0.789	0.81	0.835	0.912
***URPD* (%)**	-12.4	-8.97	-8.22	-8.3	-6.6	-8.9
***ARPD* (%)**	14.1	13.1	14.2	15.8	17.4	14.9

5.3.3.2 Comparison of the down-welling irradiance

Comparison between the down-welling irradiance, $E_{d,}$ data of SeaPRISM and HyperSAS is shown in the figure 5.7. It should be recalled here that, unlike HyperSAS, SeaPRISM instrument does not have the capability of making down-welling irradiance measurements directly. As the result, $E_{d(Spr)}$, has to be calculated from the diffuse atmospheric transmittance, t_d, using equation (4.8). On the other hand, t_d is derived from the Rayleigh (τ_R), aerosol (τ_A), and ozone (τ_O) optical thicknesses (see equation (4.6)) which are standard AERONET data products. It is also worth noting here that the down-welling irradiance measurements of HyperSAS system have been corrected for the effects of non-ideal cosine response [92] of the irradiance sensor. The estimation of the impact of the non-cosine response effect over the measured down-welling irradiance requires the characterization of the angular response of the HyperSAS irradiance

sensor and the additional calibration of it was conducted at Satlantic, Inc to quantify the deviations of the sensor characteristics from original specifications for the full range of wavelength and incidence angles. Based on this specification of the sensor, the resulting error on the down-welling irradiance was simulated by radiative transfer computations performed with Hydrolight 5 assuming clear sky condition (which realistically is prerequisite for the satellite data validation) and τ_A at 550nm wavelength equal to 0.2. Then, with the use of those simulation results and following [92], wavelength and solar zenith angle dependent correction factors were produced and the down-welling irradiance measurements of HyperSAS are adjusted accordingly. The resulting comparison exhibits strong correlation between two data with the spectral average R^2 value equal to 0.99. In addition, regression line between the two data is close to 1:1 line.

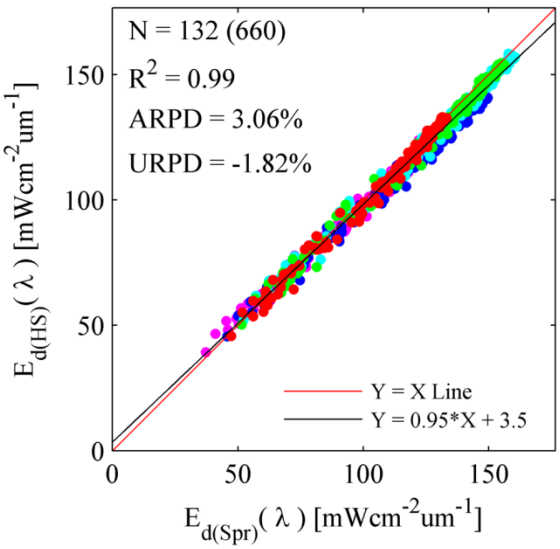

Figure 5-7. Comparison of the down-welling irradiance (in mW cm^{-2} μm^{-1}) derived from SeaPRISM and HyperSAS measurements

Spectral consistency between the two data can be also clearly observed from the strong correlations between the two data at every wavelength (see Table 5.2). The comparison also shows the existence of systematic negative bias between the two data depicting -1.82% in spectral average URPD value. Nevertheless, given the fact that the two systems acquire the E_d data in completely different methods, the observed discrepancy between the two data is not substantial. The observed negative bias can be at least partially explained by the possible presence of the absorbing aerosols, which are not taken into account by the current SeaPRISM atmospheric transmittance retrieval model, in the area of the LISCO platform [93]. If the absorbing aerosols are present, their absorption behavior can be quite pronounced, and as the result, SeaPRISM model output can be inadequate. In addition, SeaPRISM parameterization of the atmospheric transmittance is limited to a two- dimensional ideal atmosphere, which cannot encompass the full range of environmental variability in the atmospheric attenuation (e.g., surrounding clouds, water vapor spatial distribution). Conversely, it should be also reminded that HyperSAS E_d measurements can be as well affected by the stray light perturbations which might be quite pronounced for hyperspectral radiometers in the blue spectral region [94]. Although both the SeaPRISM parameterization and possible stray light effect on the retrievals of the E_d data should be further investigated, this atmospheric related study is beyond the scope of this research.

Table 5-2. Statistical summary of the comparisons of $E_{d(Spr)}$ and $E_{d(HS)}$

	Wavelength (nm)					*Spectral Average*
	412	***443***	***491***	***551***	***668***	
R^2	0.992	0.992	0.993	0.993	0.992	0.99
***URPD* (%)**	-2.14	-4.36	-1.32	-1.01	-0.35	-1.82
***ARPD* (%)**	2.42	5.42	2.55	2.21	1.82	3.06

5.3.3.3 Comparison of total sea radiance measurements

Similarly, comparison of the total sea radiance measurements of HyperSAS, denoted as $L^*_{T(HS)}$, and SeaPRISM, denoted as $L^*_{T(Spr)}$ for $80^o \leq \phi \leq 100^o$ range is shown in Figure 5.8. For this range, both instruments are pointing toward approximately the same direction (i.e. within $\pm 10^o$ from each other), as the result, geophysical targets are also approximately the same. In this comparison, L^*_T values of both systems are calculated by averaging the lowest total sea radiance measurements. The correlation between HyperSAS and SeaPRISM data for this comparison is very strong with a coefficient of determination greater than 0.989. Nevertheless, spectral average URPD between two data is 7.81% clearly showing the bias between the measurements of two systems (see Table 5.3 for detail statistical summary).

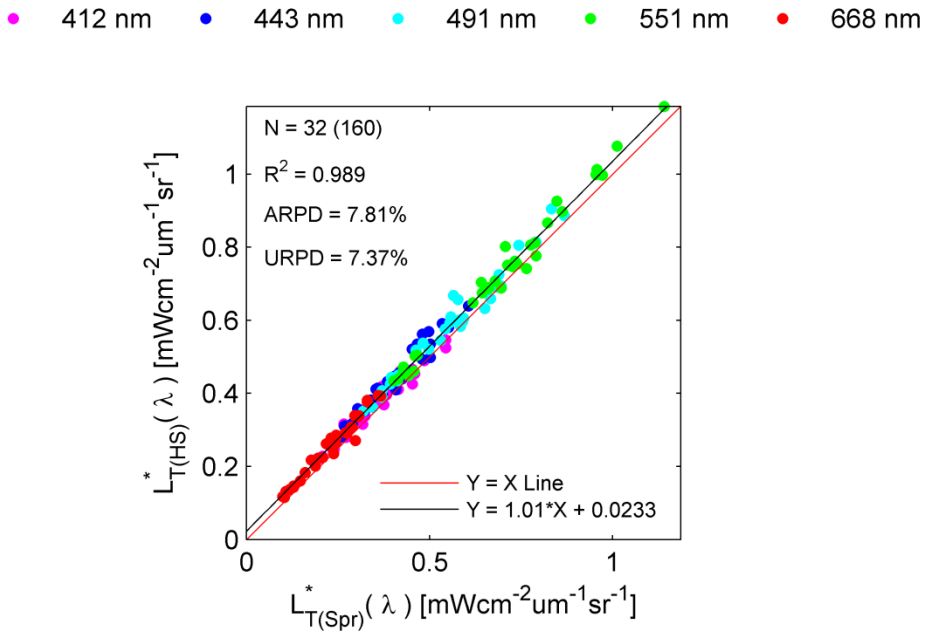

Figure 5-8. Inter-comparisons of HyperSAS and SeaPRISM sea radiance L^*_T (in $mWcm^{-2}\ sr^{-1}\ \mu m^{-1}$). for $80^o \leq \varphi \leq 100^o$ range.

The observed discrepancy is at least partially arisen from the differences between the two systems, namely integration time and field of view. Integration time of SeaPRISM instrument is 0.075 seconds where as that of HyperSAS is about 2 seconds. Field of view is also higher for HyperSAS, with 3°, compared to SeaPRISM with 1.2°. The different responses of the HyperSAS and SeaPRISM to the same filtering procedure (namely excess sky glint perturbation removal procedure) may have caused at least some of the observed discrepancies. It has been observed in our previous study [33] that the excess sky glint removal procedure, in which only the lowest 20% of multiple successive total sea radiance measurements are utilized for further processing, eliminates mostly the remainder of sun glint component which was not eliminated by other filtering procedures established in [33] and also discussed in section 5.2 and 5.3 for HyperSAS.

Then again, this approach, clearly empirical, was shown to be quite effective for SeaPRISM instrument in the previous studies [29, 30]. However, it was also clearly stated in those same studies that the scheme can certainly produce an overcorrection of sky glint perturbations, and as the result, underestimation in the total sea radiance measurements. It should also be pointed out that Hyper SAS system's longer integration time may probably reduce the ability to filter out the rapidly changing sky glint perturbation effects and therefore existence of the offset background spectrum in the HyperSAS total sea radiance measurements is possible. A dedicated study should be granted to further investigate the performance of the HyperSAS system as well the possibilities of overcorrections in the sky-glint perturbation procedure applied to SeaPRISM.

Table 5-3. Statistical summary of the comparisons of $L^*_{T\,(\mathrm{Spr})}$ and $L^*_{T(\mathrm{HS})}$ measurements. HyperSAS observations are restricted in the $80^o \leq \varphi \leq 100^o$ range.

	Wavelength (nm)					*Spectral Average*
	412	***443***	***491***	***551***	***668***	
R^2	0.942	0.952	0.963	0.983	0.962	0.989
***URPD* (%)**	7.27	9.82	5.28	3.86	9.12	7.37
***ARPD* (%)**	7.77	9.94	5.31	3.96	9.22	7.81

We further carried out the comparison using the quality-assured Level 1.5 average total sea radiance data for SeaPRISM in lieu of the lowest ones. Figure 5.9 (a & b) depicts the comparisons between the average total sea radiance of SeaPRISM, denoted as $L_{T(Spr)}$, and $L^*_{T(\mathrm{HS})}$. Here, $L^*_{T(\mathrm{HS})}$ and $L_{T(Spr)}$ data can be considered free of sun-glint perturbation effects as the sun-glint infected measurements have been effectively filtered out by taking the lowest values in the

case of HyperSAS, and by using a measurement geometry and by accounting for field constraints in the case of SeaPRISM.

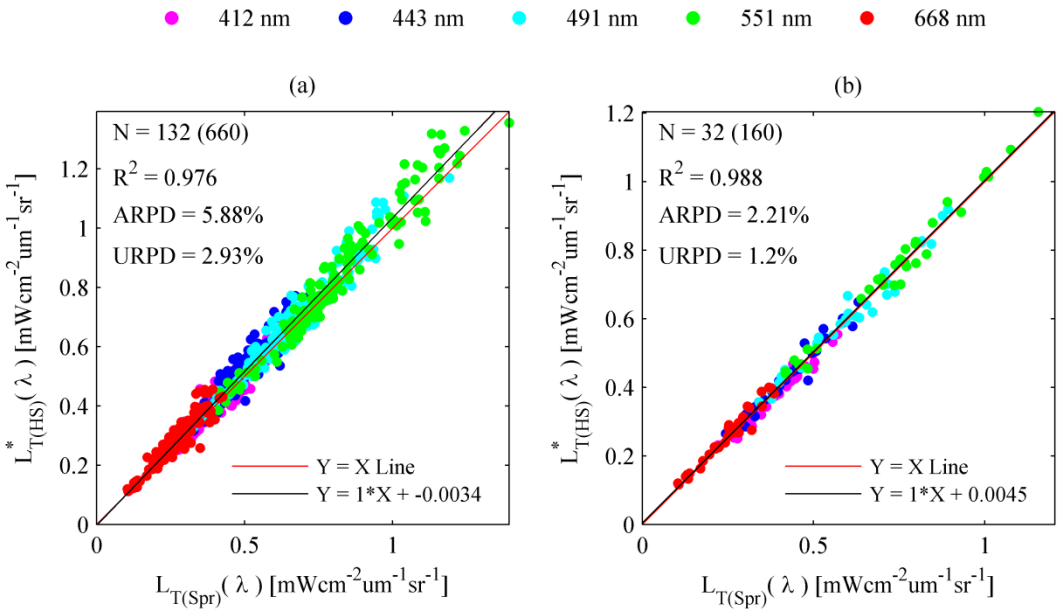

Figure 5-9. Inter-comparisons of HyperSAS and SeaPRISM sea radiance L^*_T (in $mWcm^{-2}\ sr^{-1}\ \mu m^{-1}$). (a) relative azimuth angles for HyperSAS observations are restricted in the $70^o \leq \varphi \leq 180^o$ range; (b) relative azimuth angles are restricted to $80^o \leq \varphi \leq 100^o$ range.

It can be seen in the Figure 5.9 and Table 5.4 that significant statistical improvements are made by taking this step. Discrepancies between the two data are reduced by 6% showing reduction in both ARPD and URPD values throughout the spectrum. Regression line for the comparison with the restricted azimuth range, which permits minimization of the impact of both the bidirectionality dependence and the differences in the surface-reflected radiance contributions to

the water-leaving radiance derivations, is also very close to 1:1. In addition, the discrepancy between the two datasets is becoming almost insignificant with its URPD value close to 1%.

Table 5-4. Statistical summary of the comparisons of $L_{T\,(Spr)}$ and $L^{*}_{T(HS)}$ measurements. (1st row) HyperSAS observations are restricted in the $80^{o} \leq \varphi \leq 100^{o}$ range. (2nd row) HyperSAS observations restricted in the $70^{o} \leq \varphi \leq 180^{o}$ range.

	Wavelength (nm)					*Spectral Average*
	412	***443***	***491***	***551***	***668***	
R^2	0.976	0.949	0.971	0.978	0.962	0.988
***URPD* (%)**	-2.83	1.62	0.892	1.64	4.66	1.2
***ARPD* (%)**	2.195	1.995	1.79	1.86	3.185	2.21
R^2	0.894	0.909	0.948	0.955	0.889	0.976
***URPD* (%)**	0.275	4.32	2.51	2.24	5.3	2.93
***ARPD* (%)**	5.72	6.04	4.77	4.96	7.89	5.88

Therefore, for the SeaPRISM instrument, this very first step of the data acquisition has been revised and sea radiance data used from this point forward are the average of the total sea radiance measurements. With the considerations mentioned above, it is concluded that (i) the appropriateness of the excess sky glint removal approach which only utilizes lowest measurements should be further investigated as under- estimation in total sea radiance data can be occurred with the use of this approach; (ii) we also recognize the possibility of both SeaPRISM and HyperSAS data equally being affected by the potential residual excess sky glint with the use of the average of the total sea radiance measurements for SeaPRISM instrument and therefore shall explore the impacts of this possible residual component on the bi-directional

correction procedure in detail. Thus, extensive analysis with the use of the readiative transfer simulations and synthetically generated noise signals have been carried out in order to further investigate the implications resulting from the possible residual Sun and sky glint perturbations on the correction and retrieval procedures and the discussions will be presented in chapter 8.

5.3.4 Assessments of uncertainties in above water data processing

Using the direct measurements of HyperSAS or SeaPRISM, several data processing steps are applied to obtain the exact normalized water-leaving radiance as described in chapter 4. The uncertainties generated by each of these steps are analyzed here by means of comparisons over the whole LISCO data acquisition period.

5.3.4.1 Sky radiance reflection removal

The first step of the data processing corresponds to the removal of the sky radiance reflection from the total sea radiance measurement to obtain the water-leaving radiance L_w. The L_w values derived from HyperSAS and SeaPRISM are compared in Figure 5.10. The comparison show datasets are well correlated with the spectral average R^2 value higher than 0.97. It is observed that significant positive bias is introduced for the comparison with the unrestricted relative azimuth range (see Figure 5.10.a) exhibiting URPD values more than 9% which is almost 6.2% higher than the one observed in total sea radiance comparisons. Thus it can be concluded that the first step of data processing procedure induce the additional 6.2% in dispersion compared to the uncorrected total sea radiance data. This drastic increase in the dispersion is mainly driven by the sky glint removal step in the shorter wavelengths where L_T are usually low and L_i measurements are high relative to the values at the longer wavelength, and as the result degradation in the

consistency between the HyperSAS and SeaPRISM is increased at the shorter wavelengths (see Table 5.5).

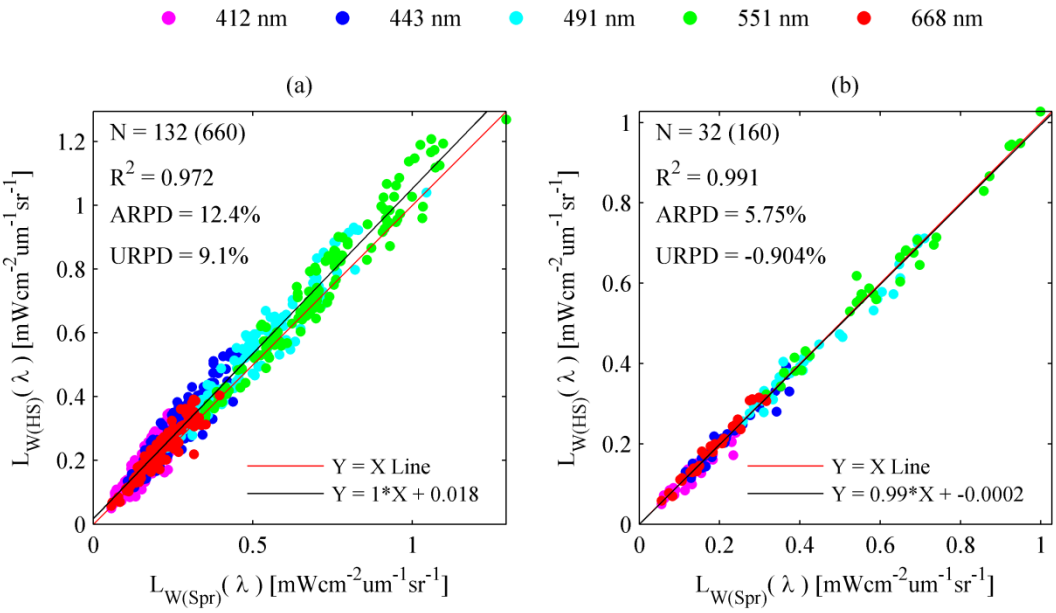

Figure 5-10. Inter-comparisons of HyperSAS and SeaPRISM water-leaving radiance L_w (in $mWcm^{-2}\ sr^{-1}\ \mu m^{-1}$). (a) relative azimuth angles for HyperSAS observations are restricted in the $70^o \leq \varphi \leq 180^o$ range; (b) relative azimuth angles are restricted to $80^o \leq \varphi \leq 100^o$ range.

In addition, overall observed bias throughout the spectrum can be at least partially explained by directional variations in the bidirectional structure of the water leaving radiance field. It has been observed through the radiative transfer simulations which will be detailed in chapter 7 that the water leaving radiances measured at the SeaPRISM geometry (i.e. relative azimuth angle $\varphi = 90^o$) are usually lower than those measured at other relative azimuth angles for solar zenith

angles θ_s greater than 30^o which are the cases for more than 80% of the data shown in the figure. Nevertheless, for the case of restricted relative azimuth range in which directional variations are minimal (see Figure 5.10.b), URPD value remains very small (about -1%) and regression line between two data is very close to 1:1 line with the correlation coefficient greater than 0.99 exhibiting the excellent agreement between the two retrievals.

Table 5-5. Statistical summary of the comparisons of $L_{W(\mathrm{Spr})}$ and $L_{W(\mathrm{HS})}$ retrievals. (1st row) HyperSAS observations are restricted in the $80^o \leq \varphi \leq 100^o$ range. (2nd row) HyperSAS observations restricted in the $70^o \leq \varphi \leq 180^o$ range.

	Wavelength (nm)					*Spectral Average*
	412	***443***	***491***	***551***	***668***	
R^2	0.915	0.946	0.978	0.982	0.974	0.991
***URPD* (%)**	-6.08	-0.275	-1.17	0.505	2.5	-0.904
***ARPD* (%)**	10	6.02	3.75	3.39	5.58	5.75
R^2	0.803	0.864	0.941	0.955	0.887	0.972
***URPD* (%)**	14.5	13.4	5.78	3.82	8.04	9.1
***ARPD* (%)**	21.1	16.3	7.93	5.82	10.9	12.4

5.3.4.2 Normalization for angular dependency and environmental effects

Normalization of the water leaving radiance is carried out in two steps. An intermediate product, denoted as L_{wN} is calculated in the first step. L_{wN} is the water-leaving radiance normalized by the cosine of the solar zenith angle and the diffuse atmospheric transmittance, $t_d \cdot \cos\theta_s$, as described in chapter 4 in order to remove the environmental effects on the water-leaving radiance. In the

second step, adjustments for viewing and illumination angle dependence or for the effects of the non-isotropic distribution of the in-water light field are made in order to obtain the final normalized water leaving radiance *nLw*.

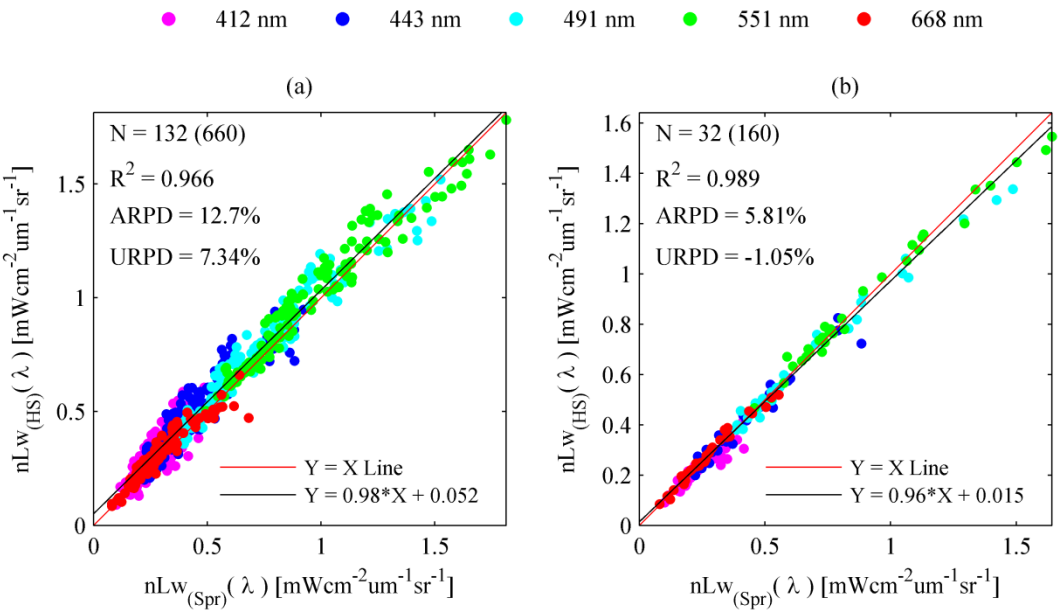

Figure 5-11. Inter-comparisons of HyperSAS and SeaPRISM normalized water-leaving radiance *nLw* (in $mWcm^{-2}\ sr^{-1}\ \mu m^{-1}$). (a) relative azimuth angles for HyperSAS observations are restricted in the $70^o \leq \varphi \leq 180^o$ range; (b) relative azimuth angles are restricted to $80^o \leq \varphi \leq 100^o$ range.

As it has been shown in section 5.3.3.2 the uncertainty budget originates from the differences in derivation of down-welling irradiance (as the result diffuse atmospheric transmittance, t_d,) data between the SeaPRISM and HyperSAS is about 1.8%. Although small, this needs to be improved in order to reconcile the two measured datasets. In order to minimize the impact of this step, the

HyperSAS data has been processed using the respective SeaPRISM atmospheric transmittance values in the normalization of the water-leaving radiance. Figure 5.11 (a & b) shows the comparisons of the final exact normalized water leaving radiance, $nLw(\lambda)$.

Table 5-6. Statistical summary of the comparisons of $nLw_{(Spr)}$ and $nLw_{(HS)}$ retrievals. (1st row) HyperSAS observations are restricted in the $80^o \leq \varphi \leq 100^o$ range. (2nd row) HyperSAS observations restricted in the $70^o \leq \varphi \leq 180^o$ range.

	Wavelength (nm)					*Spectral Average*
	412	***443***	***491***	***551***	***668***	
R^2	0.902	0.958	0.987	0.988	0.978	0.989
***URPD* (%)**	-6.21	-0.404	-1.3	0.342	2.34	-1.05
***ARPD* (%)**	10.1	6.04	3.93	3.39	5.58	5.81
R^2	0.729	0.862	0.947	0.951	0.894	0.966
***URPD* (%)**	12.7	11.6	4.01	2.06	6.33	7.34
***ARPD* (%)**	21.4	16.6	8.26	5.92	11.1	12.7

As the same t_d data has been used in the normalization for the atmospheric effect, statistical differences arisen in this step are the results of the bi-directional correction procedure which removes the angular dependency of the water leaving radiance. It can be observed in Figure 5.11.a that the $nLw(\lambda)$ comparison for the $70^o \leq \phi \leq 180^o$ relative azimuth angle range shows slight degradation in the consistency between the two datasets resulting in relatively weaker R^2 values of 0.966 and higher ARPD values for all wavelengths compared to the similar comparison performed between the two data before the normalization step (see Figure 5.10 and Table 5.5). Nevertheless, decreases in URPD values are also observed throughout the spectrum resulting

1.8% spectral average reduction. This result signifies the importance of the bi-directional correction and further detail analysis of it will be made in the later chapters.

5.4 Summary of the Chapter

We have developed a specific hyper spectral data filtering procedure for HyperSAS instrument based on the framework of AERONET-OC data processing to achieve the quality assured hyper-spectral time series data to be used in the assessments of uncertainties in the above water and satellite OC data. This data filtering procedure which makes use of the sky radiance and down-welling irradiance measurements effectively eliminate the measurements corrupted by the severe weather conditions or cloud. With the use of this quality assured hyper-spectral dataset, we further investigate the uncertainties in the above water data associated with the randomly fluctuating wave perturbation effects. As relative azimuth angle, φ, of HyperSAS measurements changes as the day progress, uncertainties in the water leaving radiance field can be analyzed as the function of viewing geometry. Thus, this analysis permits us to define the azimuth range in which above water data can be acquired with the acceptable level of uncertainty. It has been shown that environmental effects of the retrieved *nLw* becomes sensitive for $\varphi < 60°$ whatever the Sun elevation with uncertainties higher than 5%. In consequence, it is concluded that quality assurance HyperSAS data can be possible only for $\varphi > 60°$ range. HyperSAS data accuracy has been also shown on the basis of statistics of daily measurements gathered over more than one year (i.e. October 2009 until January 2011), exhibiting uncertainties below 5% within consistent spectral and time ranges which are suitable for ocean color radiometry satellite validation activities.

Furthermore, with the use of quality assured HyerSAS and SeaPRISM data, we carried out the time series analysis of the above water data obtained at the LISCO site. The 1-year time series of $nLw(\lambda)$ data obtained with the collocated instruments exhibits that the seasonal changes are well captured by both above-water measurement systems.

To further quantify the uncertainty of the *nLw* obtained by above-water instrumentation, matchup comparisons were performed for the whole set of data measured or retrieved by SeaPRISM and HyperSAS systems. The comparisons performed for the sky radiance, L_i, and total sea radiance, L_T, exhibit strong correlations between HyperSAS and SeaPRISM data with a coefficient of determination greater than 0.987 for both comparisons. Uncertainties of the two measurements are very low with the URPD values less than 2% for L_i and 1.2% for L_T . We also made assessments to the uncertainty induced in the above water data processing procedures by performing comparisons between HyperSAS and SeaPRISM data at each data processing step. It is also observed that the bidirectional correction which is optimized for case 1water actually reduces about 1.8% of uncertainty between two data exhibiting potential for further improvements in above water data processing if bidirectional correction developed for the case 2 condition were used.

6 Representativeness of LISCO as the Ocean Color Data Validation Site

6.1 Ocean color validation site

An ideal site for the validation activity of satellite-derived parameters would provide ground truth data within a range and statistical distribution closely matching those of the satellite data [28, 29, 89]. In coastal areas, the oceanic and atmospheric parameters might be very variable from site to site and highly affect the measurements from space [95]. In addition, specificity of each site has to be preliminarily investigated in order to assess its representativeness and suitability for satellite validation activities or vicarious calibration effort [89]. Such investigations are detailed in this chapter for the LISCO site based on the standard OBPG distribution of MERIS, MODIS and SeaWIFS as well as the SeaPRISM data of the AERONET-OC distribution over a two year period. To investigate the representativeness of LISCO as a validation site, detail analyses were carried out particularly for (i) adjacency effect with the use of the top-of-atmosphere (TOA) radiance of the OC sensor images, (ii) effectiveness of atmospheric correction process by comparing the in-situ and satellite retrieved aerosol optical thickness, and (iii) time series matchup and comparisons between satellite and in-situ $nLw(\lambda)$ to verify the statistical and seasonal consistencies between the two datasets.

6.2 Adjacency effect

In coastal areas, the top-of-atmosphere (TOA) radiance measured by satellite over sea can be affected by a fraction of light reflected from the mainland. Reflected light originated from the land may reduce the image contrast when the atmospheric turbidity increases [96, 97], and the phenomenon is routinely called adjacency effect. This adjacency effect is produced by a

difference in the reflectance of adjacent surfaces, and the magnitude of the related perturbations in satellite data and they are typically a function of the spectral reflectance of surfaces and of the optical properties of the atmosphere (i.e., the aerosol type and load). Therefore, a basic requirement for operating calibration/validation site is to be located in a marine (or lake) region at a distance from the mainland that minimizes the adjacency effects in satellite observations [29]. In order to determine whether the LISCO site meets the objectives of validating coastal ocean color products, the distributions of the top-of-atmosphere radiances of the Level 1 MERIS satellite data has been analyzed to quantify the importance of the adjacency effect over the LISCO area.

The high resolution Level 1 MERIS data provide TOA reflectances with a spatial resolution of 260 m by 300 m. Those images have been screened over a 2-year period from January 2008 to the end of 2010. 28 perfectly cloud-free images have been selected over the LISCO site and its surrounding shores. These selected images correspond to wide range of atmospheric conditions from very clear atmosphere to moderately turbid atmosphere with the aerosol optical thicknesses values ranging from 0.003 to 0.15 at 870 nm, as measured by the LISCO SeaPRISM system, thereby encompassing realistic variability of the aerosol loading and type. The TOA reflectances at 865 nm have been extracted from image transects over the whole set of the Level 1 MERIS data. The image transects correspond to the north-south line passing through Long Island Sound by the LISCO platform. The TOA reflectances are plotted, in Figure 6.1, in respect to the distance from the LISCO platform.

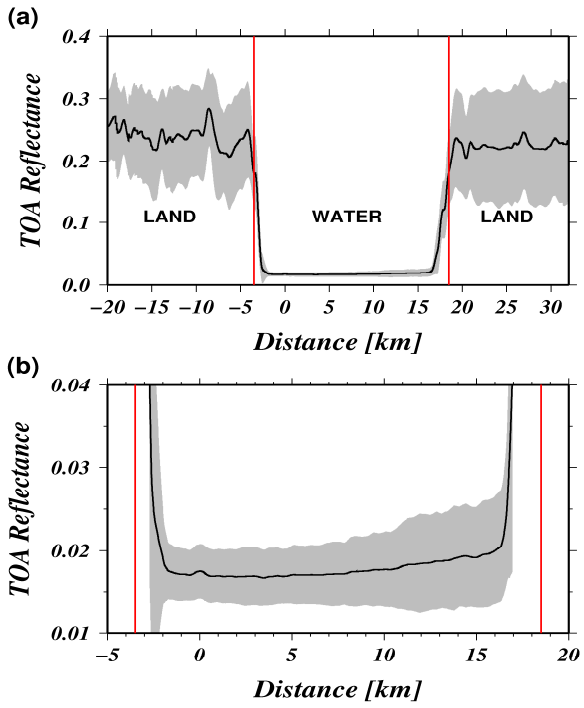

Figure 6-1. (a) Top-of-atmosphere (TOA) reflectance at 865 nm from 28 cloud free L1 MERIS images in respect to the distance from LISCO site. The black line is the mean value of TOA reflectance for a South-North transect passing over Long Island Sound (WATER) and the surroundings coasts (LAND); the gray envelope stands for plus or minus the corresponding standard deviation. The coast boundaries are denoted by vertical red lines. (b) Magnification of the water part of the transect.

The mean value of the TOA reflectance is comprised between 0.2 and 0.3 over the lands, and drops down to 0.02 over the LISCO surrounding waters (Figure 6.1.a). Interestingly, the TOA reflectances are observed to be dramatically decreasing when passing the shore. Nevertheless, this collapse stops two kilometers before the platform location (see Figure 6.1.b). Based on the delimitation of the TOA reflectance at 865 nm near the shore, it can be concluded that the adjacency effect is significant up to 1.5 km from the coast, that is, 2 km before the platform

location, and becomes negligible in the direct vicinity of the platform and further offshore. From this analysis we concluded that the LISCO site is suitable to carry out calibration/validation activities of any satellite sensors measuring the radiance field in the visible and near-infrared part of the spectrum using pixels whose edge is at least 1.5 km away from the coast.

6.3 Atmospheric parameters

The atmospheric parameters, i.e. aerosol optical thickness, τ_a, were retrieved by applying the standard iterative-NIR atmospheric correction procedure [11] to MERIS, MODIS and SeaWiFS images. The pixels used for matchup comparison are all extracted from a 3 km by 3 km region centering the LISCO location. This extracted region has been screened to have a minimum distance from the shore larger than 2 km. Furthermore, individual pixel within the extracted region is excluded from the matchup comparison process if it has been flagged, through the data processing, by at least one of these conditions: land, cloud, stray light contamination, failure in atmospheric correction, reduced or bad navigation quality, negative Rayleigh-corrected radiance, viewing angle larger than 60°, solar zenith angle larger than 70°, aerosol optical thickness at 550 nm greater than 0.4.

Then satellite retrieved τ_a data is compared with the appropriate SeaPRISM data of LISCO site derived through the standard NASA AERONET processing. Because the aerosols might be very variable in time due to atmospheric transport, the time window centered on satellite overpass time was restricted to ±30 minutes to select the SeaPRISM data. The results of the matchup comparisons of τ_a taken around 443 nm are shown in Figure 6.2.a-c for the different satellite missions. Note that every τ_a data points of the pixels within the extracted region which passed the flag test specified earlier are included in the analysis.

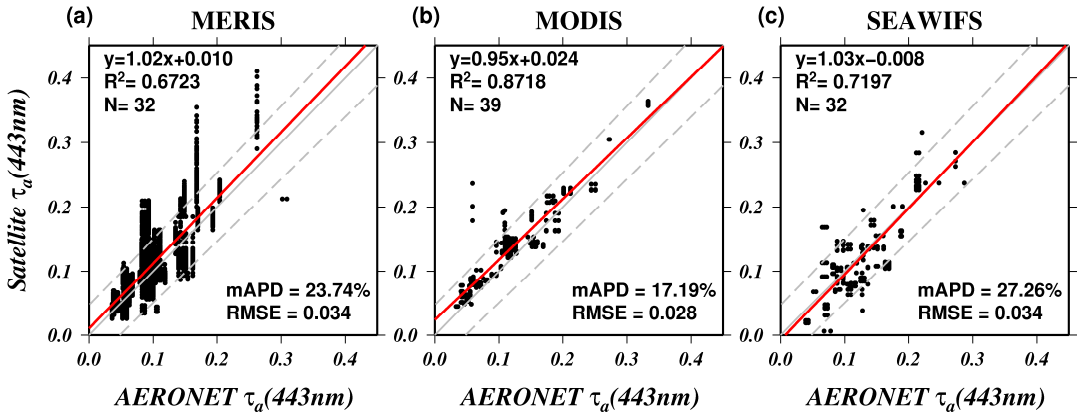

Figure 6-2. Matchup comparisons of aerosol parameters derived from satellite and SeaPRISM measurements (NASA processing) at LISCO site from October 2009 to July 2011. The aerosol optical thickness is compared for (a) MERIS, (b) MODIS, (c) SeaWiFS satellite. The red line is the regression line whose y is the equation and the dotted gray lines are the uncertainty level of the AERONET data. N is the total number of satellite images considered in each matchup comparison.

For every satellite mission, field and satellite data are significantly correlated with values of the coefficient of determination R^2 close to 0.7 for MERIS and SeaWiFS and greater than 0.87 for MODIS data. It should be noted that the lower R^2 value retrieved for MERIS is mainly due to spatial heterogeneity of τ_a derived over the 3-by-3-km pixel box because of the higher spatial resolution of MERIS images (~300 m) in comparison to MODIS and SeaWiFS 1-km spatial resolution, as it can be readily seen with the vertical distribution of the matchup points in Figure 6.2.a. The regression lines for the three missions are very close to the 1:1 line showing that no significant bias or non-linearity are present in the satellite retrievals. In the analysis, we used the median of the absolute percentage differences, denoted as *mAPD*, as statistical estimator. *mAPD* is defined as:

$$mAPD = 100 \times median\left(\frac{|y_i - x_i|}{x_i}\right) \quad (6.1)$$

with *x* taken for in-situ and *y* for satellite data.

The main reason to use the median value of the absolute percentage differences as the statistical parameter is to avoid the inclusion of extreme data points in the analysis. *mAPD* values are consistent with results achieved over the global database of the AERONET sites with values ranging from 17% for MODIS to 27% for SeaWiFS with MERIS as an intermediate with 24%. Furthermore, most of the satellite data falls within the uncertainty of the AERONET data which can be estimated by the following equation $0.05\times \tau_a \pm 0.03$ [98]. It is worth mentioning that the matchup points of MERIS outside the AERONET uncertainty range occur when the heterogeneity of the scene is high. However, part of those matchup points is well within this range showing the consistency of the MERIS retrieval despite the variability of the aerosols through the region of interest. The satisfactory derivation of the aerosol loading by three different missions using equivalent data processing proves the suitability of LISCO site for validation purposes of satellite atmospheric products.

6.4 Time series comparison between LISCO and satellite data

For the time series analysis purpose, satellite normalized water leaving radiances, $nLw(\lambda)$, were retrieved using the standard iterative-NIR atmospheric correction procedure [11] and current operational bi-directional correction algorithm [15] from MERIS, MODIS and SeaWiFS images. The SeaPRISM data of LISCO site used in this study are quality assured level 1.5 data (which is filtered through an automatic cloud screening based on almucantar and principal plane sky radiance measurements, and an elimination of data showing negative value, or exceedingly high

variance of measured radiances) and have been manually checked to make sure that no corrupted spectra were present in this dataset.

All MERIS, MODIS and SeaWiFS images were processed for the region over the LISCO site and for the period of LISCO activity since October 2009 up to July 2011. For the obtained level 2 images, a region of 9 km by 9 km is selected accordingly to the specific geography of the LISCO site. This region is then screened to locate the pixels flagged as cloudy pixel. As clouds are very bright in comparison to water, the presence of cloud in the vicinity of LISCO might very likely induce stray light effect for the non-cloudy pixels. Thus, if more than 10% of the pixels of this region are cloudy, the satellite image is excluded from the matchup comparison procedure. The pixels used for matchup comparison are all extracted from a smaller region of 3 km by 3 km region around the LISCO platform and a minimum distance from the shore larger than 2 km. Thus, this selected region of interest is expected to offer a minimum spatial heterogeneity of the water optical properties. Furthermore, any individual pixel is excluded from the matchup comparison process if it has been flagged, through the data processing, by at least one of these conditions: land, cloud, stray light contamination, failure in atmospheric correction, reduced or bad navigation quality, negative Rayleigh-corrected radiance, viewing angle larger than 60°, solar zenith angle larger than 70°, and aerosol optical thickness at 550 nm greater than 0.4. Finally, the average values of the 3 km × 3 km area are considered qualified for comparison with *in situ* data when at least 50% of the pixels are not affected by these standard flags.

The time series of comparisons of satellite OC sensors (MODIS, MERIS and SeaWiFS) and SeaPRISM $nLw(\lambda)$ data are plotted in Figure 6.3 for the period of January 1st to December 31st of 2010. Center wavelength sets of all OC sensors and SeaPRISM instrument are slightly different

from one another. As the result, *nLw* data were adjusted to a set of common center wavelengths shown in Figure 6.3 by linear interpolation. For 491, 551 and 668nm wavelengths the *nLw* data exhibit significant seasonal variations in agreement between the three satellite missions and the field data. In particular, a specific pattern of high water-leaving radiances is observable on March 17th 2010 resulting from an increase of sediment concentration following a significant storm event with higher riverine input and water body mixing. As a result, it is concluded that the temporal and seasonal changes are captured well by the satellite missions and the field instrumentation over the one year datasets of coincident acquisitions at the LISCO site. On the other hand, it should be noted that no outliers are distinguishable over this period in the satellite data, especially for the 491, 551 and 668nm wavelengths, after application of the filtering scheme. This proves that no unexpected environmental effects, which are not handled by the data processing, are perturbing the atmospheric correction procedure. It can be therefore concluded that satellite acquisitions over LISCO site are suitable for Ocean Color Radiometry purposes in this region, thereby demonstrating the ability to use the LISCO data for the satellite OC data validation, and development of the retrieval and correction algorithm specific for the typical coastal water conditions.

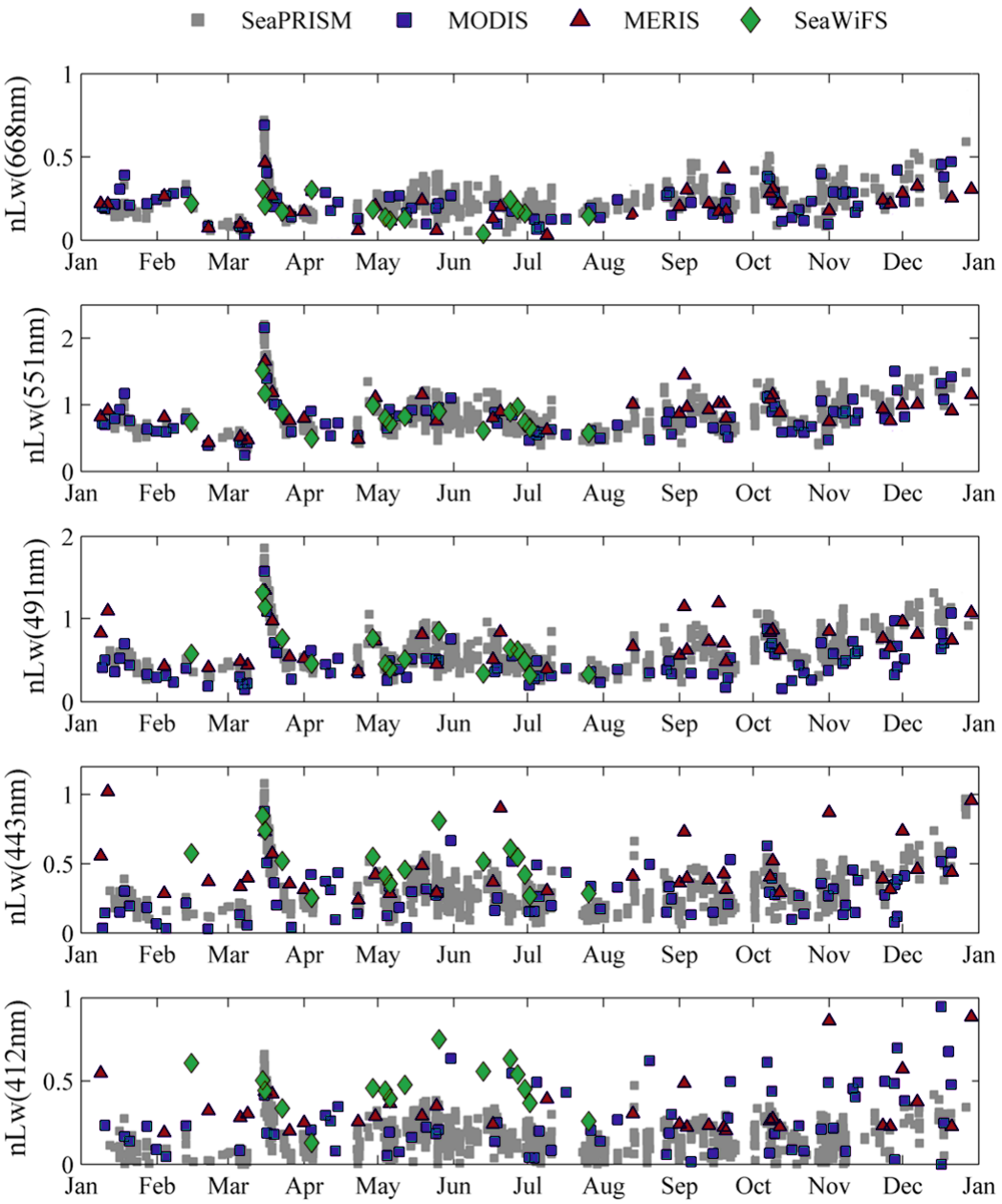

Figure 6-3. Time series of $nLw(\lambda)$, $mWm^{-2}\mu m^{-1}\ sr^{-1}$, derived from SeaPRISM (grey), MODIS (blue squares), MERIS (red triangles) and SeaWiFS (green diamonds) for year 2010.

6.5 Assessments of uncertainties in satellite Ocean Color data

The same procedures mentioned in the previous section, along with the selection of the in-situ data for the corresponding time window of ±2 hours centered on the satellite overpass have been used to plot the matchup comparisons between in-situ SeaPRISM and satellite data. Within that time window, SeaPRISM data collected at the most coincident times relative to the satellite overpass times are further selected to minimize perturbations induced by the temporal and spatial variability of the sea and atmosphere. Rigorous data quality screening procedures results in 35 MODIS, 10 MERIS and 7 SeaWiFS images to be performed the matchup comparisons against SeaPRISM measurements. The comparisons shown in Figure 6.4 indicate both qualitative and quantitative agreements between in-situ normalized water leaving radiance, $nLw_{(\mathrm{Spr})}(\lambda)$, and the one derived from the satellite, $nLw_{(\mathrm{SAT})}(\lambda)$, data. The strong spectral average correlation coefficient with the value greater than 0.91 also demonstrates the capacity for consistently monitoring $nLw(\lambda)$ data of the LISCO location from space. It was also found that regression lines between the satellite and in-situ *nLw* at those wavelength are very close to 1:1 line.

Statistical parameters such as, unbiased average percent difference (UPD) defined as:

$$UPD = \frac{1}{N}\sum_{i=1}^{N}\frac{x_i - y_i}{x_i} \tag{6.2}$$

and absolute average percent difference (AAPD) defined as:

$$AAPD = \frac{1}{N}\sum_{i=1}^{N}\frac{\left|x_i - y_i\right|}{x_i} \tag{6.3}$$

where in-situ data are taken as *x* and satellite data are taken as *y*, are obtained along with the R^2 values at each wavelength. These statistical parameters characterizing the comparison between the satellite and in-situ data are shown in Table 6.1. Very strong correlations with R^2 values around 0.9 were observed for 491 and 551nm wavelengths exhibiting the statistical consistency between the in-situ and satellite data for those wavelengths.

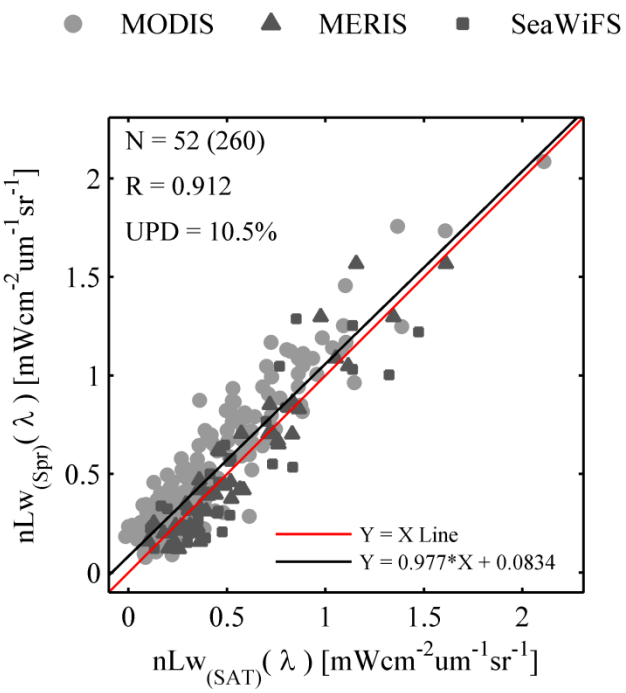

Figure 6-4. Scatter plot of the normalized water leaving radiance of MERIS, MODIS and SeaWiFS denoted as $nLw_{(SAT)}(\lambda)$ with that of SeaPRISM denoted as $nLw_{(Spr)}(\lambda)$. N is the total number of points for each spectral matchup, R^2 is coefficient of determination and UPD is the spectral average unbiased percent difference. The black and red lines are regression and 1:1 lines respectively.

The UPD parameters of every wavelengths exhibit satisfactory values which are within ±13% at every wavelengths except for 668nm and their spectral average is around 105%. Nevertheless, spectral average AAPD value is observed to be about 27% and the values are variable with the wavelength ranging from 16.53% at 551nm to 43% at 412nm. Although this is consistent with the known behavior of the atmospheric correction uncertainties, which increase from the red to the blue wavelengths [99], further analysis is needed to quantify these effects and such study however is beyond the scope of this research which is emphasized on the assessments of uncertainties in the OC data and reducing those uncertainties related only to the bidirectional correction effects.

Table 6-1. Statistical summary of the comparisons of $nLw_{(Spr)}$ and $nLw_{(SAT)}$ retrievals.

	Wavelength (nm)					*Spectral Average*
	412	***443***	***491***	***551***	***668***	
R^2	0.437	0.752	0.871	0.907	0.713	0.9124
***UPD* (%)**	-9.90	12.51	12.62	11.72	17.61	10.5211
***AAPD* (%)**	43.86	25.54	21.52	16.53	32.43	27.6392

The relatively high AAPD values obtained for the satellite versus SeaPRISM data comparisons appear to challenge the validation process, but are actually quite common in the analysis of satellite versus in situ data. To put the results achieved in this study in a more general context, it is appropriate to compare them with the similar study performed at the other AERONET-OC sites [30] and the matchup comparisons carried out between the satellite water-leaving radiance data and the in-situ one obtained from an optical mooring sited in deep ocean waters [100]. In

those studies, the latter exhibit 36.1, 22.0, 13.7, 12.9 and 40.3 in AAPD values at 412, 443, 491, 551 and 668nm wavelengths respectively for the matchup comparison performed with the MODIS. Similarly, the former study also exhibits differences on the order of tens of percent even though the comparisons are made in rather homogeneous Case-1 waters. Therefore, it is reasonably to conclude that the preliminary validation results presented for the LISCO $nLw(\lambda)$ data are consistent with those obtained from similar validation exercises for coastal waters.

6.6 Summary of the chapter

This chapter was devoted to the analysis that investigates LISCO's appropriateness as the OC data validation site. Detail analyses were carried out, using the OC data retrieved from MERIS, MODIS and SeaWIFS sensors. From the analysis, it is concluded that: (i) the adjacency effect is significant up to 1.5 km from the coast, that is, 2 km before the platform location, and becomes negligible in the direct vicinity of the platform and further offshore, (ii) for every satellite mission, atmospheric data of in-situ and satellite are significantly correlated with R^2 values greater than 0.7 for MERIS and SeaWiFS and greater than 0.87 for MODIS data thereby proving the suitability of LISCO site for validation purpose (iii) *nLw* data exhibit significant seasonal variations in agreement between the three satellite missions and the field data, and (iv) SeaPRISM *nLw* data strongly correlate with satellite *nLw* data of every missions showing R^2 value greater than 0.75 and 0.9 for the wavelength greater than 412 and 490nm respectively. Spectral average UPD value between the in-situ and satellite data are around 10% while UPD parameters of every wavelengths exhibit satisfactory values which are within ±13% at every wavelengths shorter than 668nm. However, a large dispersion between the in-situ and satellite data is observed at shorter wavelengths, particularly at 412nm which is quite common in the

analysis of satellite versus in situ data due to the known behavior of the atmospheric correction uncertainties combined with the low water leaving radiance at the blue channel because of the increased absorption by CDOM typical for the coastal location like LISCO. Nevertheless the overall results presented for the LISCO $nLw(\lambda)$ data are consistent with those obtained from similar validation exercises for coastal waters.

7 Development of the Case 2 Water Optimized Bidirectional Correction Algorithm for the Above Water and Satellite Water Leaving Radiance

7.1 Introduction to the bi-directional correction

The water leaving radiance field emerging from sea water is not generally isotropic because of the non-isotropic character of the volume scattering function (VSF) of the water body, coupled with non-isotropic illumination conditions that generally prevail above the sea surface. Furthermore, the wavy nature of water surface also has noticeable influence over the anisotropy of the water leaving radiance field. The bidirectional structure of the emerging radiance field has implications, particularly, in the processing of data from ocean-color satellite sensors as well as in calibration-validation activities for ocean-color sensors in which water-leaving radiances obtained under various geometrical configurations have to be quantitatively and accurately compared.

Variations in the bidirectional properties of the upward radiative field have already been extensively studied. Morel and Gentili [17] reported the variations in the bidirectional properties of the upward radiative field for case 1 waters, and their studies related the bidirectional variations of water leaving radiance field to chlorophyll concentration, [Chl]. Their findings were also corroborated by field measurements obtained using an underwater radiance distribution camera system in low-chlorophyll case 1 waters [19]. The anisotropy of the water-leaving radiance was also discerned from the series of BRDF measurements carried out from research aircraft for both case 1 and case 2 waters [101]. These airborne measurements results show good overall agreement with theoretical simulations. Also based on the field measurements exclusively performed for case 1 water types, Voss and Morel reported that the *Q* factor, defined

as the ratio between upwelling irradiance and upwelling radiance from the sea surface, was predicted to vary within 7% [20]. These predictive investigations were tentatively extended to typical case 2 waters, usually dominated by sediment or by colored dissolved organic matter (CDOM), and are currently being used in the NASA ocean color data processing procedures as the operational correction algorithm [15] for the retrieval of water leaving radiance from both case 1 and case 2 water types. Although the current operational algorithm is considered reasonably effective for case 1 water conditions, the validity of using of this correction algorithm in case 2 water types has not been really verified in natural environments [16]. Accordingly, the need for an improved version of a bidirectional reflectance correction algorithm particularly tuned for typical case 2 water conditions is the general consensus among the ocean color radiometry community [16, 22].

In case 2 waters, the more complex variability of the water composition results in the bidirectional properties of the upwelling radiance field being severely affected by concentrations of CDOM and mineral particles, which can have significant consequences on the correction factors both spectrally and angularly [22]. Consequently, extensive studies of the bidirectional properties of case 2 waters have been made through radiative transfer simulations with inputs of inherent optical properties (IOPs) typical for case 2 water types. Lee et al. proposed a semi-analytical model which relates nadir viewing remote sensing reflectance to single backscattering albedo and the solar zenith angle for both deep and shallow waters [102, 103]. Their model was later extended as both viewing and solar zenith angles dependent to be used for measurements made at other viewing angles [103]. Parameterization of the remote sensing reflectance as the function of single backscattering albedo, solar zenith as well as sensor viewing angles and the sea surface wind speed was also developed by Albert et al. [104, 105]. Nevertheless, these

models do not take into account the solar-sensor relative azimuth angle as an input parameter and, as a result, bidirectional variations in the azimuthal direction cannot be analyzed with the use of these models. Notably, Park and Ruddick [16] proposed a remote sensing reflectance model based on lookup tables of coefficients generated for large range of solar zenith, sensor viewing and solar-sensor relative azimuth angles to estimate the directional variation of the water leaving radiance field of both case 1 and case 2 waters. However, their model requires a phase function parameter defined by the contribution of suspended particles to the backscattering coefficients. But in remote sensing of coastal waters, accurate retrieval of such parameters of the water body remains highly challenging, and this can limit the operational use of the algorithm. Lee et al. [24] also proposed an approach centered on the inherent optical properties of water to remove the angular variations in remote sensing reflectance measurements. The evaluations of the overall performance of their BRDF correction scheme carried out with the use of the field measured data indicate slight improvement over the current standard correction algorithm.

In our previous studies [22], bidirectional reflectance effects of coastal waters were analyzed through extensive radiative transfer simulations of remote sensing reflectances typical for a wide range of coastal water conditions. Based on this analysis, we proposed a model that relates the single backscattering albedo to the remote sensing reflectance through a least mean squared optimization for a large range of IOPs and of viewing and illumination geometries.

7.2 Theorectical Background of Bidirectional Reflectance Distribution Function

The fundamental equation, shown below, relates any slanted radiance exiting the water, L_w, to the down-welling irradiance just above the sea surface, E_d, and to the absorption and backscattering coefficients of the water body (a and b_b) through three quantities: $\Re$ (a

dimensionless factor which merges all the reflection and refraction effects that occur when downward irradiance and upward radiance propagate through the air-water interface), f (a dimensionless coefficient which relates the magnitude of the irradiance reflectance just below the surface to the IOPs, namely a and b_b) and Q (the bidirectional function with units of sr^{-1}) as follows [15]:

$$L_w(\theta_s,\theta_v,\phi,\lambda,W,IOP) = E_d(\theta_s,\lambda)\times\Re(\theta_s,\theta'_v,W)\times\frac{f(\theta_s,\lambda,W,IOP)}{Q(\theta_s,\theta'_v,\phi,\lambda,W,IOP)}\times\frac{b_b(\lambda)}{a(\lambda)+b_b(\lambda)} \qquad (7.1)$$

The water-leaving radiance, L_w, at a given wavelength, λ, depends on its own direction, depicted by θ_v, the viewing zenith angle, and φ, the relative azimuth angle from the Sun's direction, on the illumination conditions (determined by the solar zenith angle, θ_s), on the sea state (parameterized via the wind speed, W) and the IOPs of the water body itself. In contrast, E_d is a function of the solar zenith angle, θ_s, and the wavelength only. The last factor $b_b/(a+b_b)$ is customarily called single backscattering albedo, and it is routinely denoted as ω. In the Equation (1) θ'_v is the in-water viewing angle and it is related to θ_v through Snell's law ($\sin\theta_v = n \sin\theta'_v$ where n is the refractive index of water).

In the equation (7.1), bidirectional reflectance paramer Q is defined as the ratio between upwelling irradiance, E_u, and upwelling radiance, L_u just below the sea surface:

$$Q(\theta_s,\theta'_v,\phi,\lambda,W,IOP) = \frac{E_u(\theta_s,\lambda)}{L_u(\theta_s,\theta'_v,\phi,\lambda,W,IOP)} \qquad (7.2)$$

Equation (7.2) implies that the Q would be a constant value of π for all viewing and illumination angles if the underwater radiance field were isotropic which is not usually the case. Our preliminary analysis [22] based on a microphysical model of the water constituents suggested

that Q can vary from 3.8 to 4.55 for $\theta_v = 0^o$ and $\theta_s = 30^o$ depending on the water compositions. and have variations with wavelength of about 15%. Fig. 7.1 (a & b) shows the Q spectrum of the two specific coastal water conditons. It can be clearly seen in the figures, Q values are highly variable with the wavelength and their spectral average values are around 4.3 sr^{-1} ruling out the isotropic under water radiance field condition for the assumed water types. Dependeny on the water constitutents can be also confirmed from the variations in both magnitude and spectral shape of each spectrum. The observed spectral variations in Q parameter implies that overall bi-directional distribution function will also be specral dependent.

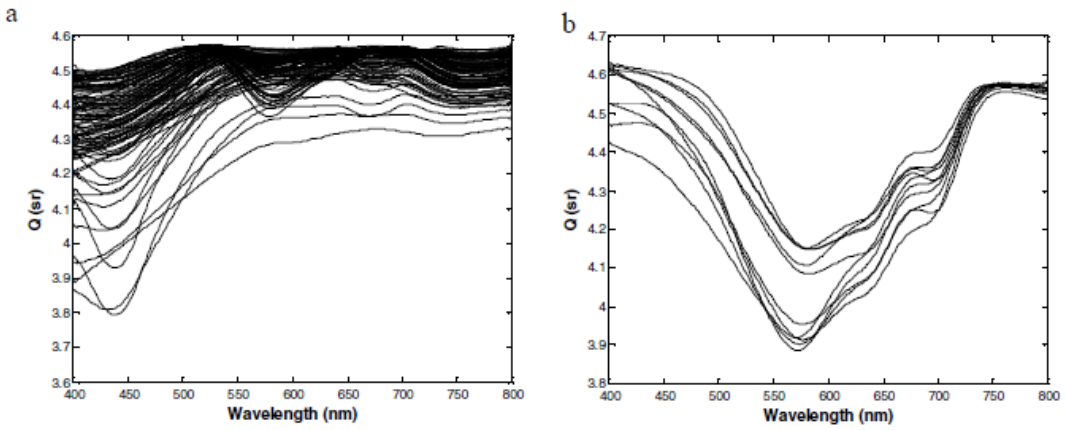

Figure 7-1. Simulated spectra of Q parameter for various water conditions: (a) $20 < [Chl] < 40$ mg/m^3, $a_{CDOM}(400nm) > 4m^{-1}$, NAP < 1 mg/m^3; (b) $20 < [Chl] < 40$ mg/m^3, $0 < a_{CDOM}(400nm) < 1$ m^{-1}, $10 < NAP < 15$ mg/m^3.

The above-water remote sensing reflectance is defined as [71]:

$$Rrs(\theta_s, \theta_v, \phi, \lambda, W, IOP) = \frac{L_w(\theta_s, \theta_v, \phi, \lambda, W, IOP)}{E_d(\theta_s, \lambda)} \tag{7.3}$$

Therefore, from equations (7.1) and (7.3), *Rrs* can be related to $\Re$, *f, Q* and the IOPs of the water as follows:

$$Rrs(\theta_s,\theta_v,\phi,\lambda,W,IOP)=\Re(\theta_s,\theta_v',W)\times\frac{f(\theta_s,\lambda,W,IOP)}{Q(\theta_s,\theta_v',\phi,\lambda,W,IOP)}\times\omega(\lambda) \tag{7.4}$$

7.3 Remote sensing reflectance model for the bidirectional correction of coastal waters

Gordon et.al [106] showed that nadir viewed remote sensing reflectance can be modeled as the polynomial function of the ω. It was also shown in [104, 107] that the factor f / Qcan be parameterized as the function of ω, θ_s and θ_v for both deep and shallow waters. In fact, ω can be considered as the representative of IOP input argument to f / Q factor and relationship between them has to be subsequently expressed in linear or higher order polynomial functions [22, 104, 107]. Consequently, relationship between *Rrs*(λ) and $\omega(\lambda)$ is also considered to be a second or higher degree polynomial [16, 24, 59, 105-107]. In this study, we model *Rrs*(λ) as the third order polynomial of $\omega(\lambda)$ as follows:

$$Rrs(\theta_s,\theta_v,\phi,\lambda,\omega)=\sum_{i=1}^{3}\alpha_i(\theta_s,\theta_v,\phi,\lambda)\omega^i(\lambda) \tag{7.5}$$

and the model coefficients, α_i, of the relationship (7.5) are tabulated for a large range of solar zenith (θ_s), viewing (θ_v), and relative azimuth (φ) angles as well as for wavelengths (λ). This polynomial model merges all bi-directional effects and directly relates the *Rrs* to the single parameter ω, allowing the BRDF correction to be performed using only the information on viewing and illumination geometries at the time of *Rrs* measurements. Thus, the model offers the computationally straightforward and simple approach for performing the directional correction

by forgoing the potential to model the different influences on L_w (and consequently on *Rrs*) separately as in equation (7.1) and (7.4).

Based on the simulated dataset which will be detailed in the following section, it was found that higher order polynomial render less Least Square (LSQ) curve fitting errors. Nevertheless, it was also observed that higher than third order polynomial fittings also show tendencies to give unrealistic *Rrs* values if the inputs ω values were outside the range of the simulated dataset. Thus we decided to use the third order as the optimal polynomial degree in our modeling. Fundamental difference between the proposed model and the previous models is that, unlike previous studies, model coefficients of the *Rrs* - ω relationship are generated as the wavelength dependent in order to better deal with the known spectral variation in *Q* factor [15, 22, 107]. Thus this proposed model allows the BRDF correction to be performed for each wavelength independently demonstrating the potential in better dealing with the spectral dependency of the BRDF. In the proposed model, the $\Re$ factor is integrated in the formulation by directly relating ω to the above-water simulated *Rrs*. Morel et al. previously reported large variation in $\Re$ with wind speed [15, 18]. Nevertheless, Gordon's revision [108] of their results later showed that the influence of surface roughness on the transfer of subsurface radiance through the air–water interface is minimal for surface viewing angles $\theta_v \leq 60^o$. Wang's evaluation of the surface reflection effects (in terms of the surface irradiance transmittance) on the water-leaving radiance with the change of solar-zenith angle for various aerosol optical properties, different wind speeds, and at various visible wavelengths as well reached to similar conclusion [109]. Albert and Mobley have also studied the dependence of irradiance reflectance for infinitely deep waters on surface wind obtaining the same results [104]. Also Park and Ruddick [16], based on the Hydrolight simulations for IOPs of both case 1 and 2 waters with the different input wind speeds

(0, 5 and 10ms^{-1}), showed that the effect of wind speed on bidirectional reflectance to be small. Following these conclusions we did not incorporate the wind speed (W) as an input parameter because its influence on both transfer of subsurface radiance through the air-water interface and underwater radiance field is minimal [24, 108].

7.4 Coastal Waters Radiative Transfer Modeling

7.4.1 Inherent Optical Properties (IOP) Model

A dataset of remote sensing reflectance spectra, $Rrs(\lambda)$, typical for coastal water conditions have been generated by us through radiative transfer simulations using Hydrolight 5 [110]. In these simulations, a four-component bio-optical model was assumed. The four components are: pure sea water, colored dissolved organic matters (CDOM), non-algal particulates, (NAP) and chlorophyll containing particles (phytoplankton). We use the subscripts "w", "y", "NAP" and "Chl" to identify these four components in the text below. The input parameters for the modeled IOPs of the components (except for pure sea water) are generated as uniformly distributed random variables in the prescribed ranges typical for coastal water conditions. The most important relationships used to compute the input IOP parameters are detailed in the following paragraphs.

The total spectral absorption coefficient $a(\lambda)$ is given as:

$$a(\lambda) = a_w(\lambda) + a_y(\lambda) + a_{Chl}(\lambda) + a_{NAP}(\lambda) \tag{7.6}$$

where the water absorption spectrum $a_w(\lambda)$ was obtained from Pope and Fry [111]. The chlorophyll absorption coefficient for case 2 waters was considered proportional to [Chl] as is often assumed [112] and is given by:

$$a_{Chl}(\lambda) = [Chl] \cdot a^*_{Chl}(\lambda) \tag{7.7}$$

where $a^*_{Chl}(\lambda)$ is the specific chlorophyll absorption coefficient, in m^2/mg. With a wide variety of specific absorption spectra available, in our simulations the set of specific chlorophyll absorptions was taken from Ciotti *et al.* [113] as a sum of specific absorptions of micro-plankton (a^*_{micro}) and pico-plankton (a^*_{pico}) with different weighting factors, S_f, as follows:

$$a^*_{Chl}(\lambda) = S_f \cdot a^*_{pico}(\lambda) + (1 - S_f) \cdot a^*_{micro}(\lambda) \tag{7.8}$$

where S_f = [0.1, 0.2, 0.3]. However, a recent study [9] showed that the use of these values generally leads to an underestimation of a^*_{Chl} in the red and near infra-red parts of the spectrum.

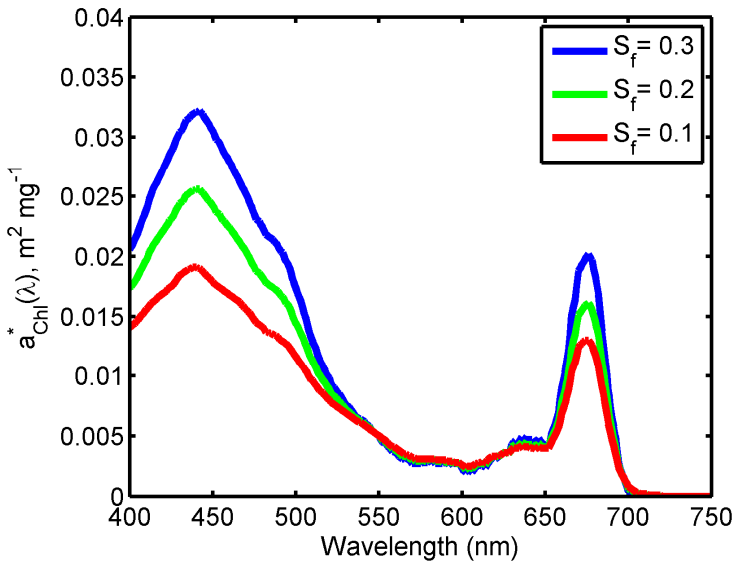

Figure 7-2. Specific chlorophyll absorption spectra used in simulations.

Consequently, we modified the spectra shape in the 650-700 nm part of the spectrum by setting a^*_{Chl} values at 675nm to 0.0142, 0.0156 and 0.02 m^2/mg for S_f = 0.1, 0.2 and 0.3 respectively. Figure 7.2 shows the specific chlorophyll absorption spectra used in the simulations.

The absorption spectra of both NAP and CDOM were both modeled as having exponentially decreasing magnitudes with respect to the wavelength and determined from their base reference values at 400 nm as in [114, 115]. Minerogenic particle type is assumed for NAP and its absorption spectra is modeled as follows

$$a_{NAP}(\lambda) = C_{NAP} \cdot a^*_{NAP}(400) \cdot \exp(-S_{NAP}(\lambda - 400)) \tag{7.9}$$

where $a^*_{NAP}(400)$ is the specific absorption of non-algal particles at 400nm, in m^2/g and C_{NAP} is their concentration in g/m^3. CDOM absorption was also modeled as shown below:

$$a_y(\lambda) = a_y(400) \cdot \exp(-S_y(\lambda - 400)) \tag{7.10}$$

where $a_y(400)$ is the absorption of CDOM at 400nm. In the equation (7.9) and (7.10) S_{NAP} and S_y denote the spectral slopes for the absorption spectral of NAP and CDOM respectively.

In a similar way, the total scattering coefficient was simulated as a sum of three components:

$$b(\lambda) = b_w(\lambda) + b_{Chl}(\lambda) + b_{NAP}(\lambda) \tag{7.11}$$

where $b(\lambda)$ is the total scattering coefficient, in m^{-1}. The scattering of NAP is modeled as a power law function [58] as follows:

$$b_{NAP}(\lambda) = C_{NAP} \cdot b^*_{NAP}(550) \cdot \left(\frac{550}{\lambda}\right)^{\gamma_{NAP}} \tag{7.12}$$

where $b^*_{NAP}(550)$ is the specific scattering of non-algal particles at 550 nm, in m^2/g.

The scattering coefficient of phytoplankton is calculated as the difference between the attenuation and the absorption coefficients:

$$b_{Chl}(\lambda) = c_{Chl}(\lambda) - a_{Chl}(\lambda) \tag{7.13}$$

where $b_{Chl}(\lambda)$ and $C_{Chl}(\lambda)$ are the scattering and attenuation spectra of phytoplankton. Then the attenuation spectrum is modeled as a power law function [116] as follows:

$$c_{Chl}(\lambda) = p \cdot [Chl]^{0.62} \cdot \left(\frac{550}{\lambda}\right)^{\gamma_{Chl}} \tag{7.14}$$

The backscattering coefficient can be decomposed as the sum of the contributions of the main scattering constituents:

$$b_b(\lambda) = b_{bw}(\lambda) + \bar{b}_{bChl} * b_{Chl}(\lambda) + \bar{b}_{bNAP} * b_{NAP}(\lambda) \tag{7.15}$$

where $b_{bw}(\lambda)$ is obtained in accordance with [117], and $\bar{b}_{bChl}$ and $\bar{b}_{bNAP}$ are the backscattering ratios for chlorophyll and non-algal particles, assumed to be independent of wavelength. $\bar{b}_{bChl}$ is calculated according to the following empirical parameterization proposed by Morel [15]:

$$\bar{b}_{bChl} = 0.002 + \{0.01[0.5 - 0.25\log_{10}(Chl)]\} \tag{7.16}$$

This allows us to use a particle phase function which is able to change progressively with [Chl] value, in such a way that the backscattering efficiency can decrease with increasing [Chl] [15]. $\bar{b}_{bNAP}$ is taken as a fixed value of 0.0183 assuming a strong mineral component in NAP.

Similar to the procedures followed for total absorption and scattering coefficients, the volume scattering function (VSF), denoted as $\beta(\psi)$, is decomposed as the sum of the contributions of pure water (β_w), non-algal particles (β_{NAP}), and chlorophyll containing particles (β_{Chl}) and can be written into the summation of all three components:

$$\beta(\psi) = \beta_w(\psi) + \beta_{NAP}(\psi) + \beta_{Chl}(\psi) \tag{7.17}$$

Equation (12) can be also written in terms of scattering coefficients and scattering phase functions (SPFs) of the contributing components as follow [60]:

$$b\overline{\beta}(\psi) = b_w\overline{\beta}_w(\psi) + b_{NAP}\overline{\beta}_{NAP}(\psi) + b_{Chl}\overline{\beta}_{Chl}(\psi) \tag{7.18}$$

where $\overline{\beta}(\psi)$ is the SPF of sea water. The SPF of pure sea water, $\overline{\beta}_w$, has been well studied and, for our simulations, is taken from [117]. In contrast to SPF of pure sea water, SPFs of non-algal and chlorophyllic particles are not well established and show high variability with the water types because of the diversity of size distributions, refractive indices, and shape anisotropies of particles [16]. The most commonly used SPF is Petzold's average-particle phase function derived from eight VSF measurements carried out by Petzold in the San Diego Harbor [118, 119]. However, Petzold's phase function results in a constant backscattering ratio of 0.0183, thereby prohibiting application of variable $\overline{b}_{bChl}$ values (which decrease with increasing [Chl], see equation (7.16)).

To meet this requirement for the backscattering ratio, we employed the phase functions given by the Fournier and Forand (FF) analytic expression [120], which is physically based on Mie theory and has reasonable assumptions about the index of refraction and particle size distribution of oceanic particles [119]. In its analytical form, the phase function is given by following equation:

$$\bar{\beta}_{FF}(\psi) = \frac{1}{4\pi(1-\delta)^2\delta^{\nu}}\left[\nu(1-\delta)-(1-\delta^{\nu})+[\delta(1-\delta^{\nu})-\nu(1-\delta)]\sin^2\left(\frac{\psi}{2}\right)\right] + \frac{1-\delta_{180}^{\nu}}{16\pi(\delta_{180}-1)\delta_{180}^{\nu}}\left(3\cos^2\psi-1\right) \tag{7.19}$$

where $\nu = \frac{3-\mu}{2}$ and $\delta = \frac{4}{3(n-1)^2}\sin^2\left(\frac{\psi}{2}\right)$.

Here ψ is the scattering angle, n is the real index of refraction of the particles, μ is the slope parameter of the hyperbolic distribution, and δ_{180} is δ evaluated at ψ=180°. Integration of $\bar{\beta}_{FF}(\psi)$ over backward scattering direction (i.e. $90^o \le \psi \le 180^o$) gives the backscattering ratio, $\bar{b}_b$ and the close form of the integral can be written into following equation:

$$\bar{b}_b = 1 - \frac{1-\delta_{90}^{\nu+1} - 0.5(1-\delta_{90}^{\nu})}{(1-\delta_{90})\delta_{90}^{\nu}} \tag{7.20}$$

where δ_{90} is δ evaluated at ψ=90°.

With the use of the FF analytical expression, phase functions with the desired backscattering ratios can be generated by setting the real index of refraction of the particles, n_p, and Junge slope parameter of their assumed distribution μ_p. Thus, $\bar{\beta}_{chl}$ used in our simulations are generated as FF phase functions by setting n_{pChl} to a fix value of 1.06 while varying the μ_{pChl} values to achieve the desired $\bar{b}_{bChl}$ values as described in [58, 119]. In other words, $\bar{\beta}_{chl}$ are generated for single particle type but with varying sizes. It should be noted here that the shape of the $\bar{\beta}_{chl}$ obtained with the FF phase functions is very similar to that of Morel [15] obtained through the T-matrix method (assuming randomly oriented spheroidal particles for all [Chl] levels used in our

simulations). $\overline{\beta}_{NAP}$ is also computed through the FF expression by setting n_{pNAP} and μ_{pNAP} to 1.1 and 3.58 respectively to give backscattering ratio 0.0183 as in [119].

Fig. 7.3 shows FF scattering phase functions: with a backscattering ratio of 0.0045 (red) used for algal particles with [Chl] = 10mg/m3, with a backscattering ratio of 0.007 (green) used for algal particles with [Chl] = 1mg/m3, and with a backscattering ratio of 0.0183 (blue) used for non-algal particles, together with the well-known Petzold's average particle phase function, reported for comparison.

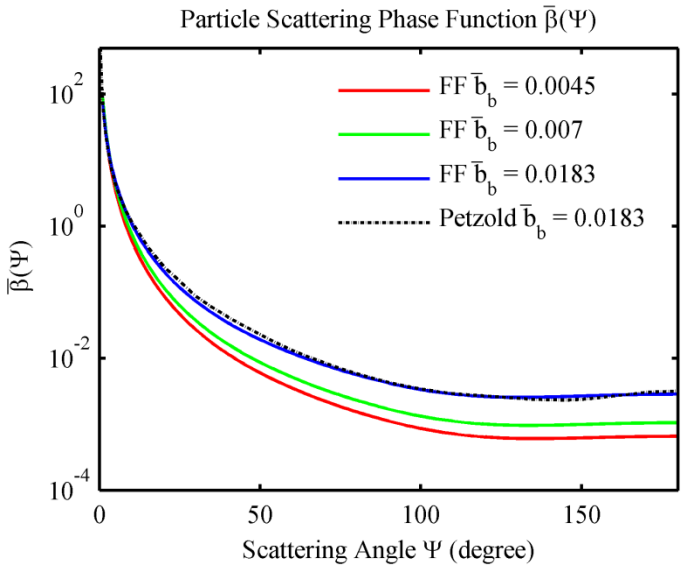

Figure 7-3. SPFs of particles used in simulations: FF b_b=0.0045 (red) is the SPF with a backscattering ratio of 0.0045 and used for algal particles with [Chl] = 10mg/m3, FF b_b =0.007 (green) is with [Chl] = 1mg/m3, FF b_b =0.0183 (blue) is used for non-algal particles, and Petzold b_b =0.0183 (black dotted line) is Petzold's average particle phase function.

7.4.2 Input Parameters for Simulation

IOP input parameters for the simulation are generated as independent random variables with uniform distribution in the prescribed ranges. These selected ranges of the input parameters comprehensively cover the realistic synoptic scale water conditions for typical coastal waters [121]. In addition, as input parameters are each independently generated from one another, resulting input dataset truly represents the conditions of the coastal waters in which constituents of the water body vary independently. Table 7.1 describes the ranges of the input parameters used in the simulation.

Table 7-1. Ranges of the IOP model input parameters used in the simulations (all parameters are randomly generated in the prescribed ranges with a uniform distribution).

Parameters	**Range**
[Chl]	1 ~ 10 mg/m^3
$a_y(400)$	0 ~ 2 m^{-1}
C_{NAP}	0.01 ~ 2.5 mg/m^3
S_y	0.01 ~ 0.02nm^{-1}
S_{NAP}	0.007 ~ 0.015nm^{-1}
$a^*_{NAP}(400)$	0.02 ~ 0.1 m^2/g
$b^*_{NAP}(550)$	0.5 ~ 1 m^2/g
γ_{Chl}	0.1 ~ 1.6
γ_{NAP}	0.5 ~ 2
p	0.1 ~ 0.5

With these assumed parameters, total absorption of the water at 412nm, $a(412)$, is in the range 0.1 - 2.3m^{-1}, the total particulate backscattering coefficient varies from 0.001 to 0.114m^{-1} and $\omega(\lambda)$ are in the range of 0.005 to 0.3. Figure 7.4 and 7.5 exhibits the total absorption and backscattering spectra resulted from the input parameters described in Table 7.1.

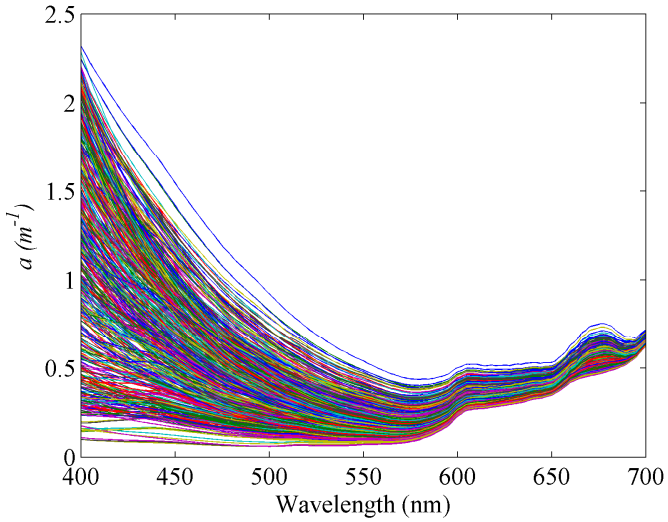

Figure 7-4. Total spectra absorption coefficient, $a(\lambda)$, in m^{-1} resulted from the input parameters used in simulations. All spectra used in the simulations are shown here.

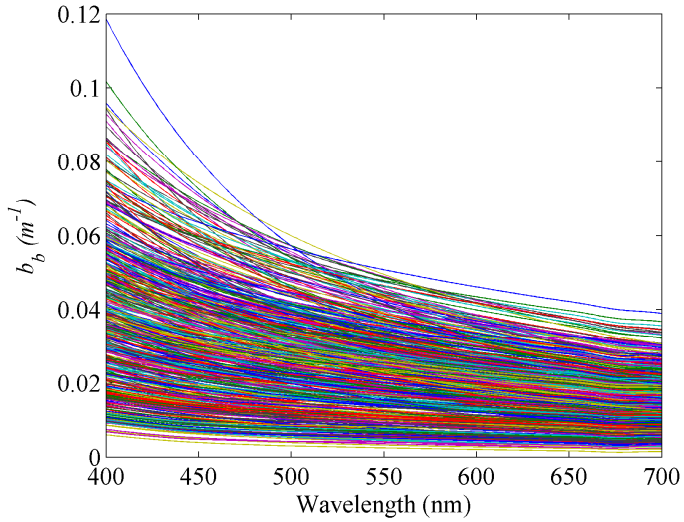

Figure 7-5. Total spectra backscattering coefficients, $b_b(\lambda)$, used in simulations.

Remote sensing reflectance, *Rrs*, water leaving radiance, L_w, and sea surface reflectance, ρ, were computed with Hydrolight with the following criteria using the IOP parameters specified above.

- 6 wavelengths λ: 412, 443, 491, 551, 668 and 753 nm
- 9 solar zenith angles θ_s : 0 to 80° at 10° intervals
- 9 sensor zenith angles θ_v : 0 to 80° at 10° intervals
- 13 relative azimuth angles φ : 0 to 180° at 15° intervals
- Wind speed W : 5 m/s with cloud free skies for the data set of remote sensing reflectance and radiance.

The three angles used as simulation inputs are defined as following: solar zenith angle, θ_s , and sensor zenith angle, θ_v, are the angles between the zenith line pointing upward and the direction to the Sun and the sensor respectively; the relative azimuth angle, φ , is defined as the angular difference between the sensor azimuth angle and the solar azimuth angle (i.e. the relative

azimuth is $\varphi = 0°$ when the sensor is in opposition with the Sun and $\varphi = 180°$ when the Sun is exactly behind the sensor.).

In our simulations we modeled the water as a homogeneous and infinitely deep medium for the sake of simplicity; therefore this modeling is applicable only to the optically deep waters where bottom reflectance is negligible. Only elastic scattering was considered and Raman inelastic scattering and fluorescence emission were not included. However, exclusion of Raman inelastic scattering has only a negligible impact on the accuracy of the modeling because of the relatively high particulate concentrations considered [15]. Chlorophyll fluorescence should not have impact on the output of water leaving radiance because the selected wavelengths are far from the fluorescence emission peak (located around 685nm) [122, 123]. The Hydrolight standard quad layout which essentially provides 10^o resolution in zenith (θ) and 15^o in azimuth (φ) directions was used. Hydrolight's built-in clear sky radiance model of Harrison and Coombes [124] and irradiance model of Gregg and Carder [125] were employed. Other atmospheric conditions such as sea-level pressure, relative humidity, horizontal visibility, and ozone concentration are set at default values which are described in the Hydrolight 5 technical documentation [77, 110].

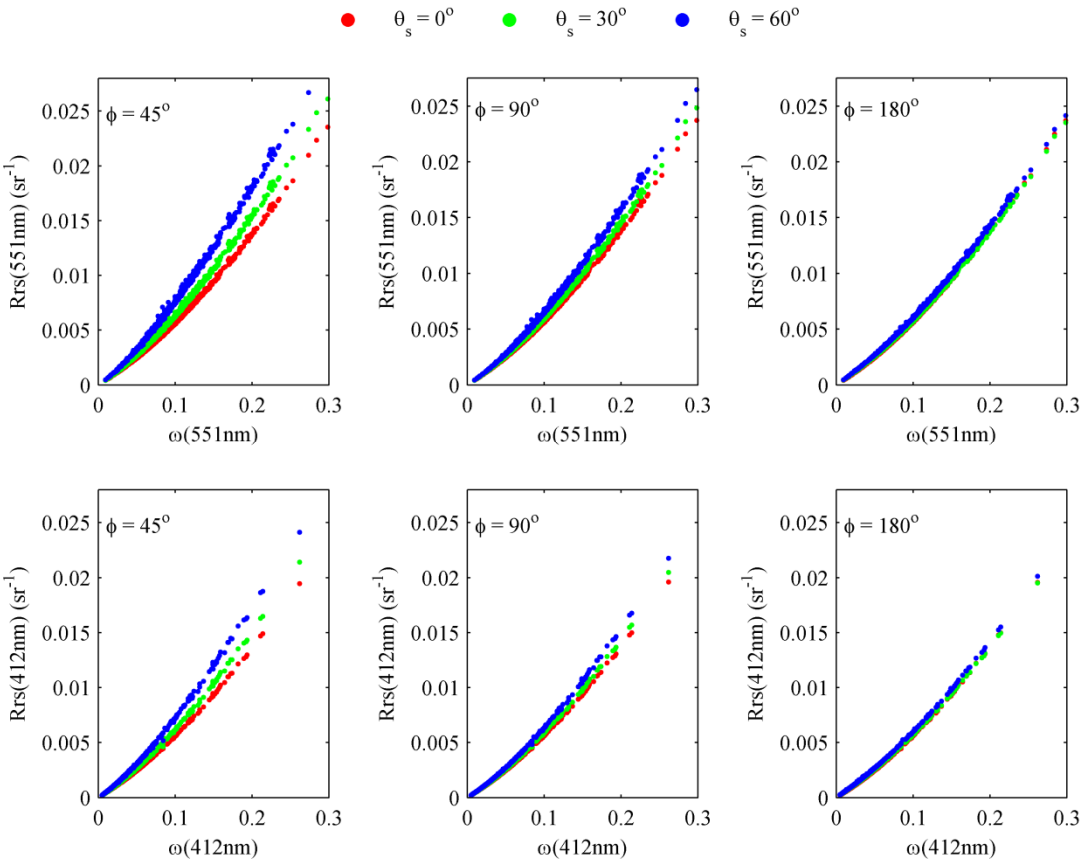

Figure 7-6. *Rrs*(λ) with respect to $\omega(\lambda)$ at viewing angle, θ_v = 40° for λ = 551nm (top row) and λ = 412nm (bottom row) and for the relative azimuth angles φ = 45°, 90° and 180° (from left to right). Simulations are shown for three solar zenith angles θ_s = 0° (red), 30° (green) and 60° (blue).

7.5 Simulation results and analysis

In general, $Rrs(\lambda)$ is strongly correlated with $\omega(\lambda)$ as known from the previous studies [16, 104, 106]. However, the value of $Rrs(\lambda)$ for a given value of $\omega(\lambda)$ does vary with the illumination and viewing geometries (i.e. solar and sensor angles) as discussed in previous chapter. Fig.7.6 shows the simulated $Rrs(\lambda)$ data as the function of $\omega(\lambda)$ for the three conditions of solar and viewing angles at 412 and 551nm. It is observed that the relationships between $Rrs(\lambda)$ and $\omega(\lambda)$ have a strong dependency on solar angles at low relative azimuth (φ) angles and that the dependency is becoming gradually weaker with increasing φ values. Similarly, Figure7-7 presents $Rrs(\lambda)$ data as the function of $\omega(\lambda)$ for the three conditions of sensor viewing and relative azimuth angles at 412 and 551nm at the fixed solar zenith angle, $\theta_s = 40^o$. Similar pattern regarding the changes in relative azimuth angle is observed as in the previous case.

Using the simulated $Rrs(\lambda)$ and $\omega(\lambda)$ data, we computed the sets of tabulated coefficients for the gridded values of θ_v, θ_s, φ and according to equation (4). For each grid, we used 500 data points of $Rrs(\lambda)$ and $\omega(\lambda)$ in a third order polynomial least-mean-square fitting procedure to produce the coefficients corresponding to the respective geometries and wavelengths. Table 7.2 shows the coefficients α_i for the nadir viewing and solar angles which are routinely employed in the estimation of Rrs from ω.

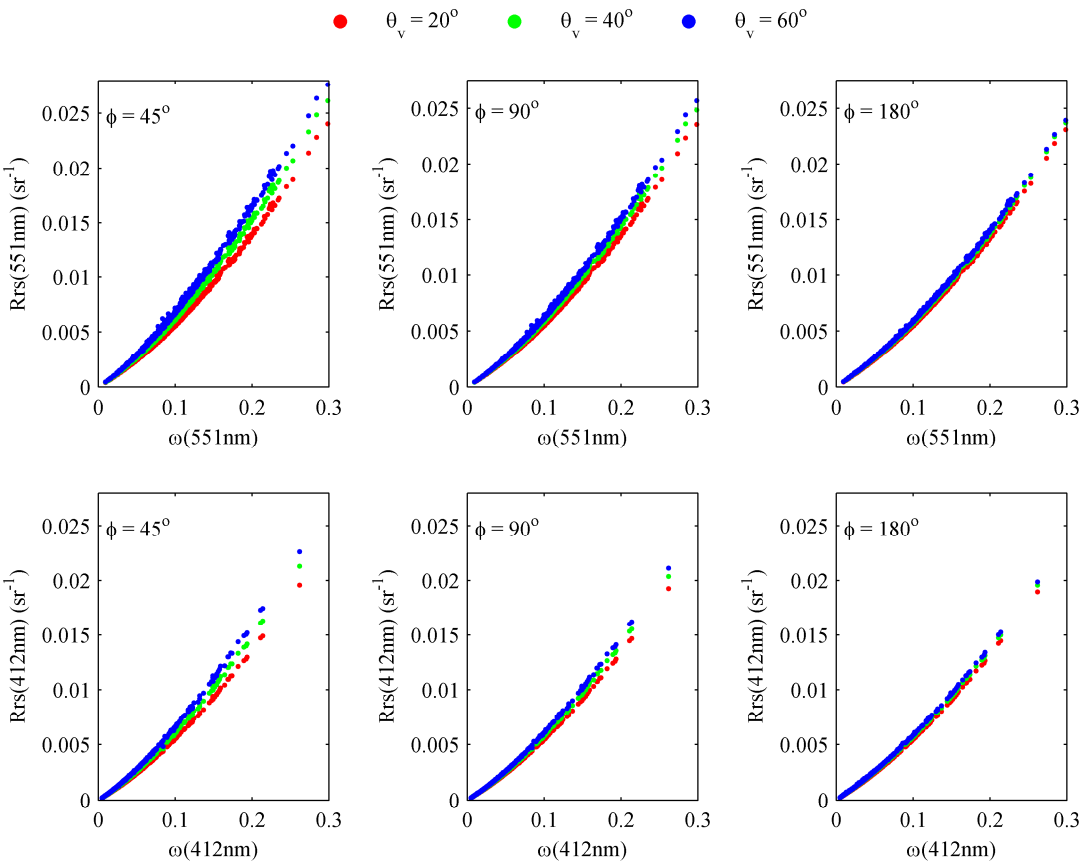

Figure 7-7. *Rrs*(λ) with respect to $\omega(\lambda)$ at solar zenith angle, θ_s = 40° for λ = 551nm (top row) and λ = 412nm (bottom row) and for the relative azimuth angles φ = 45°, 90° and 180° (from left to right). Simulations are shown for three viewing zenith angles θ_v =2 0° (red), 40° (green) and 60° (blue).

Table 7-2. Coefficients α_i for the nadir viewing and solar angles (θ_v = 0° and θ_s = 0°).

	λ(nm)				
	412	***443***	***491***	***551***	***668***
α_1	***0.04115***	***0.04073***	***0.04030***	***0.04023***	***0.03879***
α_2	***0.10186***	***0.09755***	***0.11102***	***0.1171***	***0.09425***
α_3	***0.01986***	***0.002898***	***0.00524***	***-0.01355***	***0.09660***

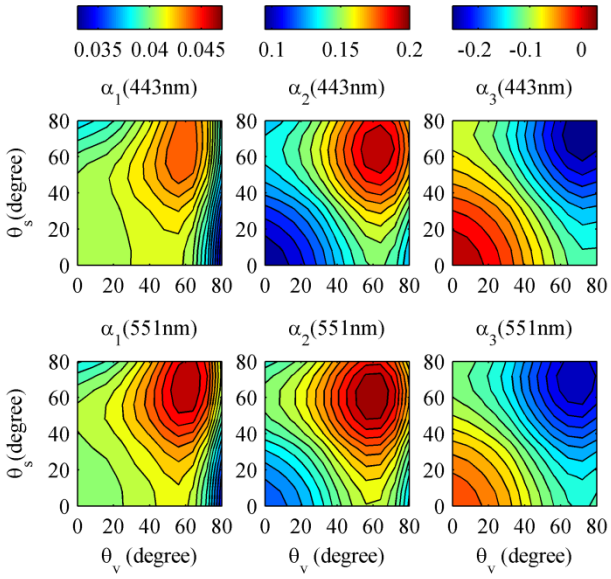

Figure 7-8. Color plots of the coefficients $\alpha_i(\theta_s, \theta_v, \phi, \lambda)$: α_1 (1st column), α_2 (2nd column) and α_3 (3rd column) are shown as a function of the sensor's zenith angle θ_v (x - axis) and the solar zenith angle θ_s (y - axis) while the relative azimuth angle φ is kept constant at 90°. The coefficients are shown for two wavelengths: λ = 443nm (top row), and 551nm (bottom row).

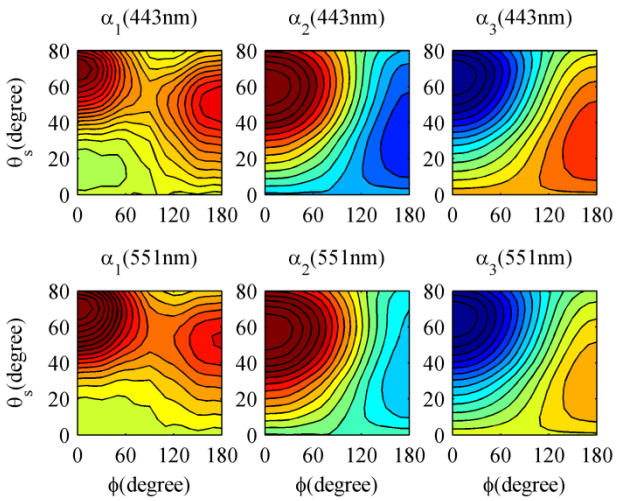

Figure 7-9. α_1 (1st column), α_2 (2nd column) and α_3 (3rd column) are shown as function of φ (x - axis) and the solar zenith angles θ_s (y - axis) while the sensor's viewing angle θ_v is kept constant at 40°. Color intensity values are the same as in the figure above.

Figure 7.8 and Figure 7.9 illustrate the variability of the coefficients α_i for the whole range of viewing and illumination geometries. Figure 7.8 highlights the dependency of the coefficients α_i on the solar and the sensor's zenith angles while the relative azimuth angle (φ) is kept constant at 90^o at which in situ above-water measurements are usually performed in order to minimize sky and sun glitters. In the figure, variations in both contour structure and color intensity are observed for the coefficient α_i images of the different wavelengths and thereby confirming the wavelength dependency of the *Rrs* - ω relationship. Figure 7.9 also shows the variability of the coefficients α_i with respect to φ (x - axis) and θ_s (y - axis) where θ_v is kept constant at 40° for the same wavelengths as in Figure 7.8.

7.6 Summary of the chapter

In this chapter, we presented the detailed discussion of the theoretical analysis of the bidirectional structure of water leaving radiance field based on its dependency on the illumination and viewing geometries, effects of sea surface roughness, wavelength dependency of *Q* factors and water constituents. Based on the those theoretical analysis, we proposed a third order polynomial remote sensing reflectance model to correct the bidirectional effects of the water leaving radiances retrieved from above water or space borne OC sensors.

We created a dataset of remote sensing reflectance spectra, $Rrs(\theta_v, \theta_s, \varphi, \lambda)$, through radiative transfer simulations made with Hydrolight. Simulations were performed for all ranges of viewing and illumination geometries with input parameters of the IOP model generated as uniformly distributed random variables in the prescribed ranges typical for coastal waters. A four-component microphysical bio-optical model was assumed in the simulations to synthetize the realistics coastal marine environment conditions where the constituents vary independent of each other. Variability of the parameters for the each component of biooptical model are also arranged in the realistics behaviors of the coastal environment based on the field observation. Specific considerations are included so that both absorption and scattering of the phytoplanton particulates vary with the size. In addition, particle scattering phase functions (SPF) are generated as the function of the particle size properties and type for each input biooptical component of each IOP datapoint. Therefore, this input data set fully cover the conditions of the natural coastal water environments exhibiting the potential to create the dataset of wide range of remote sensing reflectance spectra typical for the coastal waters.

With the use of the simulated remote sensing reflectance and input IOPs, we carried out the detailed analysis of the relationships between *Rrs* and ω based on the remote sensing reflectance model we proposed. From the analysis the coefficients α_i for the whole range of viewing and illumination geometries have been obtained. The dependency of the coefficients α_i on the solar, sensor's zenith and relative azimuth angles were analyzed and found to be sensitive enough to be used for the bidirectional correction of remote sensing reflectance. Moreover, variations in *Rrs* - ω relationship with wavelengths was also observed thereby confirming validity of the proposed model's wavelength dependent polynomial coefficients assumption.

8 Assessment of the Bidirectional Correction Algorithm

8.1 Theoretical Analysis

Based on the simulated dataset discussed in chapter 7, we carried out the assessment of the bidirectional correction performed with the proposed model (hereafter referred to as *CCNY* algorithm) as well as with the current operational algorithm [15] (referred to as *MG* algorithm). It should be noted that, although *MG* algorithm is operationally used by current above-water and satellite data processing [28] for bidirectional effect correction regardless of the water types, it was initially developed for case 1 water conditions. Thus, this theoretical analysis mainly intends to identify the amount of deviation induced by the case 1 - optimized bidirectional algorithm in typical coastal water conditions. In the following analysis we focus on $Rrs(\lambda)$ for a fixed viewing angle ($\theta_v = 40^o$) at which the sea-based above-water radiance measurements are usually performed [30, 126]. The solar zenith angle is ranging from 20^o to 70^o, and the relative azimuth angle, φ, from 60^o to 180^o. These solar zenith and relative azimuth angle ranges cover the realistic conditions in which above-water measurements can be performed with the relatively low contaminations of environmental effects [33].

In our assessments, simulated remote sensing reflectance at various viewing and illumination geometries, $Rrs(\theta_v, \theta_s, \varphi, \lambda)$, are initially translated into the nadir remote sensing reflectance, $Rrs(\theta_v=0, \theta_s=0, \varphi=0, \lambda)$, using both *CCNY* and *MG* algorithms. Then, those nadir remote sensing reflectance, $Rrs(\theta_v=0, \theta_s=0, \varphi=0, \lambda)$, obtained with the *CCNY* algorithm , (from here on denoted as $Rrs^0_{retrieved(CCNY)}$), and *MG* algorithm, (denoted as $Rrs^0_{retrieved(MG)}$), are compared with the corresponding exactly simulated nadir remote sensing reflectance denoted as Rrs^0_{actual}. $Rrs^0_{retrieved(CCNY)}$ is calculated as follows: (i) $\omega(\lambda)$ is derived by fitting $Rrs(\theta_v, \theta_s, \varphi, \lambda)$ to the

respective $\alpha_i(\theta_v, \theta_s, \varphi, \lambda)$ of the equation (4) ; (ii) $Rrs^0_{retrieved(CCNY)}$ is then calculated by plugging in $\omega(\lambda)$ obtained in the first step into equation (4) again together with α_i (θ_v=0, θ_s=0, φ=0, λ).

However, in the case of the *MG* algorithm, prior estimation of [Chl] is required. This estimation of [Chl] is carried out by using an empirical formula which relates the ratio of the water leaving radiances of the blue and green bands to [Chl] [15, 30]. In the *MG* algorithm considered in this study, we used the empirical formula (OC2) developed as a product of the SeaWiFS Bio-optical Algorithm Mini Workshop (SeaBAM) [69]. This empirical formula is also adopted in the operational AERONET-OC data processing for ocean color satellite data validation activities. The formula is defined as:

$$Chl = -0.0929 + 10^{0.2974 - 2.2429\ X + 0.8358\ X^2 - 0.0077\ X^3} \tag{8.1}$$

where:

$$X = \log_{10}\left(\frac{Rrs(490)}{Rrs(555)}\right) \tag{8.2}$$

The use of this blue-green ratio based [Chl] estimation algorithm (equation (8.1)) remains highly questionable for the optical properties typically retrieved in coastal waters [21, 127, 128]. Nevertheless, the focus of our analysis is to identify the deviation induced by the whole operational bidirectional correction process. Thus, this algorithm has been used here without modifications or adjustments. On the other hand, even if [Chl] values are retrieved with the reasonable accuracy, the current operational *MG* algorithm will still suffer from its single particle type assumption in which the contributions of scattering from the mineral rich non-algal particles (which are typical for coastal water conditions) are not considered. In our simulations we

assumed for equation (8.1) *Rrs*(490) ≈ *Rrs*(491) and *Rrs*(555) ≈ *Rrs*(551) which almost did not affect [Chl] values.

Based on the estimated [Chl] (equation (8.1)), f/Q factors are acquired from the look up tables [15]. After that $Rrs^{0}_{retrieved(MG)}$ is calculated as:

$$Rrs^{0}_{retrieved(MG)} = \frac{\Re_0}{\Re(\theta_v, W)} \times \frac{f_0(\lambda, Chl)}{Q_0(\lambda, Chl)} \times \frac{Q(\theta_s, \theta_v, \phi, \lambda, Chl)}{f(\theta_s, \lambda, Chl)} \times Rrs(\theta_s, \theta_v, \phi, \lambda) \qquad (8.3)$$

where $\Re_0$ denotes the particular values of $\Re$ when θ_v = 0. In the same way, f_0 denotes the particular value of f when θ_s = 0 and Q_0 denotes the Q value when θ_v = 0 and θ_s = 0. It is worth noting that the parameters f and Q of equation (8.3) are computed based on typical oceanic case 1 water optical properties.

Then, both $Rrs^{0}_{retrieved(CCNY)}$ and $Rrs^{0}_{retrieved(MG)}$ are compared to the Rrs^{0}_{actual} and the following statistical indicators are calculated. The absolute percent difference for each matchup denoted as δ_i:

$$\delta_i = 100 \times \frac{|x_i - y_i|}{x_i} \qquad (8.4)$$

The absolute average percent difference (AAPD) defined as:

$$AAPD = \frac{1}{N} \sum_{i=1}^{N} \delta_i \qquad (8.5)$$

and the average percent difference (APD):

$$APD = \frac{100}{N} \sum_{i=1}^{N} \frac{x_i - y_i}{x_i} \tag{8.6}$$

where x stands for Rrs^0_{actual} and y for either $Rrs^0_{retrieved(CCNY)}$ or $Rrs^0_{retrieved(MG)}$. In the comparisons, the statistical indicator AAPD provides the information regarding the dispersion while APD can be used to assess the expected bias between the compared datasets.

Those comparisons have been carried out for (i) Rrs^0_{actual} and corresponding *Rrs* (before the bidirectional effect is removed) in order to make the assessment of the bidirectional variations of the assumed water types for the viewing and illumination configurations mentioned above (*i.e.* $\theta_v = 40^o$, $20^o \leq \theta_s \leq 70^o$ and $60^o \leq \varphi \leq 180^o$), (ii) Rrs^0_{actual} and $Rrs^0_{retrieved(MG)}$ to identify the relative error resulting from the use of the case 1 water optimized correction algorithm for case 2 water conditions, (iii) Rrs^0_{actual} and $Rrs^0_{retrieved(CCNY)}$ to obtain the statistics of the error induced in the correction processes. Figure 8.1(a-e) shows the comparisons between $Rrs^0_{retrieved}$ and Rrs^0_{actual} at 412, 443, 491, 551 and 668nm, respectively, and for the viewing and illumination configurations mentioned above.

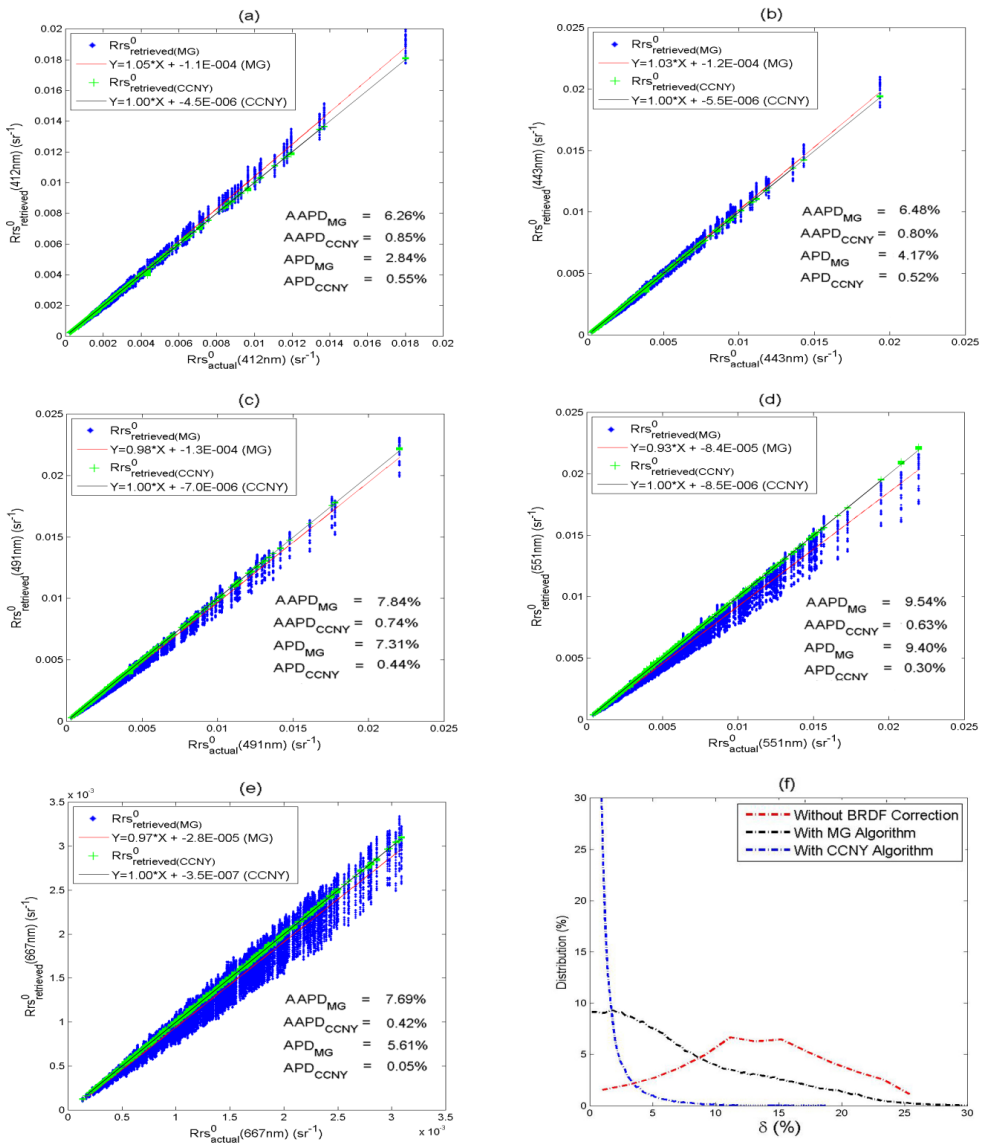

Figure 8-1. Comparisons between Rrs^0_{actual} and $Rrs^0_{retrieved}$ derived with MG (blue dots) and with CCNY (green dots) algorithms for $\theta_v = 40^o$, $20^o \leq \theta_s \leq 70^o$ and $60^o \leq \varphi \leq 180^o$ at (a) 412, (b) 443, (c) 491, (d) 551 and (e) 668nm. Regression lines between $Rrs^0_{retrieved(MG)}$ and Rrs^0_{actual} are shown in red and that of $Rrs^0_{retrieved(CCNY)}$ are shown in black. (f) Distribution of the absolute percent difference, δ, values between Rrs^0_{actual} and Rrs without BRDF correction (red), $Rrs^0_{retrieved(MG)}$ (black) and $Rrs^0_{retrieved(CCNY)}$ (blue) for each matchup.

It is observed that the comparisons show high AAPD values (6.26 to 9.5%) and APD values (2.8 to 9.4%) at all the wavelengths with the *MG* algorithm and regression line slopes between $Rrs^0_{retrieved(MG)}$ and Rrs^0_{actual} are 1.05, 1.03, 0.98, 0.93 and 0.97 respectively for 412, 443, 491, 551 and 668nm wavelengths. The dispersion between the two data is observed to be relatively smaller for the shorter wavelengths (412 and 443nm) and is largest at 551nm.

By contrast, the comparisons between $Rrs^0_{retrieved(CCNY)}$ and Rrs^0_{actual} exhibit much smaller AAPD (0.42 - 0.8%) and APD (0.054 - 0.55%) at all wavelengths. The regression lines between $Rrs^0_{retrieved(CCNY)}$ and Rrs^0_{actual} are very close to the 1:1 line for all wavelengths. Moreover, the retrieved differences between $Rrs^0_{retrieved(CCNY)}$ and Rrs^0_{actual}, which are mostly originating from the least-mean-square fitting procedure, are found to be negligible in comparison with the actual bidirectional variation, which is generally in the range of 10-20%, as can be readily seen in Figure 8.1(f).

In the Figure 8.1.(f), the histogram of the absolute percent difference values combined for all wavelengths shows that δ values between Rrs^0_{actual} and *Rrs* without BRDF correction are in the range of 2.3 to 25% and AAPD is around 13.5% which is consistent with previous studies [16, 22]. In addition, it can be seen that without the BRDF correction, only 9.5% of the dataset have absolute percent difference (δ) values within 5%, and more than two thirds of the data have δ values greater than 10%. These results demonstrate the importance of the bidirectional effect correction in the retrieval process if the water leaving radiances (and remote sensing reflectances) are to be retrieved within the ocean color sensor community's targeted accuracy level (*i.e.* less than 5% uncertainty) for above-water measurements.

Similarly, δ values between Rrs^{0}_{actual} and $Rrs^{0}_{retrieved(MG)}$ range from 0 to 27%. Nevertheless, AAPD is reduced to 7.56%. Moreover, it was observed that 43% and 70.6% of the data set have the δ values less than the 5% and 10% respectively. These results show that the bidirectional effect is reduced with the use of the *MG* correction algorithm and using the *MG* algorithm in coastal water conditions can still offer better retrievals than not correcting at all. However, 57% of the dataset have δ values greater than 5% and thus these results also outline the need of the bidirectional correction algorithm optimized for the case 2 water conditions. On the other hand, the distribution curve of δ values between Rrs^{0}_{actual} and $Rrs^{0}_{retrieved(CCNY)}$ shows much narrower range and 98.4% of the dataset have δ values less than 5%. The mean δ value is also drastically reduced to 0.69% demonstrating that *CCNY* BRDF correction algorithm works very well with the simulated dataset.

8.2 Noise Sensitivity Analysis

Water leaving radiances retrieved from above-water radiometric measurements are subject to uncertainty that arises from geophysical noise, such as rapid changes in environmental conditions, and sun and sky glints which are randomly fluctuating from the effects of surface waves. The current above water radiometry processing algorithm employs the glint filtering method in which only the lowest of multiple successive total sea radiance measurements taken within a short period are utilized in the processing of *Rrs* in order to minimize the effect of the glint [30, 33]. Such practices may result in the residual random component affecting the retrieved *Rrs*. Removal of the sky glint can also lead to residual errors which are not taken into account by the removal model [33]. For the satellite data, errors can arise from inaccuracies in atmospheric correction or from other sources. The analysis of such residual errors resulting from each step of

data processing procedures is beyond the scope of this study and deserves a dedicated study because of the importance of the topic. Here, our analysis simply intends to identify the proposed model's sensitivity to the noise, in other words, to verify whether the proposed model can still offer meaningful corrections (i.e. whether output $Rrs^0_{retrieved}$ are closer to corresponding Rrs^0_{actual} than $Rrs(\theta_v, \theta_s, \varphi, \lambda)$ are) when *Rrs* measurements are contaminated by geophysical noise, and to determine the threshold of noise level with respect to the *Rrs* signal. Since the proposed model performs the correction at each wavelength independently and modeling errors at each wavelength are much lower than assumed noise levels, the model's sensitivity to the noise at each wavelength can be evaluated from this analysis.

In order to test the applicability of the *CCNY* algorithm in the above water correction procedures we first added synthetic noise signals to the $Rrs(\theta_v, \theta_s, \varphi, \lambda)$ values before the BRDF correction was applied. Then, these noise-contaminated $Rrs(\theta_v, \theta_s, \varphi, \lambda)$ are converted to nadir remote sensing reflectances, using the *CCNY* algorithm. After that, noise-contaminated $Rrs^0_{retrieved(CCNY)}$ are compared to the respective Rrs^0_{actual} as in the previous section. For this analysis, synthetic noise signals are independently generated for each $Rrs(\theta_v, \theta_s, \varphi, \lambda)$ as random numbers with a Gaussian distribution with zero mean and standard deviation proportional to the corresponding *Rrs* values. Figure 8.2 shows the distributions of δ values (combined for all wavelengths) between Rrs^0_{actual} and noise-contaminated $Rrs^0_{retrieved(CCNY)}$ for three levels of noise (5%, 10% and 15%) together with the distribution of δ values for *Rrs* without a BRDF correction. It was found that AAPD values of the retrievals are increased to 4.0%, 7.9% and 12.9%, respectively, for the dataset with 5%, 10% and 15% noise levels. Although retrieval performances are lower with the introduction of noise to the signal, δ values for all noise levels are shifted toward smaller values

comparing to the δ values for *Rrs* without BRDF correction. Thus, it shows that even noise-contaminated *Rrs* measurements can still considerably benefit from the bidirectional correction.

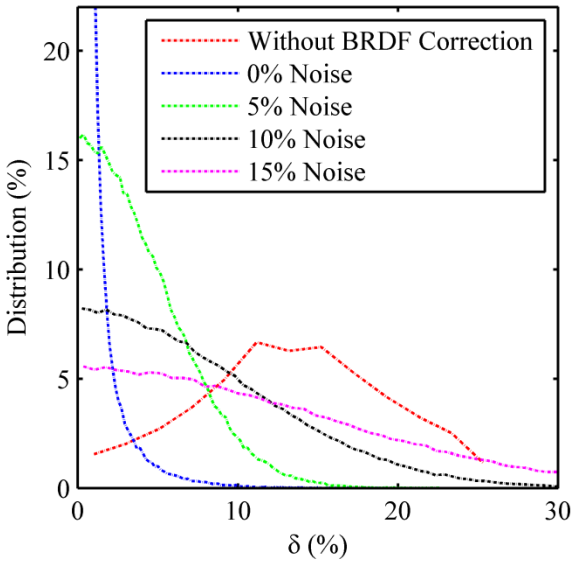

Figure 8-2. Distribution of the absolute percent difference (δ) values for $Rrs^{0}_{retrieved(CCNY)}$ infected with four different noise levels, 0% (blue), 5% (green) , 10% (black) and 15% (magenta). The red curve corresponds to the case where *Rrs* is not corrected for BRDF.

8.3 Bidirectional Reflectance Distribution Correction of Above-water Measurements

As was mentioned in chapter 7, performance of the proposed BRDF correction approach was also evaluated by measurements obtained at LISCO. One of the major advantages of the LISCO instrumentation set is that HyperSAS and SeaPRISM instruments acquire data almost concurrently but with different azimuth angles in respect to the Sun as the day progresses, except for the time when the Sun is exactly at South when both instruments point West. As both

instruments make measurements within 10 minutes window, it is reasonable to consider that the composition of the water constituents within that time window remains the same. Ideally, observed variations in the water leaving radiances acquired by the two instruments can be attributed to the variations due to the bidirectional reflectance distribution function (BRDF) only. Hence, the assessments of the performance of the BRDF corrections can be made by comparing the nadir remote sensing reflectance obtained from the SeaPRISM [denoted as $Rrs^0_{Spr}(\lambda)$] and from HyperSAS [denoted as $Rrs^0_{HS}(\lambda)$]. However, it should be pointed out that directional fluctuations in the measured sea radiance are also induced by the sun and sky light reflections on the ruffled surface which, at the end, may create significant uncertainties in the retrieved water-leaving radiance [33, 75].

It should be also reminded that the major difficulties of above-water measurements are resulted from uncertainties arisen from the sun and sky glint components of the total sea radiance measurements. These components are resulted from the randomly fluctuating windblown surface waves. These fluctuations induce different geophysical noise that needs to be removed from SeaPRISM and HyperSAS data and even after removal steps there still may be residual random components affecting the final *Rrs* values. In fact, these residual random components may be considered to have the same effect as the noise on the correction procedures as shown in noise sensitivity analysis section.

In the following, the consistency and the efficiency of the proposed *CCNY* as well as current *MG* bidirectional correction algorithm are assessed based on the dataset of $Rrs(\theta_v, \theta_s, \varphi, \lambda)$ obtained from two concurrent measurements of HyperSAS and SeaPRISM. This dataset covers a period of more than one year encompassing the full natural variability of atmospheric and water conditions

and, as the result, correction algorithms' advantages and disadvantages over one another can be fully discerned for the whole range of natural conditions and environments.

It should be noted that the BRDF correction usually accounts for 10-20% of $Rrs(\lambda)$ [16, 17]. Thus, the estimation of the bidirectional correction quality is a challenging task especially for the field data where residual random components resulted from the variability of the natural environment contribute significantly to total uncertainties. Therefore, it is of paramount importance to filter out the data corrupted by unexpected environmental effects or any stochastic artifacts beforehand. The filtering procedure for quality assurance has already been developed for the SeaPRISM system in the framework of AERONET-OC distribution [29] and all the data we used in this study are quality checked level 1.5 cloud screened data [17]. Similarly, a specific HyperSAS data filtering procedure which has been discussed in chapter 5 are closely followed in this study for the data processing.

8.3.1 Method and Data Processing

Remote sensing reflectance spectra, $Rrs(\lambda)$, for a specific viewing and illumination condition are calculated as described in [11] as follows:

$$Rrs(\theta_s,\theta_v,\phi,\lambda)=\frac{L_t(\theta_s,\theta_v,\phi,\lambda,W)-\rho(\theta_s,\theta_v,\phi,W)L_{sky}(\theta_s,\theta_v,\phi,\lambda)}{E_d(\theta_s,\lambda)} \tag{8.7}$$

Following our previous study [33], the total radiance (L_t) utilized in equation (8.7) for the SeaPRISM instrument is obtained from Level 1.5 cloud screened average total sea radiance data of AERONET-OC data distribution. In the case of HyperSAS, L_t is calculated by averaging the lowest 5% of the sea radiance measurements taken during the two minutes data acquisition time. HyperSAS performs 45 to 80 total sea radiance measurements during its two minutes data

acquisition window, depending on the brightness of the total radiances being obtained. Taking the lowest 5% allows the averaging of at least two measurements during every cycle of two minutes data acquisition for further processing. On the other hand, the sky radiance, L_{sky}, is determined by simply averaging all sky radiance measurements. The sea surface reflection coefficient, $\rho(\theta_v, \theta_s, \varphi, W)$, for the desired exact viewing and illumination geometries, and wind speed is obtained by performing a linear interpolation on the reflection coefficient dataset acquired through Hydrolight's simulations described in chapter 7. Input surface wind speed data for each data acquisition cycle is acquired from the National Weather Service. Down-welling irradiance, $E_d(\lambda)$, data is derived from the standard AERONET-OC SeaPRISM data with the use of the equation (4.6) and (4.8), and applied in the calculation of $Rrs(\lambda)$ for both HyperSAS and SeaPRISM systems.

Then, hyperspectral HyperSAS data were integrated with the sensor relative spectral response function of each SeaPRISM bands in order to produce equivalent data for both systems. The data involved were restricted to SeaPRISM measurement sequences taken within ±10 min off HyperSAS sequence intervals. In addition, findings from our previous study suggest that the contamination by environmental effects of the retrieved water leaving radiance becomes sensitive for $\varphi < 60°$ regardless of the sun elevation, with uncertainties higher than 5% [33]. As a consequence, it has been decided to eliminate from the analysis HyperSAS measurements taken with $\varphi < 60°$.

8.3.2 Assessment of Bidirectional Correction via LISCO Data

In the following, we first show the inter-comparisons between the remote sensing reflectance of HyperSAS and SeaPRISM before the bidirectional effect are corrected [denoted as $Rrs_{HS}(\lambda)$ and

$Rrs_{Spr}(\lambda)$, respectively]. This comparison (see Figure 8.3 (a & b)) allows us to make the assessment of the variation in two measurements before the bidirectional effects are removed. Secondly, we perform the comparisons between the final nadir remote sensing reflectance of both instruments [denoted as $Rrs^{0}_{HS}(\lambda)$ and $Rrs^{0}_{Spr}(\lambda)$] processed with both the *CCNY* and *MG* algorithms (see Figure 8.4 (a & b)). Finally, we compare the final nadir remote sensing reflectance of both instruments processed with *CCNY* algorithm (denoted as $Rrs^{0}_{retrieved(\mathrm{CCNY})}$) to those of *MG* algorithm (denoted as $Rrs^{0}_{retrieved(\mathrm{MG})}$) (see Figure 8.5). In the comparisons, because neither SeaPRISM nor HyperSAS data can be assigned as the reference, the following statistical indicators given in % are used.

The absolute relative percent difference (ARPD) defined as follows:

$$ARPD = \frac{200}{N}\sum_{i=1}^{N}\frac{|y_i - x_i|}{x_i + y} \tag{8.8}$$

and the unbiased relative percent different (URPD):

$$URPD = \frac{200}{N}\sum_{i=1}^{N}\frac{y_i - x_i}{x_i + y_i} \tag{8.9}$$

where SeaPRISM data are taken as x and HyperSAS data are taken as y.

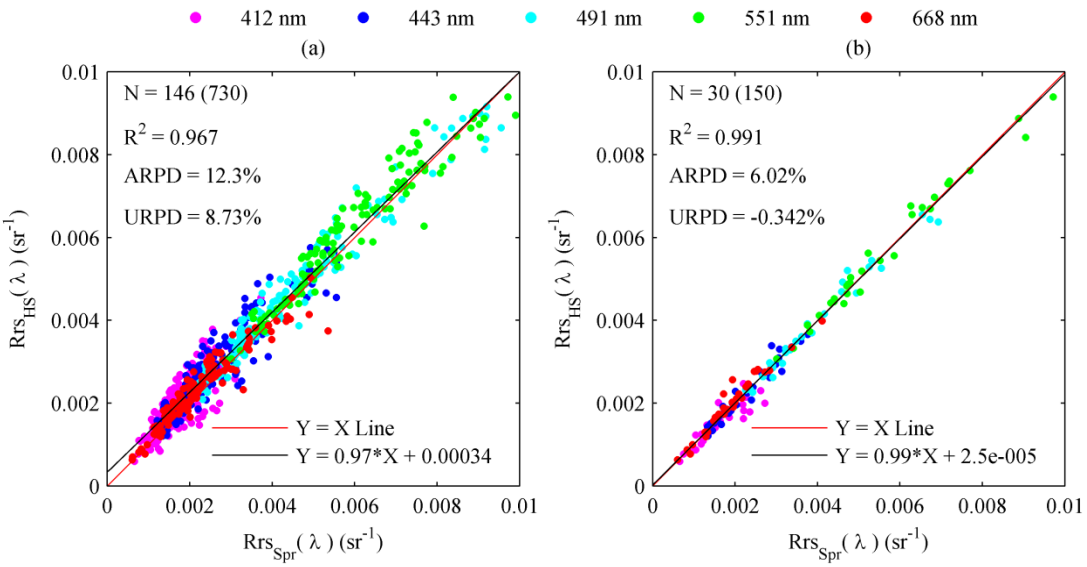

Figure 8-3. Intercomparisons of remote sensing reflectances (in sr^{-1}) derived from SeaPRISM and HyperSAS before correction for the bidirectional effect: (a) relative azimuth angles for HyperSAS observations are restricted in the $60^o \leq \varphi \leq 180^o$ range; (b) relative azimuth angle range is restricted to $80^o \leq \varphi \leq 100^o$. N is the total number of the comparisons, the bracketed value is the number of different measurement sequences used in the comparison.

Figure 8.3 (a) shows the comparison of remote sensing reflectance measurements of HyperSAS and SeaPRISM ($Rrs_{HS}(\lambda)$ and $Rrs_{Spr}(\lambda)$) before the bidirectional effect is removed for all the data used in this analysis. The comparison exhibits strong correlations between HyperSAS and SeaPRISM data with R^2 value around 0.967 and the regression line between two data is also very close to the 1:1 line. The URPD and ARPD values which show the bias and dispersion between two data are 8.73% and 12.3% respectively. However, when the relative azimuth angle range for HyperSAS instrument is restricted to $80^o \leq \phi \leq 100^o$ range (see Figure 8.3(b)), URPD and ARPD

values are reduced down to -0.342% and 6.02% respectively. In addition, the R^2 value is increased to 0.991 and the regression line becomes closer to the 1:1 line, showing a better consistency between the two measurements. In fact, with this restricted relative azimuth range, HyperSAS and SeaPRISM measurements are taken for an azimuth within $\pm 10^o$ and thus bidirectional effects for the measurements of both system are about the same. Therefore, it can be considered that this statistical difference between the two comparisons arises from the bidirectional variation of the water leaving radiance as well as from possible residual sun and sky glint effects.

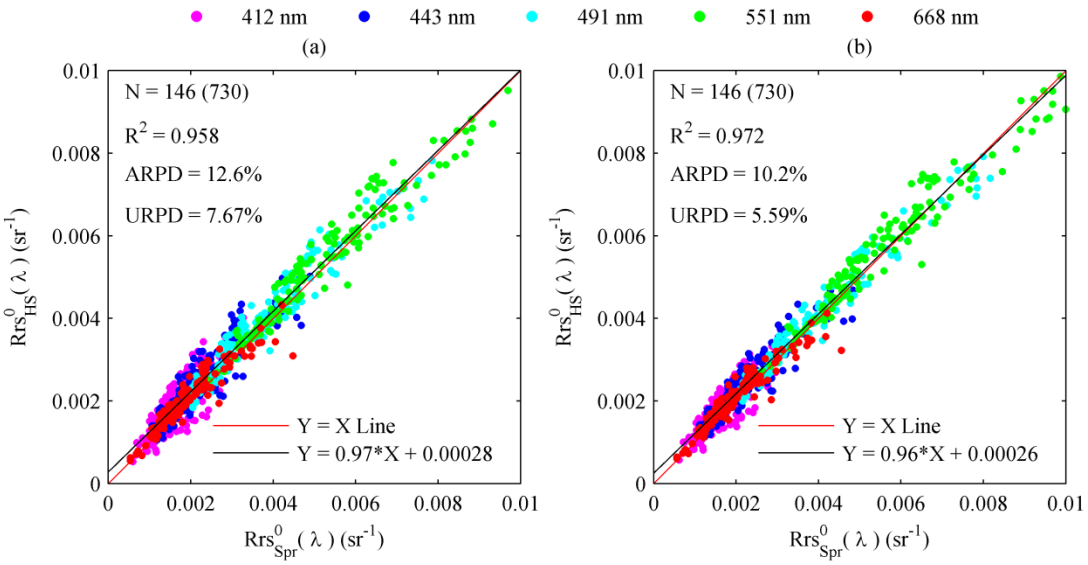

Figure 8-4. Inter-comparisons of SeaPRISM and HyperSAS remote sensing reflectance measurements (in sr^{-1}) after the bidirectional effect is corrected: (a) Processed with *MG* algorithm (b) Processed with *CCNY* algorithm. Relative azimuth angles, φ, for HyperSAS observations are the same as (a).

Comparisons of the $Rrs^{0}_{HS}(\lambda)$ and $Rrs^{0}_{Spr}(\lambda)$ processed with *MG* and *CCNY* algorithms are shown in Figure 8.4 (a) and (b), respectively. In the comparison of the $Rrs^{0}_{HS}(\lambda)$ and $Rrs^{0}_{Spr}(\lambda)$ processed with *MG* algorithm, the URPD value is reduced down to 7.67% showing 1.06% reduction in relative percent difference compared to the same data not corrected for the bidirectional effects. However, its ARPD value is increased by 0.3% compared to the value before the correction. The R^2 value is also observed to be reduced down to 0.958.

Table 8-1. Statistical summary of the intercomparisons of SeaPRISM and HyperSAS remote sensing reflectance measurements. (1st row) Before the bidirectional effect is removed ($60^o \leq \varphi \leq 180^o$ range is shown in black and $80^o \leq \varphi \leq 100^o$ is shown in red). (2nd row) After the bidirectional effect is corrected with *MG* algorithm. (3rd row) Corrected with *CCNY* algorithm.

		Wavelength (nm)					***Spectral Average***
		412	***443***	***491***	***551***	***668***	
Before BRDF correction	***R^2***	***0.7(0.81)***	***0.85(0.94)***	***0.95(0.98)***	***0.96(0.98)***	***0.95(0.95)***	***0.967(0.991)***
	ARPD	***21(11.3)***	***16(5.81)***	***7.86(3.23)***	***5.9(3.12)***	***10.8(6.67)***	***12.3(6.02)***
	URPD	***12.1(-5.9)***	***11.6(-0.02)***	***5.18(0.66)***	***3.56(0.67)***	***7.48(4.21)***	***8.73(-0.34)***
Corrected with MG algorithm	***R^2***	***0.689***	***0.833***	***0.941***	***0.945***	***0.883***	***0.958***
	ARPD	***20.35***	***16.3***	***8.17***	***6.99***	***11***	***12.6***
	URPD	***12.3***	***11.8***	***5.36***	***3.76***	***7.73***	***7.67***
Corrected with CCNY algorithm	***R^2***	***0.749***	***0.878***	***0.961***	***0.957***	***0.906***	***0.972***
	ARPD	***17.8***	***13.3***	***6.09***	***5.04***	***8.76***	***10.2***
	URPD	***9.65***	***9.41***	***3.46***	***2.11***	***5.28***	***5.59***

These results indicate that the dispersion between the two data is rather increased by the *MG* correction procedure. This shows the inadequacy of bidirectional correction based on the assumption of case 1 water for the typical LISCO waters. On the other hand, comparison of the same data processed with the *CCNY* algorithm shows reduction in both ARPD and URPD values (2.1% and 3.14%, respectively) with respect to the comparison of the data not corrected for the bidirectional effects while R^2 is increased to 0.972. Therefore, this indicates that with the use of *CCNY* bidirectional correction algorithm, dispersion between the two measurements resulted from the different viewing configuration can be reduced, thereby demonstrating the relevance and appropriateness of the *CCNY* bidirectional correction for the water leaving radiance measured by the HyperSAS and SeaPRISM instruments in the moderately turbid waters of LISCO site. It can also be observed that both ARPD and URPD values of the data corrected with the *CCNY* algorithm are lower than those of *MG* algorithm at every wavelength showing 1.95% to 3.0% improvements in terms of ARPD and 1.65% to 2.65% in terms of URPD.

Figure 8.5 shows the inter-comparisons between $Rrs^0_{retrieved(CCNY)}$ and $Rrs^0_{retrieved(MG)}$. It is observed that the relative absolute percent difference between the output nadir remote sensing reflectance of the two algorithms ranges from 0 to 14.5%, where the largest differences found at 551nm with AAPD between the outputs of the two algorithms is 6.14%. The slopes between the output final nadir remote sensing reflectances of the two algorithms are 1.05, 0.95 and 0.905 for 412, 491 and 551nm wavelengths suggesting that the *MG* algorithm is overestimating the nadir remote sensing reflectances at 412nm and underestimating them at 491 and 551nm. It should be noted that comparisons carried out with the field measurement data illustrate similar slopes with those carried out with the simulated data set.

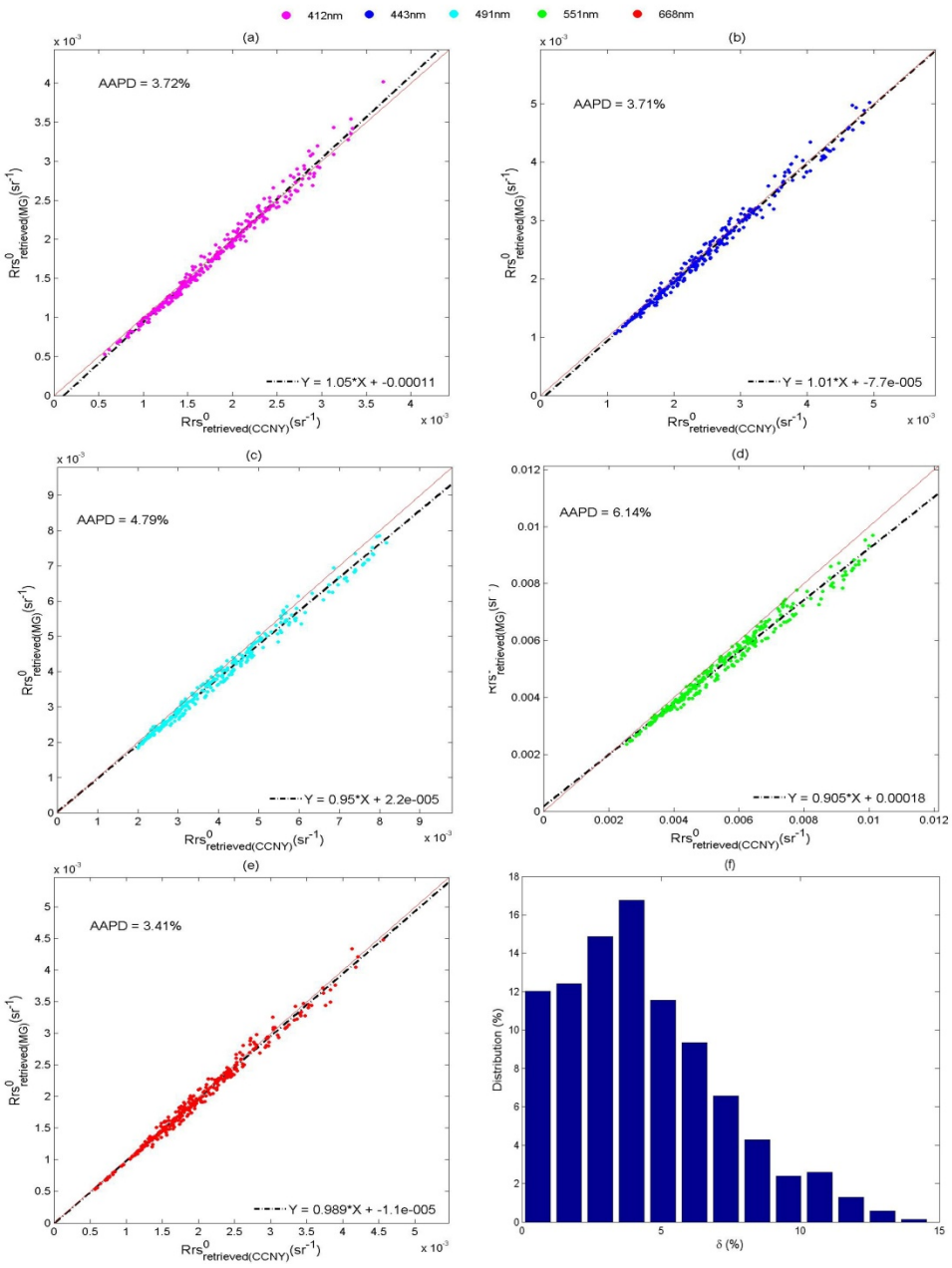

Figure 8-5. (a-e) Intercomparisons between $Rrs^0_{retrieved(CCNY)}$ and $Rrs^0_{retrieved(MG)}$ at (a) 412nm, (b) 443nm, (c) 491nm, (d) 551nm and (e) 668nm. (f) Distribution of absolute percent difference (δ) between $Rrs^0_{retrieved(CCNY)}$ and $Rrs^0_{retrieved(MG)}$ for all wavelengths. Both HyperSAS and SeaPRISM data are plotted together.

The wavelength dependencies in the correction error of the current *MG* algorithm may have confounding effects on the final OC data products as the processing algorithms for the final geophysical OC products such as [Chl] use the spectral ratio of the remote sensing reflectance values. The amount of error induced in the final OC data products resulted from the use of case 1 water optimized BRDF correction algorithm in the case 2 water conditions should be studied as it may have the implications on the monitoring of the water quality and variability in the coastal areas. Nevertheless, the exact quantification of the error induced by BRDF correction in the final OC data products will require the rigorous analysis of the each OC data product processing algorithm and, as the result, beyond the scope of this study.

8.4 Application of the BRDF Correction Algorithm to MODIS Satellite Data

A detail analysis carried out on the above and satellite water leaving radiance retrieved at LISCO site has confirmed that the LISCO site is appropriate for use in validation of the ocean color satellites in coastal waters [34]. The time series comparisons performed with the coincident satellite and in-situ data of LISCO exhibited both qualitative and quantitative agreements between the remote sensing reflectance derived from LISCO measurements.

Similarly to this previous study, time series and match-up comparisons have been carried out between the SeaPRISM above-water *in situ* measurements and satellite $Rrs^0(\lambda)$ data for LISCO's location. $Rrs^0(\lambda)$ data of both *in situ* and satellite are processed in the following two different ways: (i) with standard BRDF correction (*MG* algorithm), and (ii) with the proposed *CCNY* algorithm. Then, *in situ* and satellite data match up comparisons are carried out for both obtained datasets in order to assess merits and benefits of the proposed algorithm over the standard one.

We used the data from the Moderate Resolution Imaging Spectroradiometer (MODIS) onboard *Aqua* satellite for the match-up and for the comparisons with the *in situ* data. MODIS (Aqua) Level 1 data for a 14-month period (October 2009 through December 2010) are acquired from the ocean color data distribution website [129]. These data are processed using the software SeaDAS package version 6.2 (which contains all of the final processing programs and the source code used for the OBPG's Ocean Color Reprocessing 2010) into two groups of Level 2 data files (one group is processed with *MG* BRDF correction and another group with *CCNY* BRDF correction) with the nominal 1 km resolution. Then, we extracted the data of the 3 km × 3 km area centering the LISCO platform to create two time series of MODIS $Rrs^0(\lambda)$ data sets processed with *MG* and *CCNY* BRDF correction algorithms. For data quality assurance purpose, Level 2 flags (*i.e.* land, cloud, high sun glint, very low water-leaving radiance (cloud shadow), and atmospheric correction failure) were applied in the data extraction procedure. The average values of the 3 km × 3 km area are considered qualified for comparison with *in situ* data when at least 50% of the pixels are not affected by these standard flags. On the other hand, two sets of *in situ* SeaPRISM $Rrs^0(\lambda)$ data processed with *MG* and *CCNY* BRDF corrections are selected from the measurements that passed the data filtering procedures [33] and taken within ± 4 hours of the satellite overpass time for LISCO location.

Subsequently, we compared the MODIS $Rrs^0(\lambda)$ data, from here on denoted as $Rrs^0_{MODIS}(\lambda)$, to the corresponding SeaPRISM ($Rrs^0_{Spr}(\lambda)$) data. Comparisons are carried out with both correction algorithms and statistics, such as absolute average percent difference (AAPD), and coefficient of determination (R^2) have been obtained. A total of 42 MODIS and SeaPRISM matchups and comparisons have been carried out. Solar and sensor zenith angles of MODIS data used in the comparisons are in the range of 5^o to 56^o and 20^o to 60^o, respectively and therefore a wide range

of illumination and viewing geometries is available to test the bidirectional corrections. Table 8.2 shows the resulted AAPD values of the comparisons between $Rrs^0_{MODIS}(\lambda)$ and $Rrs^0_{Spr}(\lambda)$ data processed with *MG* and *CCNY* algorithms.

Table 8-2. AAPD values of the comparison between the $Rrs^0_{MODIS}(\lambda)$ and $Rrs^0_{Spr}(\lambda)$ data.

AAPD (%)	***Wavelength (nm)***				
	412	***443***	***491***	***551***	***668***
MG	***46.43***	***38.85***	***16.68***	***13.61***	***24.54***
CCNY	***42.40***	***34.16***	***14.93***	***10.99***	***21.89***
Improvement	***4.03***	***4.69***	***1.75***	***2.62***	***2.65***

Figure 8.6 shows the scatter plots of the $Rrs^0_{MODIS}(\lambda)$ versus $Rrs^0_{Spr}(\lambda)$ data. Left figure (a) shows the comparison of MODIS and SeaPRISM data, processed with the *MG* algorithm while right figure (b) shows the comparison of the same data processed with the *CCNY* algorithm. Three wavelengths, 491, 551 and 668 nm are shown in the plots and a stronger correlation (0.926) is observed for the comparisons processed with the *CCNY* algorithm. In addition, the slopes of the regression line are also improved and the biases are reduced. The dispersion between the satellite and *in situ* data, especially for high $Rrs^0(\lambda)$ values (which are usually associated with high particulate loading in the water), is reduced for the *CCNY* processing, thereby exhibiting its appropriateness for use in the bidirectional correction for coastal water types.

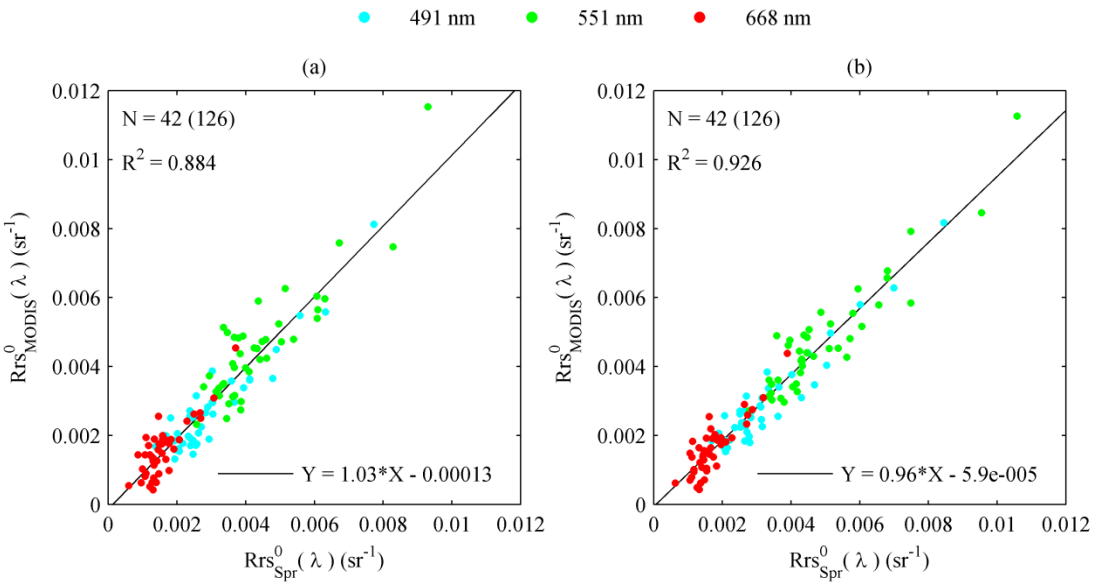

Figure 8-6. Scattering plots of the comparisons between MODIS and in situ $Rrs^0(\lambda)$ data: (a) comparison between MODIS and SeaPRISM with MG BRDF processing; (b) MODIS and SeaPRISM with CCNY BRDF processing.

8.5 Application of CCNY BRDF Correction in the Case-1 water condition

The main purpose of the proposed CCNY remote sensing reflectance model has been the utilization of it as the BRDF correction scheme specifically optimized for the Case-2 water conditions. Thus, CCNY model was developed with the use of the reflectance spectra simulated with the input IOP parameters typical to the coastal areas where in water constituents are usually dominated by sediment or CDOM. Matchup comparison analysis presented in the previous sections with the use of the above and satellite water leaving radiance data are also based on the Case-2 water conditions where LISCO is located. In the ideal situation, the BRDF correction in the satellite image processing would require the determination of the water type (i.e. whether case 1 or case 2 condition) beforehand so that appropriate correction scheme could be applied.

However, the determination of the water types itself require the retrieval of the IOP parameters through the remote sensing reflectance, and thus, such determination is proved to be difficult. Therefore, it is of upmost importance to investigate the potential implications resulted from the use of this case 2 water optimized correction algorithm in case 1 condition. For this purpose, a separate set of remote sensing reflectance spectra have been also simulated with the input IOP parameters typically observed in the case 1 water condition. For these simulations, Hydrolight's built in "New Case-1 water" model was applied and input [Chl] values ranging from 0.01 to 10mg/$m^3$are generated with 0.1 mg/m^3 linear spacing. Other simulation parameters are set the same as in the simulations performed for the case 2 condition in chapter 7. Based on that case 1 dataset, comparisons similar to the one performed in the section 8.1 are carried out to make the assessments to the CCNY algorithm's correction performance in the case 1 water condition. Distributions of the absolute percent difference (δ) values for without BRDF correction (red), $Rrs^0_{retrieved(MG)}$ (black) and $Rrs^0_{retrieved(CCNY)}$ (blue) for each matchup are shown in Figure 8.7. It can be observed from the figure that the variations in the bidirectional function of case 1 condition only slightly wider than those of case 2 condition.

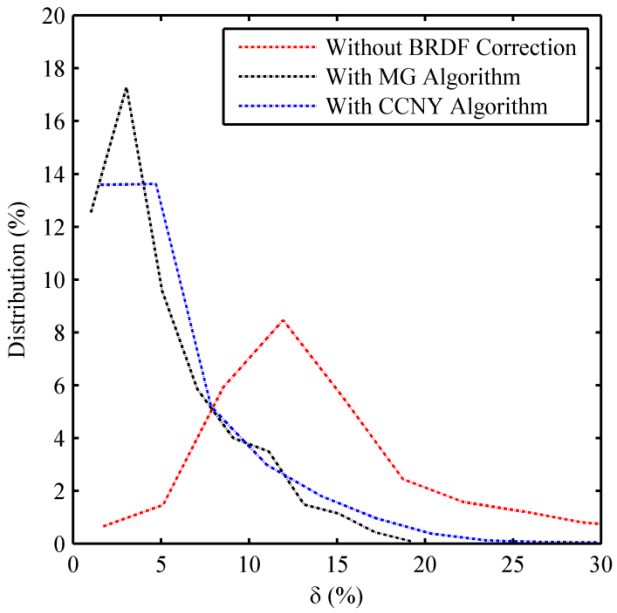

Figure 8-7. Distribution of the absolute percent difference (δ) values for without BRDF correction (red), $Rrs^{0}_{retrieved(MG)}$ (black) and $Rrs^{0}_{retrieved(CCNY)}$ (blue) for each matchup performed for simulated dataset obtained with the case 1 water conditions.

Interestingly, it is also observed that the bidirectional correction performances of CCNY and MG algorithm exhibit similar error statistics although MG algorithm slightly outperforms CCNY algorithm at all wavelengths (see Table 8.3). The spectral average AAPD values are 5.61% and 4.01% for corrections with CCNY and MG algorithms respectively. These results indicate that CCNY algorithm can be applied in the bidirectional correction for the pure case 1 condition if 1.6% increase in error is acceptable. Moreover, these results also underscore the CCNY algorithms' flexibility in dealing with the different water types and ranges of IOPs, there by

demonstrating the potentials to use the algorithm in the wide range of coastal regions around the globe.

Table 8-3. AAPD values in (%) between the Rrs^{0}_{actual} and *Rrs* without BRDF correction (1st row), $Rrs^{0}_{retrieved(CCNY)}$ (2nd row) and $Rrs^{0}_{retrieved(MG)}$ (3rd row) for matchup performed for the simulated dataset obtained with the case 1 water conditions.

	Wavelength (nm)					*Spectral Average*
	412	***443***	***491***	***551***	***668***	
Uncorrected	12.7	14.3	16.7	17.7	12.9	14.9
CCNY	4.48	5.12	5.82	6.26	5.35	5.41
MG	3.19	3.42	4.26	5.37	3.79	4.01

Furthermore, in order to analyze the characteristics of the bidirectional correction factors obtained with MG and CCNY algorithms based on the IOPs of the water body in synoptic scale, total particulate back-scattering coefficients, b_{bp}, as well as BRDF correction factor, C_{BRDF}, images are acquired from MODIS aqua satellite data. Total particulate back-scattering coefficients, b_{bp}, images are retrieved using QAA algorithm [59]. Two sets of C_{BRDF} images processed with CCNY algorithm, denoted as $C_{BRDF(CCNY)}$, and MG algorithm, denoted as $C_{BRDF(MG)}$, are also obtained. Then, the absolute relative percent differences between the corresponding pixels of the $C_{BRDF(CCNY)}$ and $C_{BRDF(MG)}$ images, denoted as δ_{BRDF}, are calculated to create the map of the absolute relative percent difference between them. Then, the analyses of the resulting δ_{BRDF} image along with the bbp image are carried out to make the assessments of the differences between the CCNY and MG bidirectional correction factors.

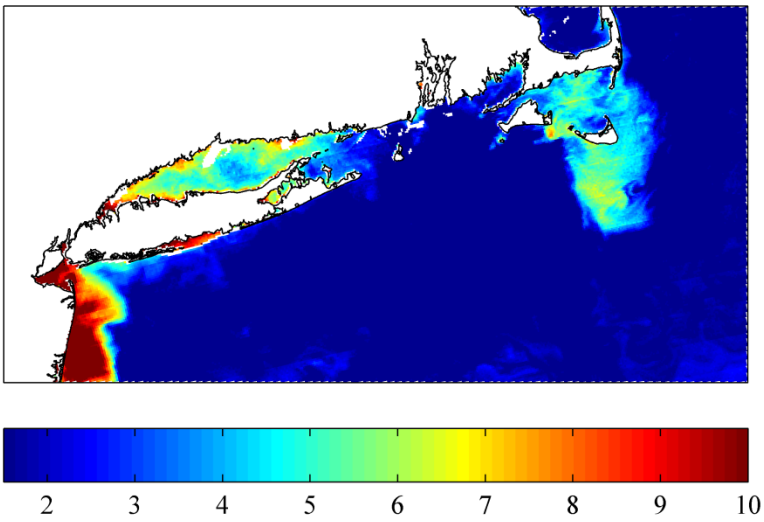

Figure 8-8. Absolute relative percent difference Map, δ_{BRDF}, in % between the $C_{BRDF(CCNY)}$ and $C_{BRDF(MG)}$ images of March 20, 2010 for 551nm wavelength. Color intensity values are limited between 1.5 and 10.

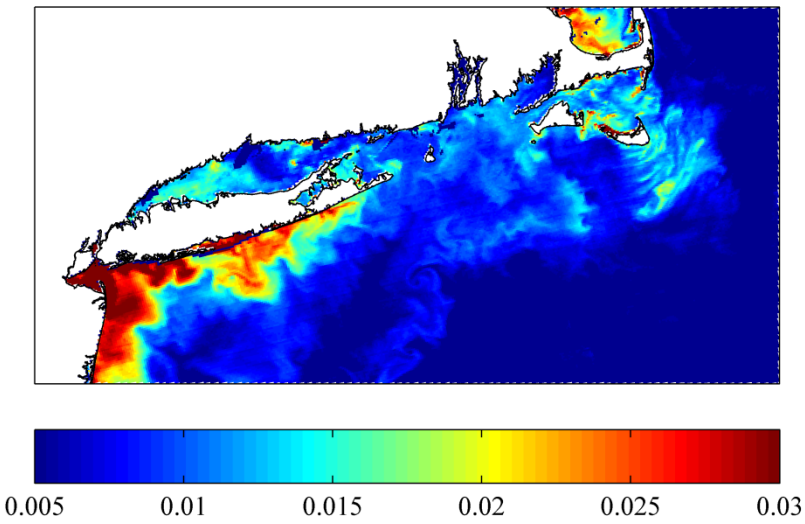

Figure 8-9. Total particulate back-scattering coefficient at 443nm, $b_{bp}(443)$, in m^{-1}.

Figure 8.8 shows a typical δ_{BRDF} image of the MODIS instrument onboard AQUA satellite. This particular δ_{BRDF} image is obtained from the data recorded on March 20 of 2010 which corresponds to the aftermath of the severe storm event occurred in the region. The b_{bp} image shown in Figure 8.9 clearly exhibits the flows of the sediment discharge from the rivers of the area. It can be observed in the image that the b_{bp} values at 443nm are particularly high (up to $0.15m^{-1}$) especially for the New York Lower Bay area and along the New Jersey coast because of the high particulate concentration resulted from the sediment discharge of the rivers. Therefore, those particular areas clearly represent the water conditions not dealt by the assumptions made in the development of MG algorithm. On the other hand, IOP parameters assumed in our simulations in the generating of remote sensing reflectance spectra cover these type of water conditions, and thus, CCNY algorithm is expected to perform well. It can be seen in the δ_{BRDF} image (Figure 8.8), absolute percent difference values are high (8~12%) for those areas underscoring the importance of the use of appropriate correction scheme. Nevertheless, for the open ocean areas with low particulate concentration levels which can be identified by the low particulate backscattering values, percent difference values in the δ_{BRDF} image are below 1.5%. As the result, from this imagery analysis, we conclude that CCNY algorithm can be used for the BRDF correction of water leaving radiance retrieved from the typical coastal water areas without needing the prior determination of water type as the uncertainties associated with the correction is increased by only 1.5% on average even if it were used for the case 1 condition.

8.6 Summary of the Chapter

We carried out the assessments of the bidirectional correction performed with the *CCNY* model as well as the operational *MG* algorithm based on the simulated dataset. Our assessments showed

that the proposed *CCNY* algorithm exhibits significant advantages over the operational *MG* algorithm. The retrieval errors resulted from *CCNY* BRDF corrections are relatively small and have AAPD values in the range 0.42 -0.85% .These small retrieval errors mostly come from the LSQ fitting procedure and are well below the well-known bidirectional variation of 10 - 20%. In addition, the regression lines between the retrieved and the actual remote sensing reflectance are very close to the 1:1 line for all viewing and illumination geometries. On the other hand, comparisons carried out using the current *MG* algorithm depict high AAPD values in the range of 6.2 - 9.54%. In addition, more than 57% of the *MG* retrievals are outside the range of 5% accuracy targeted by OC's sensor validation procedure. Systematic variations of the slope and of the bias with the scattering angles are also observed at all wavelengths for the comparisons. These results indicate that the *MG* algorithm, which is optimized for the case 1 water condition with [Chl] being the main input, is unsuited for use in optically complex case 2 waters if OC sensor validation procedure's 5% retrieval accuracy target is to be achieved.

Detail analysis on the performances of CCNY model were also carried out with the use of synthetically generated noise signals in order to identify the CCNY model's sensitivity to the noise, in other words, to verify whether CCNY model can still offer meaningful corrections if the retrieved remote sensing reflectance data is corrupted by the measurement uncertainties. Analysis provided the valuable information regarding the expected uncertainties in output remote sensing reflectance corrected with CCNY model as the function of the uncertainty level of the input data.

We also carried out comparisons of two algorithms for the above-water radiometric dataset of LISCO, which offers the unique capability of making near concurrent water-leaving radiance

measurements from different viewing geometries. LISCO's instrumentation set up in which two instruments acquire the data almost concurrently but at the different scattering angles with respect to the Sun is the major advantage we have in regard of analyzing the fidelity of bidirectional correction algorithms: we can compare the final remote sensing products, $Rrs^0(\lambda)$, retrieved from the measurements made by two instruments acquiring data at different viewing geometries. Comparisons are performed at all SeaPRISM wavelengths. With the proposed algorithm, comparison between the final remote sensing reflectance products of HyperSAS denoted as Rrs^0_{HS} and that of SeaPRISM denoted as Rrs^0_{Spr} exhibits a spectral average AAPD value of 10.2 % and very a strong correlation with a R^2 value of 0.972. On the other hand, the spectral average AAPD value of the comparison of the data processed with the current *MG* algorithm is 12.6% and the R^2 value is 0.958. The largest improvements in AAPD are found at 551 and 491nm.

We also tested merits of the proposed *CCNY* BRDF algorithm over the current operational *MG* algorithm by comparing MODIS data with *in situ* data. The study clearly shows that comparisons between MODIS and *in situ* data that are processed with the *CCNY* algorithm exhibits smaller AAPD values throughout the spectrum with a spectral average improvement of 3.15% for the SeaPRISM. In addition, stronger correlation coefficients were also observed in the comparison carried out with Rrs^0 data processed with the *CCNY* algorithm. Based on the separate dataset simulated for case 1 water condition and analysis carried out with particulate backscattering coefficient image, it is revealed that CCNY algorithm can be safely used for the BRDF correction of water leaving radiance retrieved from the typical coastal water areas without needing the prior determination of water type as the uncertainties associated with the correction is increased by only 1.5% on average even if it were used for the case 1 condition.

9 Summary and Conclusion

This research is primarily devoted to contribute the improvements in the ocean color data validation and processing procedures by identifying the underlying uncertainties in the in-situ and satellite data throughout the whole data processing steps, and reducing those uncertainties with refined above water and satellite data processing protocol particularly through developing a bidirectional correction algorithm optimized for the case 2 conditions. Hyper- and multi-spectral instrumentation and configuration of LISCO which is located in the water area with typical coastal properties enable us to fulfill these main objectives by providing the reliable time series data for the validation of satellite OC data and development of new processing algorithm.

The first part of this thesis mainly deals with the assessments of uncertainties in the above water and satellite data and processing procedures. By using the quality assured hyper- and multi-spectral dataset of LISCO, we investigated the uncertainties in the above water data associated with the randomly fluctuating wave perturbation effects and, based on the seasonal and temporal variability analysis, defined the range of the viewing geometry range in which above water radiometric measurements can be performed with the acceptable uncertainty level. The 1-year time series of $nLw(\lambda)$ data obtained with the collocated instruments exhibits that the seasonal as well as temporal changes are well captured by both above-water measurement systems and the quantitative matchup comparisons performed for the measured and retrieved data of HyperSAS and SeaPRISM show strong correlation and consistency between two datasets.

Significant efforts were also devoted to the analysis that investigates LISCO's appropriateness as the OC data validation site. Detail analyses were carried out, using the OC data retrieved from MERIS, MODIS and SeaWIFS sensors. From the analysis, it is concluded that (i) the adjacency

effect is negligible in the direct vicinity of the platform and further offshore, (ii) for every satellite mission, field and satellite data are significantly correlated with R^2 values close to 0.7 for MERIS and SeaWiFS and greater than 0.87 for MODIS data there by proving the suitability of LISCO site for validation purpose, and (iii) LISCO's *nLw* data strongly correlate with satellite *nLw* data of every missions showing R^2 value greater than 0.75 and 0.9 for the wavelength greater than 443 and 490nm respectively exhibiting potential to be used as reliable OC data validation site.

In the second part of the thesis, after detailing the development of CCNY bidirectional correction algorithm, we carried out the assessments of the bidirectional correction performed with the *CCNY* model as well as the operational *MG* algorithm based on the simulated dataset. Our assessments showed that the proposed *CCNY* algorithm exhibits significant advantages over the operational *MG* algorithm. The retrieval errors resulted from *CCNY* BRDF corrections are relatively small and have AAPD values in the range 0.42 -0.85%. On the other hand, comparisons carried out using the current *MG* algorithm depict high AAPD values in the range of 6.2 - 9.54%. In addition, more than 57% of the *MG* retrievals are outside the range of 5% accuracy targeted by OC's sensor validation procedure. Systematic variations of the slope and of the bias with the scattering angles are also observed at all wavelengths for the comparisons. These results indicate that the *MG* algorithm, which is optimized for the case 1 water condition with [Chl] being the main input, is unsuited for use in optically complex case 2 waters if OC sensor validation procedure's 5% retrieval accuracy target is to be achieved.

We also carried out comparisons of two algorithms for the above-water radiometric dataset of LISCO, which offers the unique capability of making near concurrent water-leaving radiance

measurements from different viewing geometries. With the proposed algorithm, comparison between the final remote sensing reflectance products of HyperSAS denoted as Rrs^{0}_{HS} and that of SeaPRISM denoted as Rrs^{0}_{Spr} exhibits a spectral average AAPD value of 10.2 % and very a strong correlation with a R^2 value of 0.972. On the other hand, the spectral average AAPD value of the comparison of the data processed with the current *MG* algorithm is 12.6% and the R^2 value is 0.958. The largest improvements in AAPD are found at 551 and 491nm. Finally, we tested merits of the proposed *CCNY* BRDF algorithm over the current operational *MG* algorithm by comparing MODIS data with *in situ* data. The study clearly shows that comparisons between MODIS and *in situ* data that are processed with the *CCNY* algorithm exhibits smaller AAPD values throughout the spectrum with a spectral average improvement of 3.15% for the SeaPRISM. In addition, stronger correlation coefficients were also observed in the comparison carried out with $Rrs^{0}(\lambda)$ data processed with the *CCNY* algorithm. Based on the separate dataset simulated for case 1 water condition and analysis carried out with satellite retrieved particulate backscattering coefficient images of the vast area of ocean with varying water conditions and types, it has been shown that CCNY algorithm is applicable in case 1 condition as well for the BRDF correction of water leaving radiance if the small increase in retrieval correction error is acceptable. In conclusion, with the use of this CCNY algorithm in the processing and validation of water leaving radiance of the coastal areas, the quality of the OC data can be improved; therefore, operational use of this algorithm is suggested.

Bibliography

1. P. M. Vitousek, H. A. Mooney, J. Lubchenco, and J. M. Melillo, "Human domination of Earth's ecosystems," Science **277**, 494 (1997).
2. S. HOOKER, E. FIRESTONE, W. ESAIAS, G. FELDMAN, W. GREGG, and C. MCCLAIN, "SeaWiFS technical report series. Volume 1: An overview of SeaWiFS and ocean color," (1992).
3. P. J. C. Corresponding and C. Steele, "MERIS: the re-branding of an ocean sensor," International Journal of Remote Sensing **26**, 1781-1798 (2005).
4. A. Savtchenko, D. Ouzounov, S. Ahmad, J. Acker, G. Leptoukh, J. Koziana, and D. Nickless, "Terra and Aqua MODIS products available from NASA GES DAAC," Advances in Space Research **34**, 710-714 (2004).
5. C. Welsch, H. Swenson, S. A. Cota, F. DeLuccia, J. M. Haas, C. Schueler, R. M. Durham, J. E. Clement, and P. E. Ardanuy, "VIIRS (Visible Infrared Imager Radiometer Suite): a next-generation operational environmental sensor for NPOESS," in (IEEE, 2001), 1020-1022 vol. 1023.
6. R. E. Murphy, W. L. Barnes, A. I. Lyapustin, J. Privette, C. Welsch, F. DeLuccia, H. Swenson, C. F. Schueler, P. E. Ardanuy, and P. S. M. Kealy, "Using VIIRS to provide data continuity with MODIS," in (IEEE, 2001), 1212-1214 vol. 1213.
7. F. Gohin, J. Druon, and L. Lampert, "A five channel chlorophyll concentration algorithm applied to SeaWiFS data processed by SeaDAS in coastal waters," International Journal of Remote Sensing **23**, 1639-1661 (2002).
8. J. E. O'Reilly, S. Maritorena, G. Mitchell, D. A. Siegel, K. L. Carder, D. L. Garver, M. Kahru, and C. R. McClain, "Ocean color chlorophyll algorithms for Seawifs," Journal of Geophysical Research **103**, 24937-24950 (1998).
9. A. A. Gilerson, A. A. Gitelson, J. Zhou, D. Gurlin, W. Moses, I. Ioannou, and S. A. Ahmed, "Algorithms for remote estimation of chlorophyll-a in coastal and inland waters using red and near infrared bands," Optics Express **18**, 24109-24125 (2010).
10. S. Maritorena, D. A. Siegel, and A. R. Peterson, "Optimization of a semianalytical ocean color model for global-scale applications," Applied optics **41**, 2705-2714 (2002).
11. D. A. Siegel, M. Wang, S. Maritorena, and W. Robinson, "Atmospheric correction of satellite ocean color imagery: the black pixel assumption," Applied optics **39**, 3582-3591 (2000).
12. H. R. Gordon, "Removal of atmospheric effects from satellite imagery of the oceans," Applied Optics **17**, 1631-1636 (1978).
13. H. R. Gordon and M. Wang, "Retrieval of water-leaving radiance and aerosol optical thickness over the oceans with SeaWiFS: a preliminary algorithm," Applied optics **33**, 443-452 (1994).
14. M. Wang and H. R. Gordon, "A simple, moderately accurate, atmospheric correction algorithm for Seawifs," Remote sensing of environment **50**, 231-239 (1994).
15. A. Morel, D. Antoine, and B. Gentili, "Bidirectional reflectance of oceanic waters: accounting for Raman emission and varying particle scattering phase function," Applied Optics **41**, 6289-6306 (2002).
16. Y.-J. Park and K. Ruddick, "Model of remote-sensing reflectance including bidirectional effects for case 1 and case 2 waters," Appl. Opt. **44**, 1236 (2005).

17. A. Morel and B. Gentili, "Diffuse reflectance of oceanic waters. II Bidirectional aspects," Applied Optics **32**, 6864-6879 (1993).
18. A. Morel and B. Gentili, "Diffuse reflectance of oceanic waters. III. Implication of bidirectionality for the remote-sensing problem," Applied Optics **35**, 4850-4862 (1996).
19. A. Morel, K. J. Voss, and B. Gentili, "Bidirectional reflectance of oceanic waters: a comparison of modeled and measured upward radiance fields," Journal of Geophysical Research-Oceans **100**, 13,143-113,150 (1995).
20. K. J. Voss and A. Morel, "Bidirectional reflectance function for oceanic waters with varying chlorophyll concentrations: Measurements versus predictions," Limnology And Oceanography, 698-705 (2005).
21. D. McKee, A. Cunningham, D. Wright, and L. Hay, "Determining the impact of non-algal materials on water-leaving solar stimulated fluorescence signals in coastal waters," in (IEEE, 2007), 1-6.
22. A. Gilerson, J. Zhou, R. Fortich, I. Ioannou, S. Hlaing, B. Gross, F. Moshary, and S. Ahmed, "Spectral dependence of the bidirectional reflectance function in coastal waters and its impact on retrieval algorithms," in (IEEE, 2007), 3777-3780.
23. A. Gilerson, S. Hlaing, T. Harmel, A. Tonizzo, R. Arnone, A. Weidemann, and S. Ahmed, "Bidirectional reflectance function in coastal waters: modeling and validation," in 2011), 81750O.
24. Z. P. Lee, K. Du, K. J. Voss, G. Zibordi, B. Lubac, R. Arnone, and A. Weidemann, "An inherent-optical-property-centered approach to correct the angular effects in water-leaving radiance," Appl. Opt. **50**, 3155 (2011).
25. K. Oubelkheir, L. A. Clementson, I. T. Webster, P. W. Ford, A. G. Dekker, L. C. Radke, and P. Daniel, "Using inherent optical properties to investigate biogeochemical dynamics in a tropical macrotidal coastal system," Journal of Geophysical Research **111**, C07021 (2006).
26. M. J. R. Fasham, *Ocean biogeochemistry: the role of the ocean carbon cycle in global change* (Springer Verlag, 2003).
27. F. Mélin, M. Clerici, G. Zibordi, B. N. Holben, and A. Smirnov, "Validation of SeaWiFS and MODIS aerosol products with globally distributed AERONET data," Remote Sensing of Environment **114**, 230-250 (2010).
28. G. Zibordi, J. F. Berthon, F. Mélin, D. D'Alimonte, and S. Kaitala, "Validation of satellite ocean color primary products at optically complex coastal sites: northern Adriatic Sea, northern Baltic Proper and Gulf of Finland," Remote Sensing of Environment (2009).
29. G. Zibordi, B. N. Holben, I. Slutsker, D. Giles, D. D'Alimonte, F. Mélin, J. F. Berthon, D. Vandemark, H. Feng, and G. Schuster, "AERONET-OC: a network for the validation of ocean color primary radiometric products," J. Atmos. Ocean. Technol **26**, 1634–1651 (2009).
30. G. Zibordi, F. Mélin, S. B. Hooker, D. D'Alimonte, and B. Holben, "An autonomous above-water system for the validation of ocean color radiance data," IEEE Transactions on Geoscience and Remote Sensing **42**, 401-415 (2004).
31. B. N. Holben, T. F. Eck, I. Slutsker, D. Tanre, J. P. Buis, A. Setzer, E. Vermote, J. A. Reagan, Y. J. Kaufman, and T. Nakajima, "AERONET-A Federated Instrument Network and Data Archive for Aerosol Characterization," Remote sensing of environment **66**, 1-16 (1998).

32. G. Zibordi, S. B. Hooker, J. F. Berthon, and D. D'Alimonte, "Autonomous above-water radiance measurements from an offshore platform: a field assessment experiment," Journal of Atmospheric and Oceanic Technology **19**(2002).
33. T. Harmel, A. Gilerson, S. Hlaing, A. Tonizzo, T. Legbandt, A. Weidemann, R. Arnone, and S. Ahmed, "Long Island Sound Coastal Observatory: Assessment of Above-water Reflectance Measurement Uncertainties Using Collocated Multi and Hyper-spectral Radiometers," Applied Optics (2011).
34. S. Hlaing, T. Harmel, A. Ibrahim, I. Ioannou, A. Tonizzo, A. Gilerson, and S. Ahmed, "Validation of ocean color satellite sensors using coastal observational platform in Long Island Sound," in *Proc. of SPIE*, 2010), 782504.
35. B. Holben, T. Eck, I. Slutsker, D. Tanre, J. Buis, A. Setzer, E. Vermote, J. Reagan, Y. Kaufman, and T. Nakajima, "AERONET--A federated instrument network and data archive for aerosol characterization," Remote Sensing of Environment **66**, 1-16 (1998).
36. S. B. Hooker, G. Lazin, G. Zibordi, and S. McLean, "An evaluation of above-and in-water methods for determining water-leaving radiances," (2010).
37. S. Ahmed, T. Harmel, R. A. Arnone, A. Gilerson, S. Hlaing, and A. D. Weidemann, "Multi- and Hyperspectral Ocean Color Measurements from Long Island Sound Observation Platform (LISCO): Comparison with Satellite Measurements & Assessments of Uncertainties," in *Ocean Optics XX*, 2010),
38. A. Tonizzo, J. Zhou, A. Gilerson, M. S. Twardowski, D. J. Gray, R. A. Arnone, B. M. Gross, F. Moshary, and S. A. Ahmed, "Polarized light in coastal waters: hyperspectral and multiangular analysis," Opt. Express **17**, 5666-5683 (2009).
39. W. E. Esaias, M. R. Abbott, I. Barton, O. B. Brown, J. W. Campbell, K. L. Carder, D. K. Clark, R. H. Evans, F. E. Hoge, and H. R. Gordon, "An overview of MODIS capabilities for ocean science observations," Geoscience and Remote Sensing, IEEE Transactions on **36**, 1250-1265 (1998).
40. H. R. Gordon, D. K. Clark, J. W. Brown, O. B. Brown, R. H. Evans, and W. W. Broenkow, "Phytoplankton pigment concentration in the Middle Atlantic Bight: comparison of ship determinations and CZCS estimates," Applied Optics **22**, 20-36 (1983).
41. H. R. Gordon and D. J. Castaño, "Coastal Zone Color Scanner atmospheric correction algorithm: multiple scattering effects," Applied Optics **26**, 2111-2122 (1987).
42. J. A. Yoder, C. R. McClain, G. C. Feldman, and W. E. Esaias, "Annual cycles of phytoplankton chlorophyll concentrations in the global ocean: a satellite view," Global Biogeochemical Cycles **7**, 181-193 (1993).
43. M. Hetscher, H. Krawczyk, A. Neumann, and G. Zimmermann, "Four years of ocean colour remote sensing with MOS-IRS," International Journal of Remote Sensing, 25 **7**, 1415-1421 (2004).
44. F. Sakaida, M. Moriyama, H. Murakami, H. Oaku, Y. Mitomi, A. Mukaida, and H. Kawamura, "The sea surface temperature product algorithm of the Ocean Color and Temperature Scanner (OCTS) and its accuracy," Journal of Oceanography **54**, 437-442 (1998).
45. P. Y. Deschamps, F. M. Bréon, M. Leroy, A. Podaire, A. Bricaud, J. C. Buriez, and G. Seze, "The POLDER mission: Instrument characteristics and scientific objectives," Geoscience and Remote Sensing, IEEE Transactions on **32**, 598-615 (1994).

46. T. S. Pagano and R. M. Durham, "Moderate resolution imaging spectroradiometer (MODIS)," in 1993), 2.
47. W. L. Barnes, T. S. Pagano, and V. V. Salomonson, "Prelaunch characteristics of the moderate resolution imaging spectroradiometer (MODIS) on EOS-AM1," Geoscience and Remote Sensing, IEEE Transactions on **36**, 1088-1100 (1998).
48. M. Rast, J. Bezy, and S. Bruzzi, "The ESA Medium Resolution Imaging Spectrometer MERIS a review of the instrument and its mission," International Journal of Remote Sensing **20**, 1681-1702 (1999).
49. S. D. Miller, J. D. Hawkins, J. Kent, F. J. Turk, T. F. Lee, A. P. Kuciauskas, K. Richardson, R. Wade, and C. Hoffman, "NexSat: Previewing NPOESS/VIIRS imagery capabilities," Bulletin of the American Meteorological Society **87**, 433-446 (2006).
50. T. E. Lee, S. D. Miller, F. J. Turk, C. Schueler, R. Julian, S. Deyo, P. Dills, and S. Wang, "The NPOESS VIIRS day/night visible sensor," Bulletin of the American Meteorological Society **87**, 191-200 (2006).
51. C. B. Field, M. J. Behrenfeld, J. T. Randerson, and P. Falkowski, "Primary production of the biosphere: integrating terrestrial and oceanic components," Science **281**, 237 (1998).
52. W. W. Gregg, N. W. Casey, and C. R. McClain, "Recent trends in global ocean chlorophyll," Geophysical Research Letters **32**, L03606 (2005).
53. IOCCG, "Minimum requirements for an operational, ocean-colour sensor for the open ocean," (Dartmouth, Canada, 1997).
54. C. R. McClain, G. C. Feldman, and S. B. Hooker, "An overview of the SeaWiFS project and strategies for producing a climate research quality global ocean bio-optical time series," Deep-Sea Research Part Ii-Topical Studies In Oceanography **51**, 5-42 (2004).
55. S. Sathyendranath, A. Longhurst, C. M. Caverhill, and T. Platt, "Regionally and seasonally differentiated primary production in the North Atlantic," Deep-Sea Research (Part I, Oceanographic Research Papers) **42**, 1773-1802 (1995).
56. D. A. Siegel, S. Maritorena, N. B. Nelson, M. J. Behrenfeld, and C. R. McClain, "Colored dissolved organic matter and its influence on the satellite-based characterization of the ocean biosphere," Geophysical Research Letters **32**(2005).
57. D. A. Siegel, S. Maritorena, N. B. Nelson, D. A. Hansell, and M. Lorenzi-Kayser, "Global distribution and dynamics of colored dissolved and detrital organic materials," Journal of Geophysical Research **107**, 3228-3249 (2002).
58. M. S. Twardowski, E. Boss, J. B. Macdonald, W. S. Pegau, A. H. Barnard, and J. R. V. Zaneveld, "A model for estimating bulk refractive index from the optical backscattering ratio and the implications for understanding particle composition in case I and case II waters," Journal of Geophysical Research **106**, 14129-14142 (2001).
59. Z. P. Lee, K. L. Carder, and R. A. Arnone, "Deriving inherent optical properties from water color: a multiband quasi-analytical algorithm for optically deep waters," Applied Optics **41**, 5755-5772 (2002).
60. C. D. Mobley, *Light and Water: Radiative Transfer in Natural Waters* (Academic Press, New York, 1994).
61. H. R. Gordon and M. Wang, "Surface-roughness considerations for atmospheric correction of ocean color sensors. I: The Rayleigh-scattering component," Applied optics **31**, 4247-4260 (1992).
62. M. Wang, "The SeaWiFS atmospheric correction algorithm updates," (2000).

63. E. Vermote and A. Vermeulen, "Atmospheric correction algorithm: spectral reflectances (MOD09)," ATBD version **4**(1999).
64. M. H. Wang, "Remote sensing of the ocean contributions from ultraviolet to near-infrared using the shortwave infrared bands: simulations," Applied Optics **46**, 1535-1547 (2007).
65. IOCCG, "Remote sensing of inherent optical properties: fundamentals, tests of algorithms, and applications. ," (Dartmouth, Canada, 2006).
66. C. R. McClain, M. L. Cleave, G. C. Feldman, W. W. Gregg, S. B. Hooker, and N. Kuring, "Science quality SeaWiFS data for global biosphere research," Sea Technol **39**, 10–15 (1998).
67. H. R. Gordon and D. K. Clark, "Remote sensing optical properties of a stratified ocean: an improved interpretation," Applied Optics **19**, 3428-3430 (1980).
68. H. R. Gordon and D. K. Clark, "Clear water radiances for atmospheric correction of coastal zone color scanner imagery," Applied Optics **20**, 4175-4180 (1981).
69. J. E. O'Reilly, S. Maritorena, B. G. Mitchell, D. A. Siegel, K. L. Carder, S. A. Garver, M. Kahru, and C. McClain, "Ocean color chlorophyll algorithms for SeaWiFS," Journal Of Geophysical Research-Oceans **103**, 24937 (1998).
70. S. W. Bailey and P. J. Werdell, "A multi-sensor approach for the on-orbit validation of ocean color satellite data products," Remote Sensing of Environment **102**, 12-23 (2006).
71. C. D. Mobley, "Estimation of the remote-sensing reflectance from above-surface measurements," Applied Optics **38**, 7442-7455 (1999).
72. S. B. Hooker, G. Zibordi, J. F. Berthon, D. D'Alimonte, D. v. d. Linde, and J. W. Brown, "Tower-Perturbation Measurements in Above-Water Radiometry," (NASA Goddard Space Flight Center, Greenbelt, MD, NASA Tech. Memo. TM-2002-206 892, ser. SeaWiFS Postlaunch Technical Report Series, vol. 23, S. B. Hooker and E. R. Firestone, Eds., 2003., 2003).
73. O. Dubovik and M. D. King, "A flexible inversion algorithm for retrieval of aerosol optical properties from Sun and sky radiance measurements," J. Geophys. Res. **105**, 20,673-620,696 (2000).
74. http://aeronet.gsfc.nasa.gov/
75. S. Kay, J. D. Hedley, and S. Lavender, "Sun Glint Correction of High and Low Spatial Resolution Images of Aquatic Scenes: a Review of Methods for Visible and Near-Infrared Wavelengths," Remote Sensing **1**, 697-730 (2009).
76. R. Austin, "Inherent spectral radiance signatures of the ocean surface," Ocean color analysis **7410**, 1-20 (1974).
77. C. Mobley and L. Sundman, "Hydrolight 4.2 users' guide," Sequoia Scientific, Inc., Redmond, WA **87**(2001).
78. S. B. Hooker, G. Lazin, G. Zibordi, and S. McLean, "An evaluation of above-and in-water methods for determining water-leaving radiances," Journal of Atmospheric and Oceanic Technology **19**(2002).
79. C. Fröhlich and G. E. Shaw, "New determination of Rayleigh scattering in the terrestrial atmosphere," Applied optics **19**, 1773-1775 (1980).
80. A. Young, "Revised depolarization corrections for atmospheric extinction," Applied optics **19**, 3427-3428 (1980).
81. S. B. Hooker and A. Morel, "Platform and environmental effects on above-water determinations of water-leaving radiances," Journal of Atmospheric and Oceanic Technology **20**, 187-205 (2003).

82. S. Y. Kotchenova and E. F. Vermote, "Validation of a vector version of the 6S radiative transfer code for atmospheric correction of satellite data. Part II. Homogeneous Lambertian and anisotropic surfaces," Applied Optics **46**, 4455-4464 (2007).
83. S. Y. Kotchenova, E. F. Vermote, R. Matarrese, and F. J. Klemm, "Validation of a vector version of the 6S radiative transfer code for atmospheric correction of satellite data. Part I: Path radiance," Applied Optics **45**, 6762-6774 (2006).
84. D. Antoine, F. d'Ortenzio, S. B. Hooker, G. Bécu, B. Gentili, D. Tailliez, and A. J. Scott, "Assessment of uncertainty in the ocean reflectance determined by three satellite ocean color sensors (MERIS, SeaWiFS and MODIS-A) at an offshore site in the Mediterranean Sea (BOUSSOLE project)," J. Geophys. Res. **113**(2008).
85. C. Cox and W. Munk, "Statistics Of The Sea Surface Derived From Sun Glitter," Journal Of Marine Research **13**, 198-227 (1954).
86. C. Cox and W. Munk, "Measurement Of The Roughness Of The Sea Surface From Photographs Of The Suns Glitter," Journal Of The Optical Society Of America **44**, 838-850 (1954).
87. C. Cox and W. Munk, "Slopes of the sea surface deduced from photographs of sun glitter," (1956).
88. T. Nakajima and M. Tanaka, "Effect of wind-generated waves on the transfer of solar radiation in the atmosphere-ocean system," Journal of Quantitative Spectroscopy and Radiative Transfer **29**, 521-537 (1983).
89. G. S. Fargion, J. L. Mueller, and S. Project, *Ocean optics protocols for satellite ocean color sensor validation, Revision 2* (National Aeronautics and Space Administration, Goddard Space Flight Center, 2000).
90. Z. Lee, K. L. Carder, S. K. Hawes, R. G. Steward, T. G. Peacock, and C. O. Davis, "Model for interpretation of hyperspectral remote-sensing reflectance," Applied Optics **33**, 5721-5732 (1994).
91. Y. Liu and K. Voss, "Polarized radiance distribution measurement of skylight. II. Experiment and data," Applied optics **36**, 8753-8764 (1997).
92. G. Zibordi and B. Bulgarelli, "Effects of cosine error in irradiance measurements from field ocean color radiometers," Applied optics **46**, 5529-5538 (2007).
93. V. Ransibrahmanakul and R. Stumpf, "Correcting ocean colour reflectance for absorbing aerosols," International Journal of Remote Sensing **27**, 1759-1774 (2006).
94. K. J. Voss, S. McLean, M. Lewis, C. Johnson, S. Flora, M. Feinholz, M. Yarbrough, C. Trees, M. Twardowski, and D. Clark, "An example crossover experiment for testing new vicarious calibration techniques for satellite ocean color radiometry," Journal of Atmospheric and Oceanic Technology (2010).
95. P. Y. Deschamps, B. Fougnie, R. Frouin, P. Lecomte, and C. Verwaerde, "SIMBAD: a field radiometer for satellite ocean-color validation," Applied optics **43**, 4055-4069 (2004).
96. D. Tanre, M. Herman, P. Y. Deschamps, and A. Deleffe, "Atmospheric Modeling For Space Measurements Of Ground Reflectances, Including Bidirectional Properties," Applied Optics **18**, 3587-3594 (1979).
97. D. Tanre, M. Herman, and P. Y. Deschamps, "Influence of the background contribution upon space measurements of ground reflectance," Applied Optics **20**, 3676-3684 (1981).
98. L. A. Remer, Y. J. Kaufman, Tanr, D., S. Mattoo, D. A. Chu, J. V. Martins, R. R. Li, C. Ichoku, R. C. Levy, R. G. Kleidman, T. F. Eck, E. Vermote, and B. N. Holben, "The

MODIS Aerosol Algorithm, Products, and Validation," Journal of the Atmospheric Sciences **62**, 947-973 (2005).
99. M. Wang, S. Son, and W. Shi, "Evaluation of MODIS SWIR and NIR-SWIR atmospheric correction algorithms using SeaBASS data," Remote Sensing of Environment **113**, 635 (2009).
100. D. Clark, H. Gordon, K. Voss, Y. Ge, W. Broenkow, and C. Trees, "Validation of atmospheric correction over the oceans," Journal of Geophysical Research **102**, 17209-17217,17217 (1997).
101. C. K. Gatebe, M. D. King, A. I. Lyapustin, G. T. Arnold, and J. Redemann, "Airborne spectral measurements of ocean directional reflectance," Journal of the atmospheric sciences **62**, 1072-1092 (2005).
102. Z. Lee, K. L. Carder, C. D. Mobley, R. G. Steward, and J. S. Patch, "Hyperspectral remote sensing for shallow waters. I. A semianalytical model," Applied Optics **37**, 6329-6338 (1998).
103. Z. Lee, K. L. Carder, C. D. Mobley, R. G. Steward, and J. S. Patch, "Hyperspectral remote sensing for shallow waters. 2. Deriving bottom depths and water properties by optimization," Applied Optics **38**, 3831-3843 (1999).
104. A. Albert and C. Mobley, "An analytical model for subsurface irradiance and remote sensing reflectance in deep and shallow case-2 waters," Opt. Express **11**, 2873-2890 (2003).
105. A. Albert and P. Gege, "Inversion of irradiance and remote sensing reflectance in shallow water between 400 and 800 nm for calculations of water and bottom properties," Applied Optics **45**, 2331-2343 (2006).
106. H. R. Gordon, J. W. Brown, R. H. Evans, O. B. Brown, Smith, Baker, and D. K. Clark, "A semianalytic radiance model of ocean color," Journal of Geophysical Research **93**, 10909-10924 (1988).
107. P. Gege and A. Albert, "A tool for inverse modeling of spectral measurements in deep and shallow waters," Remote sensing of aquatic coastal ecosystem processes, 81-109 (2006).
108. H. R. Gordon, "Normalized water-leaving radiance: revisiting the influence of surface roughness," Applied Optics **44**, 241-248 (2005).
109. M. Wang, "Effects of ocean surface reflectance variation with solar elevation on normalized water-leaving radiance," Applied optics **45**, 4122-4128 (2006).
110. C. D. Mobley and L. K. Sundman, "HYDROLIGHT 5 ECOLIGHT 5," (Sequoia Scientific Inc, 2008).
111. R. M. Pope and E. S. Fry, "Absorption spectrum (380-700 nm) of pure water .2. Integrating cavity measurements," Applied Optics **36**, 8710-8723 (1997).
112. C. Mobley and L. Sundman, "HYDROLIGHT 4.2, Sequoia Scientific," (Inc, 2001).
113. A. M. Ciotti, M. R. Lewis, and J. J. Cullen, "Assessment of the relationships between dominant cell size in natural phytoplankton communities and the spectral shape of the absorption coefficient," Limnology And Oceanography, 404-417 (2002).
114. D. Stramski, A. Bricaud, and A. Morel, "Modeling the inherent optical properties of the ocean based on the detailed composition of the planktonic community," Applied Optics **40**, 2929-2945 (2001).

115. A. Bricaud, M. Babin, A. Morel, and H. Claustre, "Variability in the chlorophyll-specific absorption coefficients of natural phytoplankton: Analysis and parameterization," J. Geophys. Res **100**, 13321-13332 (1995).
116. Voss, "A spectral model of the beam attenuation coefficient in the ocean and coastal areas," Limnology and oceanography **37**, 501 (1992).
117. A. Morel, *Optical properties of pure water and pure seawater, in Optical Aspects of Oceanography*, Optical Aspects of Oceanography (Academic Press, New York, 1974), pp. 1-24.
118. T. J. Petzold, "Volume scattering functions for selected ocean waters," (DTIC Document, 1972).
119. C. D. Mobley, L. K. Sundman, and E. Boss, "Phase function effects on oceanic light fields," Applied Optics **41**, 1035-1050 (2002).
120. G. R. Fournier and J. L. Forand, "Analytic phase function for ocean water," in 1994), 194.
121. Z. P. Lee, *Remote sensing of inherent optical properties: fundamentals, tests of algorithms, and applications* (International Ocean-Colour Coordinating Group, 2006), Vol. 5.
122. A. Gilerson, J. Zhou, S. Hlaing, I. Ioannou, J. Schalles, B. Gross, F. Moshary, and S. Ahmed, "Fluorescence component in the reflectance spectra from coastal waters. Dependence on water composition," Optics Express **15**, 15702-15721 (2007).
123. S. Ahmed, A. Gilerson, A. Gill, B. Gross, F. Moshary, and J. Zhou, "Separation of fluorescence and elastic scattering from algae in seawater using polarization discrimination," Optics communications **235**, 23-30 (2004).
124. A. Harrison and C. Coombes, "An opaque cloud cover model of sky short wavelength radiance," Solar Energy **41**, 387-392 (1988).
125. W. W. Gregg and K. L. Carder, "A simple spectral solar irradiance model for cloudless maritime atmospheres," Limnology and oceanography, 1657-1675 (1990).
126. S. B. Hooker, G. Zibordi, J. F. Berthon, and J. W. Brown, "Above-water radiometry in shallow coastal waters," Applied Optics **43**, 4254-4268 (2004).
127. H. J. Gons, M. Rijkeboer, and K. G. Ruddick, "A chlorophyll-retrieval algorithm for satellite imagery (Medium Resolution Imaging Spectrometer) of inland and coastal waters," Journal of Plankton Research **24**, 947 (2002).
128. D. McKee, A. Cunningham, D. Wright, and L. Hay, "Potential impacts of nonalgal materials on water-leaving Sun induced chlorophyll fluorescence signals in coastal waters," Applied Optics **46**, 7720-7729 (2007).
129. http://oceancolor.gsfc.nasa.gov/